NTNU
Norwegian University of
Science and Technology

Review of a Semi-Analytical Drillstring Model Through Experimental Testing of Axial Motion

Amplification and Time Delay in Air and Water

Halvor Lunde Tobro

Petroleum Geoscience and Engineering
Submission date: June 2018
Supervisor: Sigve Hovda, IGP

Norwegian University of Science and Technology
Department of Geoscience and Petroleum

Summary

Prediction of downhole movement is key to foresee surge and swab fluctuations, and the ability to maintain pressure within the boundaries of the operational window. Especially during connections, the movement of the structure is inflicted on the drillstring, as no heave compensation exists when the drillstring is set in slips. A lumped element model developed in Hovda (2017) is presented, with the ambition of predicting downhole movement as a function of only topside movement and a transfer function.

The objective of the experiments was to gather empirical data on the relationship between frequency, and both amplification and time delay. This was done by recording the behavior of harmonic oscillations by a drillstring in both air and water. The model was tested in a 66 m deep well, with an inner diameter of 68.9 mm. The drillstring consisted of 60 m of pipes with an outer diameter equal to 21.3 mm, and one joint of 6 m length with an outer diameter of 38.0 mm, to resemble a bottom hole assembly (BHA). The drillstring was oscillated by a motor, inflicting rotational motion on an offset-disc with an off-centered connection to the drillstring, above the well. Experiment frequencies ranged from 0.25 to 12.75 Hz, in increments of 0.25 Hz. It was decided not to increase frequency any further, to maintain HSE. The first resonant frequencies were estimated to 18.75 and 18.15 Hz for air and water respectively. Movement was monitored by two positional sensors on the drillstring. One directly beneath the motor, and one at the bottom of the drillstring. Initial experiments were preformed with an air-filled well. After functionality of the setup was confirmed, and sufficient data acquisition of the behaviour in air, the well was filled with water. Experiments were repeated with the new well fluid, for comparison of the difference made by changing fluid.

The obtained results were compared to the predictions first made in Tobro (2017), to determine the solidity of the model. Results proves that the model is capable of predicting amplification within a range from approximately 6 to 11.75 Hz. For frequencies below 5.25 Hz, measurements yielded an amplification of less than one in both fluids. According to model predictions, this should not occur for any frequency with low-viscous fluids as air and water. This is attributed to friction and stick-slip, influencing both amplification and delay. In experiments with frequencies ranging from 5.5 to 11.75 Hz, predictions of amplification best correspond with measurements in both fluids. At 6 and 11.75 Hz, amplification in air was predicted to 1.141 and 1.808, while measurements showed 1.114 and 1.812. In water, the predicted amplification at 6 and 11.5 Hz was 1.151 and 1.841, and the measured amplification 1.125 and 1.804. Above 11.75 Hz, an unexpected drop in amplification is seen. The cause of this drop is believed to be caused by effects outside the scope of the model, and is further discussed throughout the thesis.

A time delay was measured in experiments of both fluids, but not predicted by the model. At experiment frequencies below 6 Hz this delay is relatively large, at more than 10 ms,

which is also attributed to friction and stick-slip. For the remainder of experiment frequencies, the time delay was found to be approximately constant at 4ms. The accuracy of that number is uncertain, as it is a small number and coincides with the sampling rate of experiment setup. Friction is likely still present at frequencies above 6 Hz, and its influence could very well cause such a small delay.

A sensitivity analysis was also performed, as an effort to identify areas of improvement in the model. Results of the sensitivity analysis showed fluid forces had to be increased significantly to match simulations to the measured results. Particularly matching results by alteration of Basset forces proved impossible, as matching delay set amplification further off. This implies that exterior factors, unaccounted for by the model, bear more significance, and that some assumptions of the fluid model, such as considering the drillstring an infinite plate, should be revisited.

Samandrag

Denne oppgåva tek for seg eindimensjonal aksial rørsle i ein borestreng. Føreseieleg nedihòls rørsle er essensielt for å predikere trykksvingingar, og dermed mogleiken til å vedlikehalde trykket i botn av ein brønn innanfor rammene sett av poretrykk og frakturering strykk. Særleg når borestrengen gjerast opp, og nye borerør skal festast til den resterande borestrengen, blir rørsla frå ein flytande borerigg direkte overført til borestrengen. I desse tilfella finnast inga mekanisme for å kompensere for bølgehiv. Ein modell utvikla i Hovda (2017) presenterast, med ambisjon om å kunne føreseie nedihòls rørsle som ein funksjon av berre rørsla på toppen og ein overføringsfunksjon.

Målsettinga for eksperimenta var innsamling av empiriske data, for å stadfeste ein samanheng mellom aukande frekvens, og både forsterkning og forseinking. Dette blei gjort ved å måle posisjonen til borestrengen under påverknad av harmoniske svingingar i både luft og vatn. Modellen blei testa eksperimentelt i ein 66 m djup brønn ved NTNU i Trondheim. Den indre diameteren i brønnen var 68.9 mm. Borestrengen som blei brukt i eksperimenta var satt saman av 60 m røyr med ein ytre diameter lik 21.3 mm, og eit 6 m langt røyr med ytre diameter lik 38.0 mm, for å etterlikne BHA. Ein motor plassert rett over brønnen satt i gang svingingane, ved å påføre ein rotasjon på ei skive med ikkje-sentrert feste til borestrengen. Frekvensen på svingningane i eksperimenta strakk seg frå 0.25 til 12.75 Hz, i 0.25 Hz trinn. Ytterlegare auking i frekvens blei stoppa, grunna HMS. Fyrste resonante frekvansar blei estimert til høvesvis 18.75 og 18.15 Hz i luft og vatn. Posisjonen blei målt av to posisjonssenorar festa på borestrengen. Ein rett under motoren, og ein annan i botn. Dei fyrste eksperimenta blei utført med brønnen fylt av luft, for å sørgje for riktig funksjon av alt utstyr. Etter tilstrekkeleg data var samla inn, blei brønnen fylt med vatn. Eksperimenta blei gjentekne med same frekvensar, for å samanlikne resultat med ulike brønnfluidar.

For å analysere styrka i modellen, blei dei målte resultata samanlikna med prediksjonar først presentert i Tobro (2017). Resultata viser at modellen er i stand til å føreseie forsterkninga av rørsla for frekvensar mellom omtrent 6 og 11.75 Hz. For frekvensar under 5.25 Hz viste målingane amplifikasjon med ein faktor mindre enn ein for begge fluidane. Ut frå modellen skal amplifikasjon av nedste element overstige ein for alle frekvensar i luft og vatn. Dette tilskrivast friksjonen si rolle, med påverknad på både forsterkning og forseinking. I eksperimenta med frekvens mellom 5.5 og 11.75 Hz viser modellen seg i stand til å føreseie forsterkning med høg nøyaktigheit. Ved 6 og 11.75 Hz føreseiar modellen ein amplifikasjon på 1.141 og 1.808, medan målingar viste 1.114 og 1.812. Den predikerte amplifikasjonen i vatn ved 6 og 11.5 Hz var 1.151 og 1.841, og den målte amplifikasjonen var 1.125 og 1.804. Over 11.75 Hz viser eksperimentelle resultat ei nedgang i amplitude, som ikkje er føreset av modellen. Dette fallet er anteke å vere forårsaka av faktorar utanfor målsettinga til modellen, og blir diskutert vidare i oppgåva.

Eksperimenta viste også ei uforventa forseinking for alle frekvensane. Ved frekvensar under 6 Hz blei forseinkinga målt til over 10 ms, noko som også er tillagt friksjonen si rolle. For dei resterande eksperimenta blei forseinking målt tilnærma konstant lik 4 ms. Grannsemda av dette talet er tvilsam, ettersom det er eit lite tal og lik samplingsfrekvensen på måleinstrumenta. Friksjon er sannsynlegvis til stades også over 6 Hz, og påverknaden kan tenkast å føre til ei så lita forseinking.

Ei sensitivitetsanalyse blei også gjennomført, i eit forsøk på å identifisere modellen sine veikskapar. Resultata viste at for å tilpasse modellen og dei målte resultata krevst det ei stor auking i kreftene frå brønnfluiden. Tilpassing med endring av Basset krefter viste seg umogeleg, sidan tilpassing av forseinking forårsaka ei større endring i forsterking. Dette fortel at andre faktorar, som modellen ikkje tek høgde for, spelar ei større rolle, og at nokre av antakingane i fluidmodellen, som at borestrengen er ei uendelig plate til dømes, burde reviderast.

Preface

This thesis was conducted during the spring semester of 2018 at Department of Geoscience and Petroleum at Norwegian University of Science and Technology (NTNU) in Trondheim. It should be considered a continuation of the project report Tobro (2017).

I would like to thank my supervisor Sigve Hovda for his help with this thesis. I would also like to thank the Adwell project for financial support that permitted experiments. Additional acknowledgements are given to Noralf Vedvik and Steffen Wærnes Moen for their help related to experiment setup, as well as hardware schematics. Your help with both rigging, hardware setup and software connection was paramount for the experimental testing and the obtained results.

Table of Contents

List of Tables

List of Figures

Chapter 1

Background

1.1 Introduction

Axial motion in the drillstring is a topic of interest for several reasons. Unintended movement has the potential of causing damage to expensive downhole equipment by bit-bouncing, or worsening borehole conditions. Axial displacement also impose a force on the drilling fluid by a piston-like behaviour, especially in tight boreholes. In turn, the fluid displaced by the moving drillstring causes pressure variations downhole, known as surge and swab. The implications of controlling these pressure variations are particularly important in deep sea operations, and operations with a narrow operational window. If not accurately predicted or accounted for with safety factors, such unintended variations could cause influx or mud losses. Both require time and effort to manage. Time and effort that could be spent more productively with precautionary measures in place to avoid such occurrences. One of the main challenges of future projects in mature areas is depleted pore pressure and hard-to-reach prospects. Both of these attributes result in a more narrow operational window, and the need to maintain a stable downhole pressure. Several possible causes of unintended excitation of the drillstring exist. One possibility is whenever the drillstring is abruptly hung in slips. The abrupt stop over a short period of time is analogous to a large deceleration, which is transferred to the drillstring. According to Everage et al. (2005), this excitation could even potentially cause resonant modes in the drillstring. Incoming ocean waves on floating drilling structures is another possibility, resulting in lower frequency motion. The magnitude of the imposed oscillations depends on the frequency and amplitude of the incoming waves. In the general case with the drillstring suspended in the top drive, heave compensation absorbs this energy. However, with the drillstring suspended in slips, the energy is directly transferred to the drillstring. This augments the importance of maintaining predictable downhole pressure in areas of harsh weather conditions, such as the North Sea. Ability to predict these fluctuations in real-time has the potential to reduce unwanted incidents and improve efficiency in offshore drilling operations.

In conventional drilling processes, drilling fluid is the most important pressure control and the primary barrier towards underburden formations, according to Bourgoyne Jr et al. (1997). Drilling fluid as the primary barrier requires maintenance of mud properties by continuous addition of additives. Also associated is the limitation of a constant pressure gradient, starting from zero at the surface. Advances in Managed-Pressure-Drilling (MPD) allows the use of fluid gradients smaller than that of the formation fluid. Thus, the use of MPD has increased as a solution to narrow operational windows in deep sea operations to avoid excessive sectioning and changing mud weights, as described by Rasmussen et al. (2007), Mathew et al. (2012) and Nauduri et al. (2009). According to Aarsnes et al. (2014), it has been more extensively used from fixed platforms rather than floating rigs due to complications with surge and swab. Industry-practice in handling surge and swab from mobile drilling rigs is through safety factors and conservative pressure estimates, as summarized by Bybee et al. (2008). A proposed solution to these complications is the inclusion of a downhole choke to regulate pressure. The main disadvantage of this solution is the lack of high-speed transmission and dependency on telemetric communication, with the time delay related, as outlined by Kvernland et al. (2018). All these factors highlight the necessity of accurate predictions of axial movement, and the consequences seen in pressure fluctuations.

This thesis shortly presents a semi-analytical, lumped element model describing unidirectional movement of a drillstring imposed by a topside driving force, developed in Hovda (2017). The objective of the model is to accurately predict downhole motion by only the topside movement and a transfer function dependent on the drillstring and well fluid. Experiments have been conducted, and analysis of related empirical data is presented along with the model's predictions, first developed in Tobro (2017). The ability to predict pressure fluctuations of swab and surge is dependent on the magnitude of the drillstring movement, and the time at which it occurs. Hence, the two most important measured identities are amplification and time delay between top and bottom movement. Empirical data for the relationship between increasing frequency and these two factors are compared to the models predictions. Areas of improvement are identified by analyzing the significance of different parameters in a sensitivity analysis.

1.1.1 Background Theory

The most important parts in derivation of the model presented by Hovda (2017) are summarized and presented in the following section. The most fundamental assumption is consideration of the drillstring as a 1D-element, with inspection of motion along the axial direction. The drillstring is discretized as a set of n springs and point-masses of equal length. All length is centered in the springs of the system, while all mass is concentrated in the point-masses. Each spring has a stiffness, k_i, given by the material properties of the drillstring at element *i*, as $k = \frac{EA}{L}$. Where E is the Young's modulus of the material, A is the cross-sectional area and L is the length. Connection to the structure is through the top spring, with position $Q(0) = 0$. Coordinates of the remaining blocks are denoted as $Q_i(0)$. The distance from the equilibrium point of each point mass is denoted $q_i(t)$, and is zero in the case where every element is at rest at its equilibrium point. By use of Newton's

2. law, a relationship arises of the forces influencing each element

$$\begin{aligned} -m_1\ddot{q_1} + m_1 gBF_1 - k_1(q_1 - Q) + k_2(q_2 - q_1) + R_1 = 0, \quad &\text{for} \quad i = 1 \\ -m_i\ddot{q_i} + m_i gBF_i - k_i(q_i - q_{i-1}) + k_{i-1}(q_{i+1} - q_i) + R_i = 0, \quad &\text{for} \quad 2 \leq i \leq n-1 \\ -m_n\ddot{q_n} + m_n gBF_n - k_n(q_n - q_{n-1}) + R_n = 0, \quad &\text{for} \quad i = n \end{aligned} \tag{1.1}$$

where R_i is the viscous forces of the fluid, and BF_i is the buoyancy factor. For the case where diameter is unchanged between elements, the buoyancy factor is equal to one. This system is better described as a system of equations, on the form

$$\mathbf{M}\ddot{q} + \mathbf{K}q + \mathbf{M}g\mathrm{BF} + \mathbf{R} = \mathbf{f}(t) \tag{1.2}$$

where **R** is the resistance. **M** and **K** are diagonal and tridiagonal matrices respectively, and can be found in Appendix (D). The driving force **f**(t) is inflicted only by the structure, so it is given as $k_1 Q(t)$ for the first element, and otherwise zero. The assumption of unidirectional motion implies no contact friction, and all friction of the system attributed to fluids. This fluid friction is further assumed to originate from the viscous forces of the well fluid. The fluid is assumed incompressible and Newtonian, with the shear stress of the fluid linearly proportional to the shear strain rate. Since air and water were used for experiments, the assumption of Newtonian behaviour is well documented and often used according to Cengel (2010). The incompressibility assumption however, is rarely used for air, but commonly used for water. Flow is also assumed laminar. If not for the movement of the pipe, the well fluid would be static. Assumption of laminar flow is justified by the relatively low magnitude of frictional forces, so that the fluid motion resulting from drillstring oscillations is small, and in turn, so is the Reynolds number. As this is an axial motion, it is reasonable to assume that fluid in the vicinity of the drillstring is symmetrical in axial direction. This implies an irrotational assumption, meaning that the vorticity of the flow is negligible, also expressed as

$$\vec{\zeta} = \vec{\nabla} \times \vec{U} \approx 0 \tag{1.3}$$

where $\vec{U}$ is the velocity vector, and the curl of this velocity is the vorticity. Under the irrotational flow approximation, the velocity of the flow can be expressed as the gradient of a scalar function. Attempts to describe the viscous forces are developed based on Navier-Stokes equations given as

$$\frac{1}{r}\frac{\partial}{\partial r}\left(r\frac{\partial u_i}{\partial r}\right) = \frac{1}{\mu}\left(\frac{\partial p_i}{\partial z} - \rho_m g\right) + \frac{\rho_m}{\mu}\frac{\partial u_i}{\partial t} \tag{1.4}$$

where u_i is the axial velocity of the fluid, μ is the viscosity and ρ_m the density. After oscillations of constant frequency over a longer period of time, it is assumed that a steady-state system has evolved, and initial transient behaviour has subdued. Hence, all time derivatives of Eq. (1.4) can be neglected, and the resulting system can be solved with regards to the velocity as

$$u_i(r) = \frac{(\partial p_i/\partial z) - \rho_m g}{4\mu} r^2 + C_1 \ln(r) + C_2 \tag{1.5}$$

with constants determined by boundary conditions. For simplicity, the variable $U_i = ((\partial p_i/\partial z) - \rho_m g)/(4\mu)$ is introduced. On both radial edges, there is a no-slip assumption. That is, both along the casing wall and the edge of the drillstring. The parameter α_i is a number between zero and one that denotes the ratio between the edge of drillstring element i and the radius of the casing wall, R. Boundary conditions are thus formulated as

$$\begin{aligned} u_i(R) = 0 &= U_i R^2 + C_1 \ln(R) + C_2 \\ u_i(\alpha_i R) = \dot{q}_i &= U_i \alpha_i^2 R^2 + C_1 \ln(\alpha_i R) + C_2 \end{aligned} \tag{1.6}$$

and solved to yield

$$\begin{aligned} C_1 &= \frac{\dot{q}_i + U_i R^2 (1 - \alpha_i^2)}{\ln(\alpha_i)} \\ C_2 &= -U_i R^2 - C_1 \ln(R) = -\frac{U_i R^2 \left(\ln(\alpha_i) + (1 - \alpha_i^2)\ln(R)\right) - \dot{q}_i \ln(R)}{\ln(\alpha_i)} \end{aligned} \tag{1.7}$$

Integrating the resulting expression over the annulus cross-sectional area yields the flow rate through the well as

$$V_i = \int_{\alpha_i R}^{R} 2\pi r u_i(r) dr = \frac{\pi R^2}{2} \left(U_i R^2 (\alpha_i^4 - 1) - \frac{\dot{q}_i + U_i R^2 (1 - \alpha_i^2)}{\ln(\alpha_i)} (1 - \alpha_i^2) - 2\alpha_i^2 \dot{q}_i \right) \tag{1.8}$$

Due to assumptions of incompressibility and consequent conservation of mass, this equals the rate of flow through the drillstring

$$V_i = -\pi \alpha_i^2 R^2 \dot{q}_i - V \tag{1.9}$$

where V is the volume pumped by the mud pumps. Equalling these expressions results in the frictional forces as

$$R_i = 2\pi \alpha_i R h \mu \frac{\partial u_i}{\partial r} + R_{i,dp}(V) \Big|_{\alpha_i R} \tag{1.10}$$

where $R_{i,dp}$ is the frictional loss from flow through the drillpipe, a term that is dominated by pressure drop over the nozzles. Rewriting Eq. (1.10) as a function of q, gives

$$\begin{aligned} R_i = -2\pi h \mu \dot{q}_i \left(\frac{1 + \alpha_i^2}{1 - \alpha_i^2} \ln(\alpha_i^{-1}) - 1 \right)^{-1} + \frac{4h\mu V}{R^2} \left(\frac{1 + \frac{2\alpha_i^2 \ln(\alpha_i)}{(1 - \alpha_i^2)}}{(1 + \alpha_i^2)\ln(\alpha_i) + (1 - \alpha_i^2)} \right) \\ + R_{i,dp}(V) = -c_i \dot{q}_i + v_i(V) \end{aligned} \tag{1.11}$$

which accounts for frictional forces from the fluids. As continuous oscillations is analogous to continuous acceleration, there are other fluid forces in play as well. These are

known as added mass and Basset forces. Basset forces accounts for the previous acceleration of the pipe, and the effect of this at later stages. As is well known, viscous forces act on the interface between a solid body and the fluid. According to Schwarzkopf et al. (2011), the forming of such a boundary layer is delayed by acceleration of the body. From Hovda (2017), these Basset forces are given as

$$R_{i,Ba} = 2Rh\sqrt{\pi\rho_m\mu}\left(\frac{\alpha_i}{1-\alpha_i^2}\right)\left(t^{-\frac{1}{2}} *_t \ddot{q}_i\right) = b_i(t^{-1/2} *_t \ddot{q}_i) \tag{1.12}$$

where $*_t$ is a time convolution operator. Added mass is another fluid force inflicted by the movement of the drillstring. Added mass originates from work done by a solid body accelerating in a fluid. This work increases the inertia of the fluid in which it is submerged. Revisiting Navier-Stokes equation in Eq. (1.4), and assuming a stiff drillstring and no viscosity terms, it can be solved to yield

$$p_i = h\sum_{j=1}^{i}\frac{\partial p_j}{\partial z} = \rho_m g h i - \rho_m h\sum_{j=1}^{i}\frac{\partial u_j}{\partial t} \tag{1.13}$$

The last summation is not included in any of the previous equations. This is included as an effect of added mass. The added mass is then found as

$$a_{added} = \ddot{q_n}\rho_m\pi\alpha_1^2R^2\frac{L}{n}\sum_{j=1}^{n}\frac{\alpha_j^2}{1-\alpha_j^2} \tag{1.14}$$

which summarizes the fluid forces included in the model. All these forces can be merged and manipulated dependent on a single variable, namely the displacement of the drillpipe. Including these forces in Eq. (1.2), results in

$$-\mathbf{B}(t^{-1/2} *_t \ddot{\mathbf{q}}) + \mathbf{M}\ddot{\mathbf{q}} + \mathbf{C}\dot{\mathbf{q}} + \mathbf{K}\mathbf{q} - \mathbf{g} - \mathbf{v} = \mathbf{f}(t) \tag{1.15}$$

with gravitational and buoyancy forces included. This equation is made dimensionless by substituting $\tau = c_s/Lt$, and further reduced by a substitution of variables as $\mathbf{q} = \mathbf{y} + \mathbf{K}^{-1}(\mathbf{g}+\mathbf{v})$

$$-\frac{nc_s^{3/2}}{E\hat{a}L^{1/2}}\mathbf{B}(\tau^{-1/2} *_t \ddot{\mathbf{y}}) + \mathbf{A}_1\ddot{\mathbf{y}} + \frac{nc_s}{E\hat{a}}\mathbf{C}\dot{\mathbf{y}} + n^2\mathbf{A}_2\mathbf{y} = \frac{nL}{E\hat{a}}\mathbf{f}(t) \tag{1.16}$$

where $\mathbf{A}_1$ and $\mathbf{A}_2$ are diagonal and tridiagnoal matrices respectively, similar to $\mathbf{M}$ and $\mathbf{K}$. However, the entries of these matrices are the cross-section area of element i, divided by the geometric average of all cross-section areas. This is the case for both matrices, with $\mathbf{A}_1$ resembling that of $\mathbf{M}$, and $\mathbf{A}_2$ resembling $\mathbf{K}$. All these can be found in Appendix (D). Due to the tridiagonal structure of $\mathbf{A}_2$, the equation is not yet directly solvable. However, as both matrices make up a real, definite pair, the equation can be decoupled and solved. This is a trait for symmetric and positive definite matrices as described by Kreyszig (2010). Using eigenvalue decomposition, the following identity is obtained

$$\mathbf{A}_1 v = \lambda\mathbf{A}_2 v \tag{1.17}$$

resulting in a set of eigenvalues and eigenvectors for the system. These are denoted **D** and **V**. Using eigenvalue identities and another variable substitution of **x = Vy**, and the new matrix equation is given as

$$-\frac{nc_s^{3/2}}{E\hat{a}L^{1/2}}\mathbf{V}^T\mathbf{B}\mathbf{V}(\tau^{-1/2} *_t \ddot{\mathbf{x}}) + \ddot{\mathbf{x}} + \frac{nc_s}{E\hat{a}}\mathbf{V}^T\mathbf{C}\mathbf{V}\dot{\mathbf{x}} + n^2\mathbf{D}\mathbf{x} = \frac{nL}{E\hat{a}}\mathbf{V}^T\mathbf{f}(t) \quad (1.18)$$

where **B** and **C** are the drilling fluid force coefficients. Final decoupling is achieved by assumption of constant values along the the diagonals.

$$b_d = \frac{2RL^{1/2}c_s^{3/2}\sqrt{\pi\rho_m\mu}}{Ea_1\hat{a}}\left(\frac{\alpha_1}{1-\alpha_1^2}\right) \quad (1.19)$$

$$c_d = \frac{2\pi L\mu c_s}{Ea_1\hat{a}}\left(\frac{1+\alpha_1^2}{1-\alpha_1^2}\ln(\alpha_1^{-1}) - 1\right)^{-1} \quad (1.20)$$

Introducing some useful parameters as

$$\begin{aligned} \omega_i &= n\sqrt{D_{ii}} \\ \zeta_i &= \frac{c}{2\omega_i} \\ \kappa_{ij} &= \frac{n^2 a_1 V_{ji} V_{1i}}{\omega_i^2} \end{aligned} \quad (1.21)$$

Rearranging the Laplace transform of (1.18) results in

$$\begin{aligned} Y_j(s) = \sum_{i=1}^{n} \frac{\kappa_{ij}\omega_i^2}{-b\sqrt{\pi}s^{\frac{3}{2}} + (s+\frac{c}{2})^2 + \omega_{d,i}^2} Q_L(s) \\ + \sum_{i=1}^{n} \frac{V_{ji}(cx_i(0) + (b\sqrt{\pi}s^{-\frac{1}{2}} + 1)(sx_i(0) + \dot{x}_i(0)))}{-b\sqrt{\pi}s^{\frac{3}{2}} + (s+\frac{c}{2})^2 + \omega_{d,i}^2} \end{aligned} \quad (1.22)$$

By taking the inverse Laplace transform of Eq. (1.22), the displacement of the drillstring as a function of dimensionless time is given as

$$y_j(\tau) = Q(\tau) *_\tau s_{1,j}(\tau) + s_{2,j}(\tau) \quad (1.23)$$

Which is solveable by Fourier transform, and where $s_{1,j}$ and $s_{2,j}$ are given by

$$\begin{aligned} s_{1,j}(\tau) &= \sum_{i=1}^{n} \mathscr{L}^{-1}\left(\frac{\kappa_{ij}\omega_i^2}{-b\sqrt{\pi}s^{\frac{3}{2}} + (s+\frac{c}{2})^2 + \omega_{d,i}^2}\right) \\ s_{2,j}(\tau) &= \sum_{i=1}^{n} \mathscr{L}^{-1}\left(\frac{V_{ji}(cx_i(0) + (b\sqrt{\pi}s^{-\frac{1}{2}} + 1)(sx_i(0) + \dot{x}_i(0)))}{-b\sqrt{\pi}s^{\frac{3}{2}} + (s+\frac{c}{2})^2 + \omega_{d,i}^2}\right) \end{aligned} \quad (1.24)$$

Chapter 2

Experiments

2.1 Rig up

Experiments were conducted at a NTNU laboratory hall in Trondheim, using a well on site at the laboratory. This well is previously used for other experiments, and cased with a 10 inch casing. It is 94m deep, and considered perfectly vertical. Above the well stood a scaffolding, with computers for monitoring downhole equipment, and control system for the motor.

2.1.1 Casing

Initial experiment preparation was the installation of a new casing in the well. New casing served two different purposes. The first being that the full length of the well was not planned to be utilized, so the new casing was closed-end, to shorten the effective length of the well. Effects of fluids are enhanced by shortening the distance from the end of the drillstring to the bottom of the casing. Reduction in distance between drillstring and well bottom leaves less room for fluid to escape after excitation of the drillstring. In a drilling process, the drillstring is mostly situated near the bottom of the well, making the experiments more realistic. The other purpose of a new casing was a reduction in inner diameter, to minimize the clearance between drillpipe and casing. Simulations of both Hovda (2017) and Tobro (2017) have shown that the effects of added mass on pressure increase significantly in a narrow hole. The different configurations of drillpipe used for experiments all had diameters less than 38 mm. A casing inner diameter equal to 68.9 mm was decided to best fit this purpose. Casing joints of 6 m were laid out on the rig floor, and inspected for any visible damage, especially on connections. As initial experiments were conducted in an air-filled well, and the original casing in place was water-filled, it was important to ensure the sealing of all connections. A threadlocking adhesive named Loctite 243 were applied to all connections to keep liquids out of the casing. Additionally, the adhesive prevents loosening and chemical degradation of connections. Before applying the grease, connections were cleansed using 2-propanol, to ensure proper fastening of

connections. A movement sensor was installed at the bottom of the first casing element, with cable connected on the outside of the casing through the lower part of a T-joint on the bottom threads as seen in Fig. (2.1). The sensor installed was a magnetostrictive sensor, further described in Section (2.1.3). A hose was connected to the bottom T-joint to allow for circulation of fluid through the casing during experiments. A lifting cap designed for the threads of the casing was connected to the top threads of the joint, and to a traverse crane. The joint was then hoisted using this crane, lowered into the well, and hung off in slips. The same procedure was repeated for the next joint, which was connected to the joint in the slips, before being lowered into the well and hung off. Connections were made by hand, and tightened by use of a chain wrench. On the third casing joint, a pressure sensor was placed at the top connection through a T-joint. This sensor was connected by a cable running on the outside of the casing, along with the cable connected to the bottom movement sensor and the circulation hose. This first pressure sensor was placed three full joints above the bottom of the casing, equalling an 18 m distance. The next pressure sensors were connected similarly with a spacing of three joints (18 m), making up a total of three pressure sensors in the well. The full casing with all sensors is displayed in Fig. (2.6). The cables connecting these three pressure sensors to the computer topside ran parallel to the casing along with the bottom movement sensor and the circulation hose. These were all attached to the casing using zip ties every meter or so, to keep cables still. The final length of the casing was 66 m, consisting of 11 full joints of 6 m each.

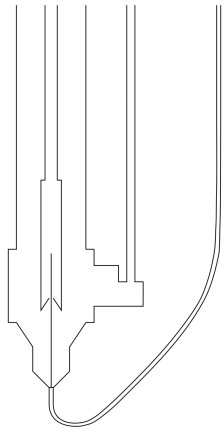

Figure 2.1: Bottom casing schematic

2.1.2 Drillstring

The first drillstring element was a hollow-end pipe with a custom-made funnel attached to the end through a crossover. The joint was stainless steel of the type AISI 304, grade E235, and delivered by Smith Stål. This is a non-magnetic alloy with chromium, to avoid interference with the magnetostratic sensor. The outer diameter of the pipe was 38 mm, with a wall thickness of 2 mm. The funnel served the purpose of guiding the drillstring

to the bottom sensor rod in the casing, as seen in Fig. (2.1). All pipes used in the experiments were assumed to have a Young's modulus equal to 210 GPa, found from Irgens (2006). The remainder of the drillstring was smaller diameter pipes, so the bottom element is considered analogous to the BHA of the drillstring. Connection to the pipe above was through a cross-over. The drill pipe used for experiments are referred to as 1/2" drillpipe. This pipe is made of ground material and grade S195, and is delivered by Ahlsell. In total, 10 whole joints of this type of pipe, and an additional amputated joint with connection to the motor, made up the full drillstring. In total, this amounted to a drillstring with 11 joints of 6 m each, in addition to and amputated joint, the 4 cm funnel and two crossovers of 3 cm and 2.5 cm respectively. These minor components are considered as part of the bottom joint by addition of extra length in simulations. The full length of the drillstring was equal to 66.9 m. All pipe joints were installed according to the procedure described for installment of the casing. Drill pipes were laid out on the rig floor and inspected. Threads of the drillstring were cleaned using 2-propanol, and sealed with adhesives to ensure sufficient strength of connections. Another lifting cap designed for the size of threads on the drill pipe, was connected to the top, and the traverse crane used to connect to the drillstring. Due to the severe vibrations from the oscillating drillstring, the driving motor was placed on a frame above the well. This reinforced the structure, and considerably reduced vibrations at the surface. The frame measured 150 cm above the well, making the total distance from motor to casing bottom equal to 67.5 m. This is supported by measurements of the drillstring position, which show the end of the string resting 60 cm above the bottom of the casing at equilibrium. Additional information on all pipes used for experiments can be found in Table (2.2). The drillstring in its entirety can be seen in Fig. (2.2), and all components are listed in Table (2.1). Schematics for both crossovers and the funnel can be found, along with pictures of the rigging process in Appendix (E).

Joint nr	Type	Length [m]	OD [mm]	ID [mm]	Weight [kg/m]
1	1/2" DP	0.78	21.3	14.9	1.46
2	1/2" DP	6.00	21.3	14.9	1.46
3	1/2" DP	6.00	21.3	14.9	1.46
4	1/2" DP	6.00	21.3	14.9	1.46
5	1/2" DP	6.00	21.3	14.9	1.46
6	1/2" DP	6.00	21.3	14.9	1.46
7	1/2" DP	6.00	21.3	14.9	1.46
8	1/2" DP	6.00	21.3	14.9	1.46
9	1/2" DP	6.00	21.3	14.9	1.46
10	1/2" DP	6.00	21.3	14.9	1.46
11	1/2" DP	6.00	21.3	14.9	1.46
12	Cross-over	0.040	38.0	28.0	1.78
13	1 1/2" BHA	6.00	38.0	34.0	1.78
14	Cross-over	0.025	38.0	22.5	1.78
15	Funnel	0.035	38.0	13.0	1.78

Table 2.1: List of all drillstring components

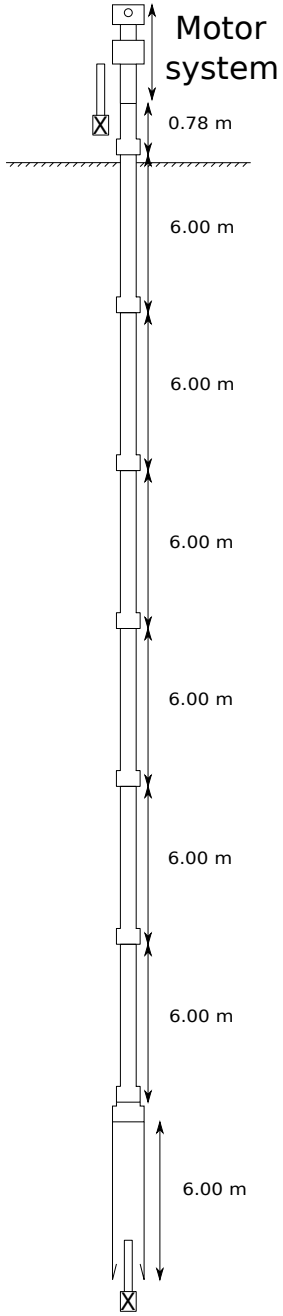

Figure 2.2: Drillstring schematic. Sizes are not in realistic proportion for illustrative purposes

	Serial number	Length [m]	OD [mm]	ID [mm]	Area [mm^2]	Weight [kg/m]	Density [kg/m^3]
Drill pipe "1/2 inch"	1001207	60.78	21.3	14.9	182.0	1.46	8023.7
BHA "1 1/2 inch"	Smith Staal	6.00	38.0	34.0	226.2	1.78	8023.0
Casing "3 inch"	1001021	66.00	76.1	68.9	820.0	6.63	8085.8

Table 2.2: Characteristic information about pipes used for experiments

2.1.3 Sensors

In order to experimentally decide a relationship between movement at both ends of the string, positional readings were needed at both places. Two magnetostrictive positional sensors with different measuring length were delivered by Balluff. Magnetostrictive sensors operate by utilizing ferromagnetic properties of the sensor material. Examples of such materials are nickel, cobalt and iron. In the presence of a magnetic field, the material itself changes physical properties. As the electrons of the metal is oriented along the axis of the magnet, it causes stress, and the body undergoes elongation or compression on a small scale. A magnetostrictive sensor is composed of a housing at one end, in which all processing electronics are contained. This housing is connected via cable to the computer registering measurements on one end, and to a sensor rod on the other end. This sensor rod could further be divided into two parts; the nominal length and the damping zone. The sensor rod is a transducer that includes a waveguide protected within the rod. When the drillstring is set in motion, the magnet attached travels along this waveguide, generating a magnetic field. An induced current pulse sets off a torsional wave along the waveguide, which propagates with sonic speed. When this wave reaches one end of the waveguide, the wave is transformed into an electric output signal that is transmitted as the output data. The waves that travel the opposite direction reach the damping zone. These waves are absorbed to avoid reflection. The time differential needed for the sonic wave to reach the end of the rod determines the distance to the magnet, and hence the location of the drillstring. To summarize, measurements show the location of the magnet attached to the drillstring, by use of torsional waves in the waveguide of the sensor rod. This type of sensor is displayed in Fig. (2.3).

The sensor specifications are listed in Table (2.3). The sensor is designed for use in pressurized hydraulic environments, as it has a hermetically sealed aluminum housing. Thus the same sensor could be used regardless of fluid in the casing. The sensor was also resistant to shock and vibrations, which is a convenient feature in experiments of oscillating metal tubes. The operating analog output signal of the sensor ranged from 4 to 20 mA, with a measuring length of 1000 mm. To convert this output analog signal into digital measurements, scaling was needed. This scaling is on the form $f(x) = ax + b$, where x is the output current, and $f(x)$ is the displacement distance. The sensor measures relative movement. At 4 mA output signal, the sensor measures 0 mm displacement, while 1000

Figure 2.3: Bottom positional sensor. From Balluff (2018)

mm is measured at 20 mA. The slope and intersection were found as follows

$$a = \frac{ML}{\Delta I} = \frac{1000\text{mm}}{16\text{mA}} \tag{2.1}$$

$$b = f(4) - 4a = -\frac{1000\text{mm}}{16\text{mA}} 4\text{mA} = -250\text{mm} \tag{2.2}$$

Because of linearity between the output signal and the displacement, this results in a final conversion scale as $f(x) = \frac{1000x}{16}\text{mm/mA} - 250\text{mm}$. The conversion scaling utilized in LabView is shown in Fig. (2.4).

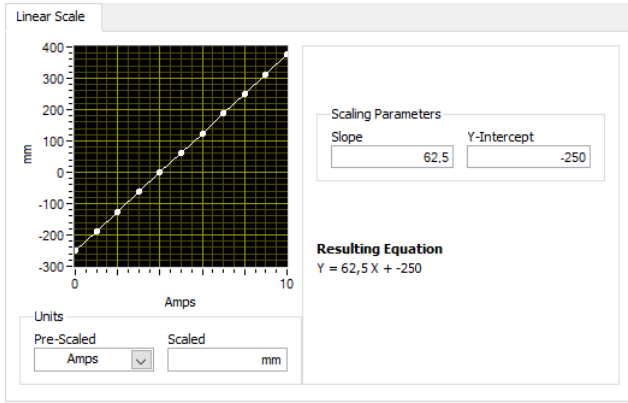

Figure 2.4: Conversion scale of bottom sensor

The most important difference between the top and the bottom sensor was the measuring length. The top sensor had a measuring length of 200 mm. This sensor was attached to the frame which the motor rested on, directly besides the drillstring, as shown in Fig. (2.2). Due to the difference in measuring length, the scaling was correspondingly different. Conversion scale for this sensor is found similarly as the bottom sensor, with

Placement	Bottom Sensor	Top Sensor
Product name	BTL7-E100-M1000-B-KA05	BTL7-E500-M0200-B-S32
Measuring length	1000 mm	200 mm
Pressure rating	600 bar	600 bar
Max sampling frequency	1000 Hz	4000 Hz
Analog output	4 - 20 mA	4 - 20 mA
Operating voltage	24 V	24 V
Repeat accuracy	$\pm$ 5 μm	$\pm$ 5 μm

Table 2.3: Sensor specifications

only measuring length different between the two. This conversion scale is found to be $f(x) = \frac{200}{16}$mm/mA $- 50$mm. LabView conversion scale is included in Fig. (2.5).

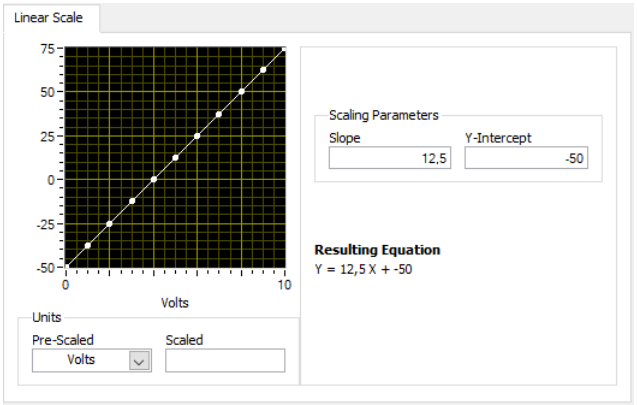

Figure 2.5: Conversion scale of top sensor

One accelerometer was placed near the bottom of the string, and another attached at the top. Both accelerometers are of the type MPU-6050 from InvenSense, with specifications listed in Table (2.4). These are 3-axis accelerometers and 3-axis gyroscopes. In addition to measuring acceleration of the string, the accelerometer also includes temperature measurements. The placement of sensors can be seen in Fig. (2.6).
Pressure variations were also monitored, with three pressure sensors placed evenly spaced inside the casing. One at the bottom, one in the middle and one at the top. Sensors of type UNIK 5000 from GE were used for the experiments. These are 12 bit sensors, with an operating range from 0 to 10 bar, a sampling frequency of 80-100 kHz, and a sensitivity of about 0.15 mbar.

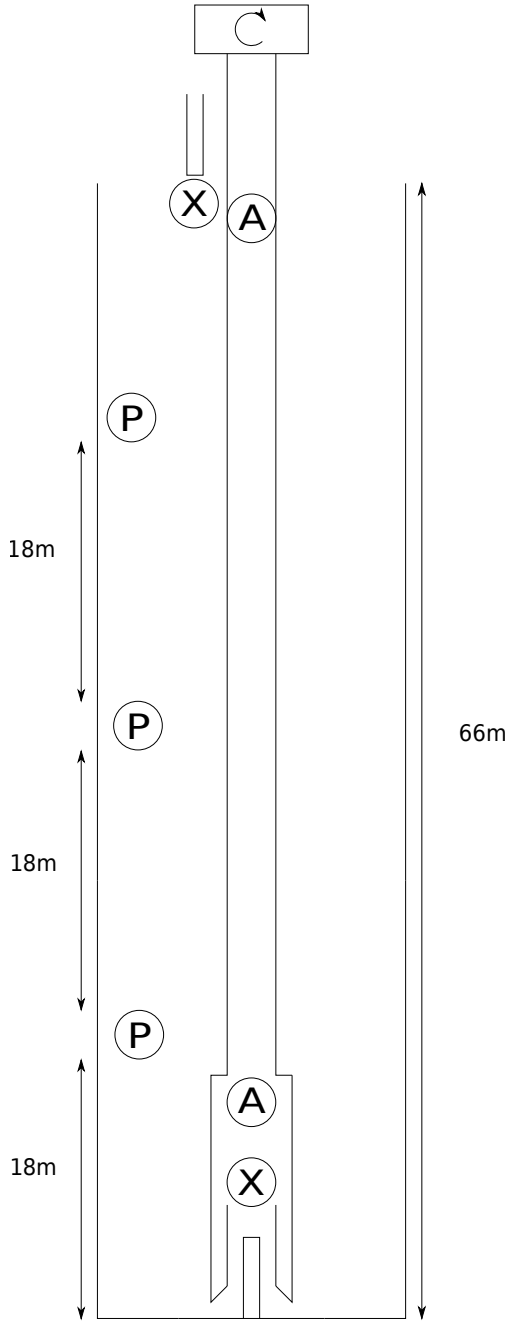

Figure 2.6: Location of positional sensors (X), pressure sensors (P) and accelerometers (A) in the well. Not in realistic proportions, for illustrative purposes

Gyro Full Scale Range [deg/sec]	±250	±500	±1000	±2000
Gyro Sensitivity [LSB/deg/sec]	131	65.5	32.8	16.4
Gyro Rate Noise [dps/$\sqrt{\text{Hz}}$]	0.005	0.005	0.005	0.005
Accel Full Scale Range [g]	±2g	±4g	±8g	±16g
Accel Sensitivity [LSB/g]	16384	8192	4096	2048

Table 2.4: Accelerometer and gyroscope specifications

2.1.4 Driver and Module

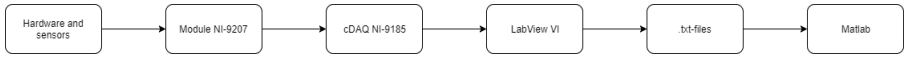

Figure 2.7: Data flow

Communication between hardware and LabView software was through a compactDAQ (cDAQ) and a National Instruments (NI) module. The cDAQ used for experiments was of type NI-9185. A cDAQ is a data acquisition platform, that controls the synchronization of input/output from the module connected to the sensors and the computer used for cataloguing data. The cDAQ communicates with the computer on site, and with the sensor through the module. Connection with the computer was through Ethernet cable, enabling sampling frequencies in the magnitude of millions per second. The module connected was of type NI-9207. This is a 16-channel current and voltage input module. The module includes an internal resistance for conversions, and a built-in rejection of noise at frequencies of 50 and 60 Hz. These frequencies are set to limit the effect of electrical noise in the system. Specifications of the module listed a sampling rate of 500 Hz per input channel.

2.1.5 Motor and Hoisting System

Oscillations of the pipe were initiated by a motor directly above the well. An offset disc, as seen in Fig. (2.8) was connected to the motor. Rotational motion of the motor forces rotation on this offset disc, which in turn is transferred to the drillstring as a vertical motion. The motion is caused by the off-centered connection from disc to drillstring. As an effort to reduce the lateral component of these oscillations the pipe was guided through a seal with low horizontal clearance in the drill floor and into the well. The frequency of experiments were governed by the frequency of the motor. The motor had a maximum operating power of 5.5 kW, corresponding to approximately 7.4 horsepower. A schematic of the motor is seen in Fig. (2.9). The maximum frequency of the motor was 1435 rpm. While the motor governed the frequency of experiments, the amplitude was governed by the eccentric connection to the offset-disc. Experiments were conducted with amplitudes of 10 mm and and 0.5 mm. Communication with the motor was through a Siemens control system, from which frequency could be administered in increments of 15 rpm. The motor was welded on top of a frame to reinforce the structure and reduce topside vibrations. Pictures of the final topside outlook can be found, along with pictures of the rigging process,

in Appendix (E).

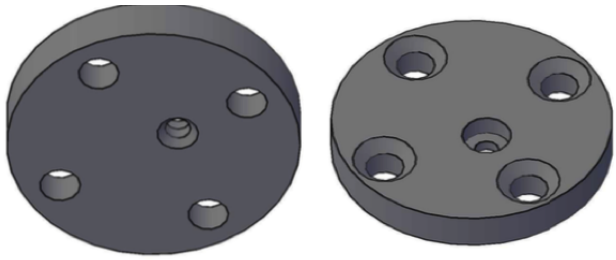

Figure 2.8: Offset-disc schematic by Vedvik and Moen 2017

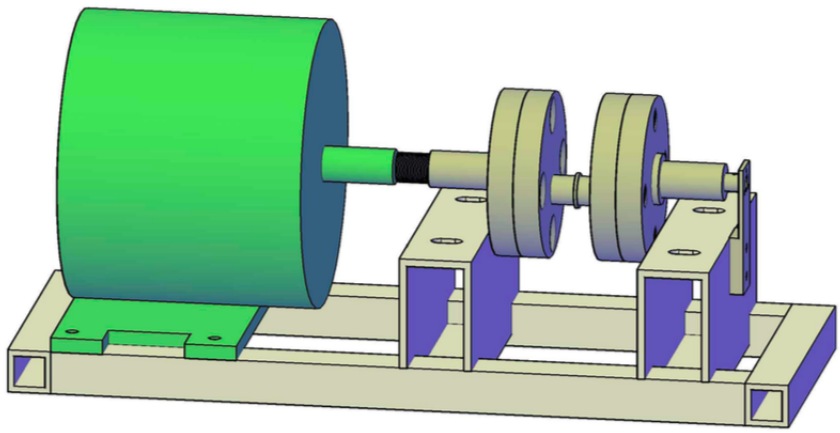

Figure 2.9: Motor schematic by Vedvik and Moen 2017

2.2 Experiment Procedure

Experiment procedure was attempted kept as constant as possible throughout all experiments. This was for easier reproducability and minimization of systematic error on behalf of the one conducting experiments. The procedure can be summarized in the following simple steps:

1. **Starting motor system -** The motor system was started from the scaffolding and the Siemens control system. Frequency was gradually increased to desired level.
2. **Starting data acquisition -** The LabView file was started from the computer located right next to the motor control panel. This application monitored and stored data, and is further described in Section (C).

3. **During experiments -** Experiment duration was attempted kept equal to approximately 100 s for all experiments. After sufficient duration of the experiment, the LabView application was stopped, and the data written to file.

The first rig-up included a 10 mm amplitude offset-disc. Initial experiments were run at frequency below 60 rpm to ensure proper function of all equipment. Afterwards, frequency was increased in increments. During experiments, the measurements were monitored in real-time on the LabView front panel, as a HSE measure. In case of any unintended incidents, there was an emergency stop button situated above the well. However, the most important HSE measure was listening. At a level of about 300 rpm, loud noises could be heard from the well, with the sound of steel hitting steel. Due to the presence of connections in both the drillstring and the casing, it was decided not to increase the frequency any further at this amplitude. This is due to the risk of connections getting stuck, and the drillstring ripping apart. The root cause of the noise unknown, but it was likely caused by a laterally induced movement from the motor, that was not sufficiently eradicated by the seal on top of the well. Due to the small diameter pipes, there was little stiffness in the material between connections, so that small lateral oscillations experienced amplification with increasing depth. In addition to the increased HSE risk, the vibrations induced by collision with the casing wall also manifested in measured results. A combination of these factors led to the decision of reducing the amplitude of the movement. A new offset disc with an amplitude of 0.5 mm was ordered from the machine shop. Issues of noise were significantly reduced with the new amplitude. Hence, this amplitude was used for the majority of experiments. Experiments were also run with with this amplitude in air to ensure the functionality of the setup. At least two experiments were preformed with frequencies at every increment from 105 to 765 rpm. Results are based on average values of these experiments. At frequencies above 765 rpm, the noise originating from the well increased significantly once again, so efforts of obtaining measurements at higher frequencies were aborted. As this is within the range proposed in Tobro (2017), it was deemed sufficient for the purpose of a first time experimental testing of the model.

After several experiments had been conducted at each frequency, the well was filled with water. As there was no way of emptying water from the well afterwards, it was important to ensure the functionality of the system beforehand. Water was the main focus of the experimental testing as this is much more comparable to the environment encountered in a drilling process. Additionally, two different fluid types allows comparison of results, for a better understanding of the fluid model proposed. The experimental procedure remained the same with the new fluid in place. Two experiments were conducted at every frequency step, and the output averaged in the display of results. This amounts to a total of almost 200 experiments used in the final presentation of results.

Chapter 3

Data Acquisition and Processing

3.1 Data Acquisition

3.1.1 LabView

LabView was chosen for development of the control system. LabView is a system-design platform and a visual programming language. Programming is preformed and executed in a flow chart-like manner. A LabView Virtual Instrument (VI) was written to acquire measurements to the cDAQ and write the data to a .txt-file. This was done by a loop that obtained measurements from both sensors at a rate of 250 Hz. Results were plotted real-time on a simple xy-plot to monitor movement during experiments, as a HSE precaution. Additionally, maximum displacement within the last 10 seconds was written to screen, to make sure that the amplification of the movement did not force the drillstring to hit the bottom of the casing. This also ensured that resonance was avoided, and a steady-state periodic motion seen, rather than ever increasing amplitudes. When the recordings were stopped, another VI was called to write the measured data to a .txt-file. The frequency of the experiment and a comment describing the experiment was input by a pop-up window. The file name was generated by the date of experiment and the experiment number of that day. This was used to catalogue the data, and for easier systematization of previously collected data. The LabView VIs can be found in Appendix (C).

After the .txt-file had been acquired, additional data processing was needed. Matlab was decided to best fit this purpose, as all simulations had been preformed using Matlab.

3.2 Sensor Uncertainty

Some uncertainties exist related to data acquisition. Although sensor specifications listed 1000 Hz and 4000 Hz as the maximum sampling rate, duplicated measurements were obtained at these rates. A sampling rate of 250 Hz was found to be the highest rate at which duplicates were not recorded. After consultations with both NTNU employees and

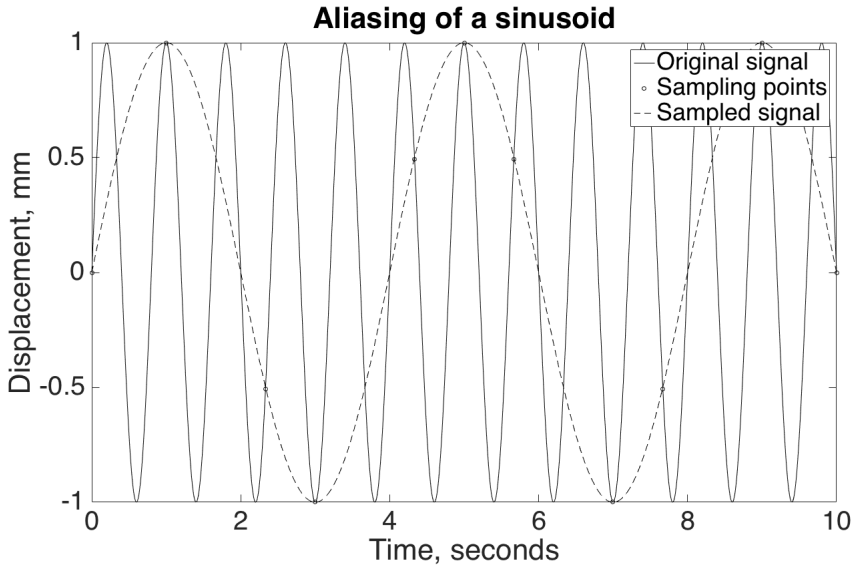

Figure 3.1: Irregularly sampled sine curve and wrongly interpreted signal

National Instrument representatives, it was suggested that the driver was the most probable limiting factor. A 250 Hz sampling rate was deemed sufficient, as maximum frequency of experiments were 800rpm, equivalent to 12.5 samples per sine-period. This is well within the boundaries set by the Nyquist-Shannon theorem from Kaiser and Reed (1977). The theorem states that for reconstruction of a periodic signal, sampling should occur at least twice as fast as the highest frequency of the function that is sampled, formulated as

$$\Delta t \leq \frac{1}{2f_{max}} \tag{3.1}$$

Where Δt is the required sample spacing needed to avoid aliasing. Aliasing occurs whenever the sampling rate is too low, so that a distinct signal becomes indistinguishable from others. A sampling of almost twenty times experiment frequency was well within this requirement. Hence, aliasing as seen in Fig. (3.1) was avoided. It should also be noted that even though sampling rate was set to 250 Hz, samples were not uniformly distributed, but rather followed the sampling rate as an average distribution. In Table (2.3) the repeat accuracy of the sensors is listed. The repeat accuracy is the consistency at which the sensor is able to reproduce the same output signal for identical measurand. That is, how similar the output value is for the exact same position of the drillstring. It was discovered that the uncertainty of the sensors, with the bottom sensor in particular, was larger than expected. An effort was made to quantify the sensor uncertainty by acquiring measurements of a static drillstring over a long period of time. At the time of acquisition, the drillstring had been static more than 24 hours, so the possibility of posterior effects by experiment oscillations could be excluded.

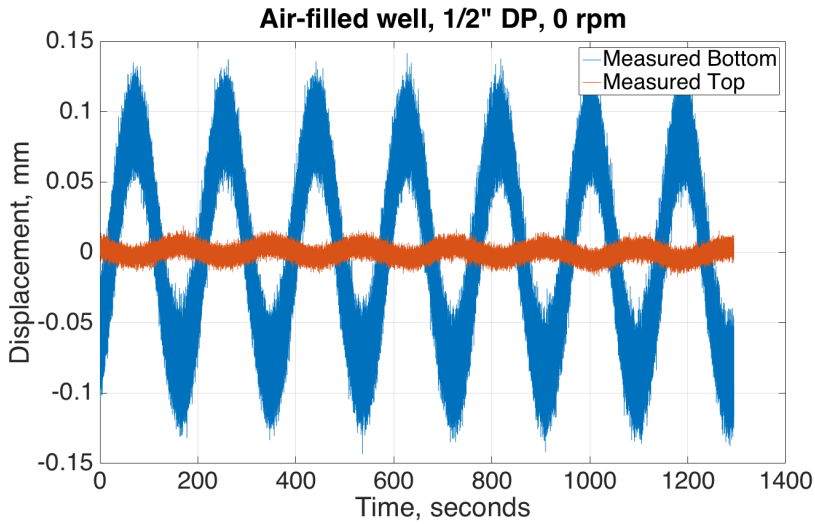

Figure 3.2: Uncertainty of both sensors

As is evident from this Fig. (3.2), the top sensor showed expected results, with some quivering around a relatively stable value. The bottom sensor however showed high frequency fluctuations with higher amplitude, in addition to a more low frequency periodic behaviour. This low frequency oscillation were present with the top sensor as well, but on a much smaller scale. The result of this behaviour is an uncertainty in measurements that far exceeds the product specifications. Additional sensor uncertainty presents a supplementary systematic error to the system. The cause of the uncertainty is unknown, but it is suspected that the additional distance from the bottom sensor to the data acquisition platform enlarges the effect, explaining why the bottom sensor was more heavily influenced. Based on the figure presented, the low frequency noise had a period in the range of 250s. This excludes the possibility of the noise being electrical, as electrical noise follows the same frequency as the power grid, at 50 Hz. Both the sensor retailer and the sensor manufacturer were consulted for advice on the issue, but were both unable to give any constructive feedback. The actual uncertainty of the sensors was quantified by finding the standard deviation of the still measurements. From Abdi (2007), this was calculated as

$$\sigma = \sqrt{\frac{1}{n-1}\sum_{i=1}^{n}(y_i - y_{avg})^2} \tag{3.2}$$

where y is the position measured at the sensor. Results from the procedure are found in Table (3.1). The uncertainty of the top sensor was in the same order as expected, while the bottom sensor uncertainty was much higher. As experiments would be preformed with amplitudes of 0.5 mm, there was a need to reduce the uncertainty. A standard deviation of 63μm corresponds to more than 12% of the amplitude value, which is too large to accurately determine any amplification.

Sensor	Value
σ_{top} [μm]	4.1743
σ_{bot} [μm]	63.022

Table 3.1: Estimated standard deviation of sensors

3.3 Data Processing

To minimize the influence of noise, it was decided to apply a high-pass filter on the data set. The procedure of smoothing experimental data by use of filters is commonly used with experimental data according to Kaiser and Reed (1977). Filtering techniques utilize that signals usually consist of multiple frequencies, which can be decomposed by Fourier analysis. Through spectral analysis, the periodic signal is broken down to a spectrum of frequencies, by a fast-Fourier transform (FFT) as described by Lee (2009).

3.3.1 High-pass Filter

As the name implies, a high-pass filter is designed to let the higher frequencies above a specified threshold value pass through. Frequencies lower than this threshold are damped so that they are effectively filtered out of the output signal. The upper threshold is limited by the Nyquist-Shannon theorem, as the highest frequency that can possibly be singled out by a FFT is the Nyquist frequency, formerly described. Two common disadvantages of running experimental data through high-pass or low-pass filters is time-shift and amplitude alteration. Frequencies below the cutoff are attenuated, while the higher frequencies pass through. With an ideal filter, all frequencies above the cutoff threshold would be removed. Such an ideal filter is visualized by imagining a rectangular function in the frequency domain, multiplied with the signal frequency domain. However, an ideal filter requires an infinite time-span of the signal, and is therefore unobtainable. The filter is approximated by truncating into a finite impulse response of N terms, resulting in a filter of $2N+1$ terms. This causes the filtered signal to be shifted in the time domain, as knowledge of the future behaviour is needed, since it is of finite duration. In reality, the frequencies in the region of the threshold is damped or even amplified slightly, while significantly higher frequencies undergo more damping, as described by Kaiser and Reed (1977). The truncation of the filter signal is visualized as a Gibbs-phenomenon square wave signal. This is also the reason why amplitude alteration of frequencies nearby the cutoff is seen with filters, and the reason why this topic needs additional consideration in an experiment where amplitude amplification is of the essence. With regards to time-shift from the filter, the importance of relative time should be emphasized. As the entire data set of measured movement is shifted equally, the relative time between data points is unaffected. The absolute time of experiments is of no significance, and with the relative time preserved after filtering, the time-shift of the filter does not influence the obtained results. As amplification was to be decided as a function of frequency, any amplitude alteration should be avoided. A Butterworth filter was chosen, as this type of filter optimizes the conservation of amplitude within the passband, first described by Butterworth (1930).

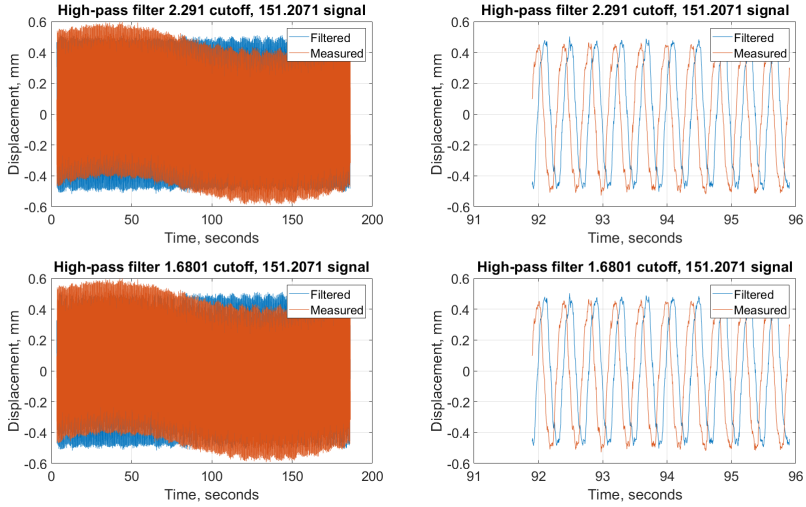

Figure 3.3: High-pass filter with different cutoff frequencies

The effect of the high-pass filter is shown in Fig. (3.3). This figure presents the effect of different cutoff frequencies. The full effect of the filter is more apparent in the left part of the figure, on a macroscopic level. The conservation of amplitude is seen in the zoomed data points to the right. The low-frequent unknown noise was effectively removed by the filter, whereas high frequency noise still remains.

The high-pass filter was created using Matlab functions, but are based on the works of Butterworth (1930). Although Butterworth filters are designed to keep frequencies in the passband as flat as possible, the amplitude alteration was minimized by filter settings. Settings include cutoff frequency, passband ripple and stopband attenuation. These settings were decided by trial and error, and analysis of filter visualization. The magnitude response and phase shift caused by filtering was inspected with Matlab's filter visualization tool. A Matlab function was written as an additional safeguard, to ensure the conservation of amplitude and keep track of any modification with regards to results validity. The absolute minimum and maximum displacement could not be utilized since the low frequency noise gives additional magnitude to this displacement. Due to the very low frequency of the noise, it is assumed that the contribution to extra displacement in one single wave is insignificant. This function considers the maximum and minimum value between every second zero-crossing of both the filtered and unfiltered data set. The least square difference, calculated by Eq. (3.5), was found between the filtered and unfiltered value. In other words, the wave top and wave bottom of each wavelength is examined to ensure the equality of these values.

In terms of signal processing, the experiment frequency was relatively low at all times. The maximum experiment frequency was less than 800 rpm, corresponding to less than

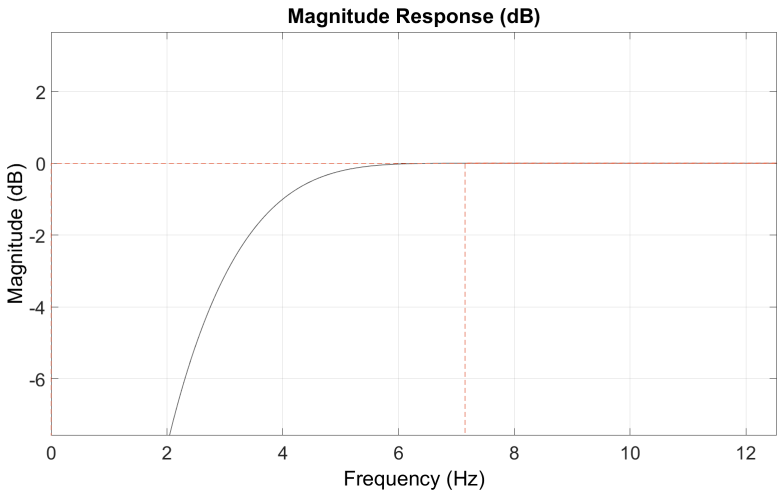

Figure 3.4: High-pass filter visualization

15 Hz. Cutoff frequency was found to be a function of the experiment frequency. The cutoffs resulting in minimization of amplitude alteration for each experiment frequency, was found by applying the filter to the entire set of experimental data and running through the Matlab function described. Minimized least square differences were obtained for $\frac{10}{11}$ times experiment frequency in experiments below 400 rpm, and $\frac{10}{14}$ in the cases above. The passband ripple was kept small and close to zero to minimize magnitude amplification of the frequencies within the passband. Stopband attenuation was set to 80 dB, as all frequencies below the threshold should ideally be removed.

3.3.2 Low-pass Filter

After the data set was filtered through the high-pass filter, some high frequency noise remained. High frequency contamination is commonly seen in experiments where measurements of analog parameters are converted into digital data samples, according to Kaiser and Reed (1977). With the sensor repeatability stated in Section (2.1.3), it was expected that the movement is not found as a perfect sinusoidal function. Especially lower experiment frequencies show more noise remaining after initial filtering efforts. A low-pass filter was constructed as a solution. The functionality of a low-pass filter is opposite that of the high-pass filter. Similar to the high-pass filter, it was created in Matlab, with built-in functions based on the Butterworth filter. A disadvantage is that low-pass filters are more prone to amplitude alteration. This is an even bigger issue, as the passband of the low-pass filter is much more narrow, with experiment frequencies from 1 to 15 Hz. Because of the risk of amplitude alteration, it was decided not to use the low-pass filter in the presented results.

3.4 Sine Matching

One of the key elements of connecting measurements to simulated predictions is the accurate description of a driving force. Different approaches were tried to accurately describe the motor driving force. Initial efforts were made by using the top sensor measurements as a representation of the driving force. As the sensor is placed directly beneath the motor, the positional readings are considered an accurate representation of the motor movement. In a real-life situation, this is analogous to the force exerted by the structure of the floating rig. The underlying assumption is that due to the small distance between motor and sensor, the stiffness of the material between is sufficient, so the measurements accurately describes the movement of the motor. With an abrupt start to a high frequency, the derivative of the first points causes the Fourier transform of Eq. (1.23) to spike. Adding a smooth build up to the measured frequency solved this behaviour. However, utilizing the measured points directly thereafter still resulted in complications in the Fourier transformation. As the data is irregularly distanced and carries several frequencies, it was tried to smooth the data set using splines and resampling to increase resolution. Additional points in between measurements were found by piecewise cubic Hermite interpolating polynomial (pchip) in Matlab. Every piece of the interpolation is found by the value of the points, and the derivative estimated from these points in the domain level, as found from De Boor et al. (1978). The Matlab function uses an harmonic average over these points, and does not overshoot the data. The resulting function is smooth and derivative, at least to the first order. This effort proved unsuccessful, as the spline resulted in higher degree polynomials between the measured data points. The Fourier transform of this is interpreted as high-frequent noise materializing in useless results.

Due to the erratic behaviour described, it was decided that sine matching the signals was a better solution to increase resolution and accurately describe the measured motion. This is due to the smoothness needed for Fourier transforming the signal, and solving the convolution in Eq. (1.23). By sine matching the data, an infinitely derivable expression is obtained, and additional frequencies in between data points are avoided. This was done by optimizing four parameters of the following expression

$$f(s)_i = s(1)\sin(\frac{2\pi t_i}{s(2)} + \frac{2\pi}{s(3)}) + s(4) \tag{3.3}$$

As seen from Eq. (3.3), these four parameters are amplitude, period, phase shift and offset respectively. The correct values of these four parameters were found by a Least-Squares optimization, as described by Wolberg (2006). The difference between the sine function and the measured value at each time stamp, the residual, was found as

$$r(s)_i = \{f(s)_i - y(t_i)\} \quad i = 1, 2, 3...n \tag{3.4}$$

where $y(t_i)$ is the position at time step *i*. The sum of the squared residual, *S*, was minimized over the entirety of the data set by varying s.

$$S = \sum_{i=1}^{n} r(s)_i^2 \tag{3.5}$$

resulting in parameter values of s(1), s(2), s(3) and s(4). The result of this procedure is seen in Fig. (3.5), and the procedure can be found in Appendix (3.5). Due to the complexity of optimizing four parameters in data sets of more than 250 000 measurements, some relatively accurate initial estimations was required. These estimations were found as follows

1. **Amplitude -** Amplitude was estimated by finding the maximum and minimum value noted in the data set, subtracting these and dividing by two.

2. **Period -** Period was estimated by multiplying the vector containing all measurements with the same vector shifted one index. That is, vector element *i* was multiplied with element *i+1*, while *i+1* was multiplied with element *i+2* and so forth. Thus, if one element and the next had the same sign, the resulting vector element would be positive. If the position changed sign between the two data points, the new vector would contain a negative value. From these preliminary results, a boolean vector was found by making all positive elements of the vector zero, and all non-positive entries one. The time corresponding to these one-entries of the boolean vector was averaged, resulting in an estimated period.

3. **Phase shift -** Phase shift showed to be the most sensitive estimation. A for-loop with different estimates of phase shift was run. The sum of Eq. (3.5) was stored for each of the estimated phase shifts, and the s yielding the smallest residual was saved for further use.

4. **Offset -** The offset of the measurements was found by adding the maximum and minimum measurement of the data set, as this proved more accurate than averaging the data set.

In the case of an abruptly started driving force, the Fourier transformed signal results in spiky initial behaviour. As measurements were started after the system had reached a constant frequency, there was a need for some numerical manipulation. Initial transient behaviour of the Fourier transformed signal is avoided by making sure that both the first point and its derivative is zero. This is achieved by the smoothstep function described in Tobro (2017) as

$$S_N(t/c)\begin{cases} 0 & t/\tau_b \leq 0 \\ (\frac{t}{\tau_b})^{N+1} \sum_{n=0}^{N} \binom{N+n}{n}\binom{2N+1}{N-n}(-\frac{t}{\tau_b})^n & 0 \leq t/\tau_b \leq 1 \\ 1 & t/c \geq 1 \end{cases} \tag{3.6}$$

where τ_b is the build-up time to a constant frequency. After this build-up however, the build-up signal needs to be connected to the top sensor sine matched function. The final function value of the build-up signal is denoted $y(\tau_b)$, position at build-up time. The function value of the sine-matched top position was set to match this value changing the phase shift of the top sine function. Once more, the significance of relative time, not absolute is noted. The phase shift of the driving force was found by

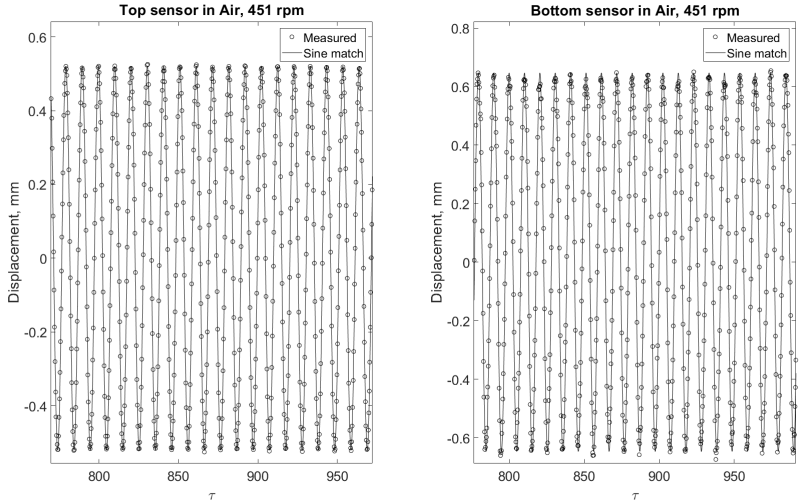

Figure 3.5: Sine matching movement of sensors

$$y(\tau_b) = s(1)\sin\left(\frac{2\pi\tau_b}{s(2)} + \frac{2\pi}{s(3)}\right) + s(4) \tag{3.7}$$

$$\sin^{-1}\left(\frac{y(\tau_b) - s(4)}{s(1)}\right) = \frac{2\pi\tau_b}{s(2)} + \frac{2\pi}{s(3)} \tag{3.8}$$

$$s(3) = \frac{2\pi}{\sin^{-1}\left(\frac{y(\tau_b)-s(4)}{s(1)}\right) - \frac{2\pi\tau_b}{s(2)}} \tag{3.9}$$

with the result being substituted into Eq. (3.3) for a common point between the two expressions. To clarify, this initial build-up is just an artificial function to avoid numerical instability. In order to analyze differences between both measurements, sine matched expressions and simulated movement, all curves were shifted equally. This was accomplished by calculating the time shift caused by the phase shift visualized in Fig. (3.6). With only the time shift between the two, the position is equal. Equalling two of the sinusoid expressions found in Eq. (3.3) yields

$$\begin{aligned} s(1)\sin\left(\frac{2\pi\tau_{old}}{s(2)} + \frac{2\pi}{s_{old}(3)}\right) + s(4) &= s(1)\sin\left(\frac{2\pi\tau_{new}}{s(2)} + \frac{2\pi}{s_{new}(3)}\right) + s(4) \\ \frac{2\pi\tau_{old}}{s(2)} + \frac{2\pi}{s_{old}(3)} &= \frac{2\pi\tau_{new}}{s(2)} + \frac{2\pi}{s_{new}(3)} \\ \Delta\tau &= s(2)\left(\frac{1}{s_{old}(3)} - \frac{1}{s_{new}(3)}\right) \end{aligned} \tag{3.10}$$

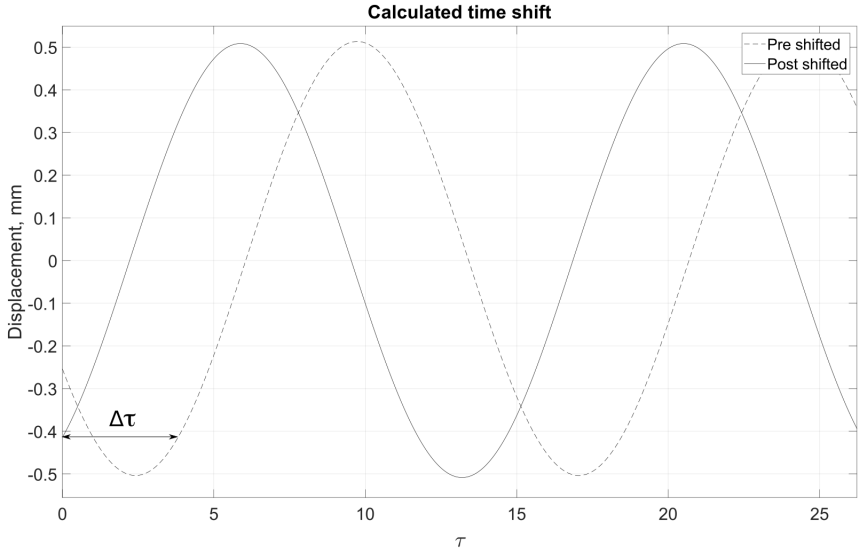

Figure 3.6: Time shift calculated to match simulations and matched data

The least square residual from the best fit calculated is presented for all results. Another argument to refrain from using a low-pass filter is that the described sine matching procedure provides similar results. It is not believed that a low-pass filter before sine matching would improve the accuracy of the match obtained. Hence, an additional data alteration that would not necessarily increase accuracy of representation is avoided.

3.5 Matlab Implementation

An illustrative figure with relationship between Matlab scripts and codes is presented in Fig. (3.7). The main script *runExperiments.m* seen in Appendix (B.1) was used to decide what experiments to consider. The date and experiment number of this experiment were initially input in Matlab. Parameters such as gravitational constants, Young's modulus and simulation duration were also defined. Information about the rig-up, including size and dimension of all piping and fluid properties were loaded from a .csv file using *experimentInfo.m* in Appendix (B.2). Data was loaded by the path created by the aforementioned parameters date and experiment number, and the Matlab function *measurements.m* in Appendix (B.3). Due to switch-on delay of 600 ms on both sensors, this period of measurements proved useless throughout experiments. Position was found to vary within this interval, while the time stamp of these measurements were all at a single point in time. As a solution, the starting point of the data set was set to the first points with separation in time. The importance of time was not the total duration of experiments, but rather the time between measurements. Hence, time can be shifted, as long as the same shift is made for both top and bottom measurements. This was carefully ensured

throughout all operations including time shift of data. The data was also offset to oscillate around a value of zero by subtracting the mean of all positional data. The frequency of the experiment was then found by averaging the time between every second zero-crossing. The next step of the Matlab procedure was to run through the high-pass filter *highpassFilter.m* described in Section (3.3.1) with code attached in Appendix (B.4). The first points of the data series was flattened out by the filter, and thus removed thereafter. As mentioned, the filter settings were optimized by a previous analysis, but the effects were still documented by function *filterAmplification.m* in Appendix (B.5). Next up was matching the positional data of both sensors to sinusoidal functions as described, by the function *SineMatch.m* in Appendix (B.6). The sine matched top function was connected to the created build-up driving force, and the sine matched signals shifted accordingly. The simulated predictions were calculated according to the model presented in Section (1.1.1) by function *experimentMovement.m* and a series of other smaller functions in Appendix (B.7) through (B.11). An additional flow chart of this function is found in Appendix (B.1). Finally two time delays were calculated by *findDelay.m* in Appendix (B.12). One being the delay between simulated and sine matched bottom movement, and the other between top and bottom measured movement. This was done by the difference in time between zero-crossings of the input data series with corresponding time. The time delay between simulations and matched data was also calculated analytically according to Eq. (3.10), and found to correspond with that of zero-crossings.

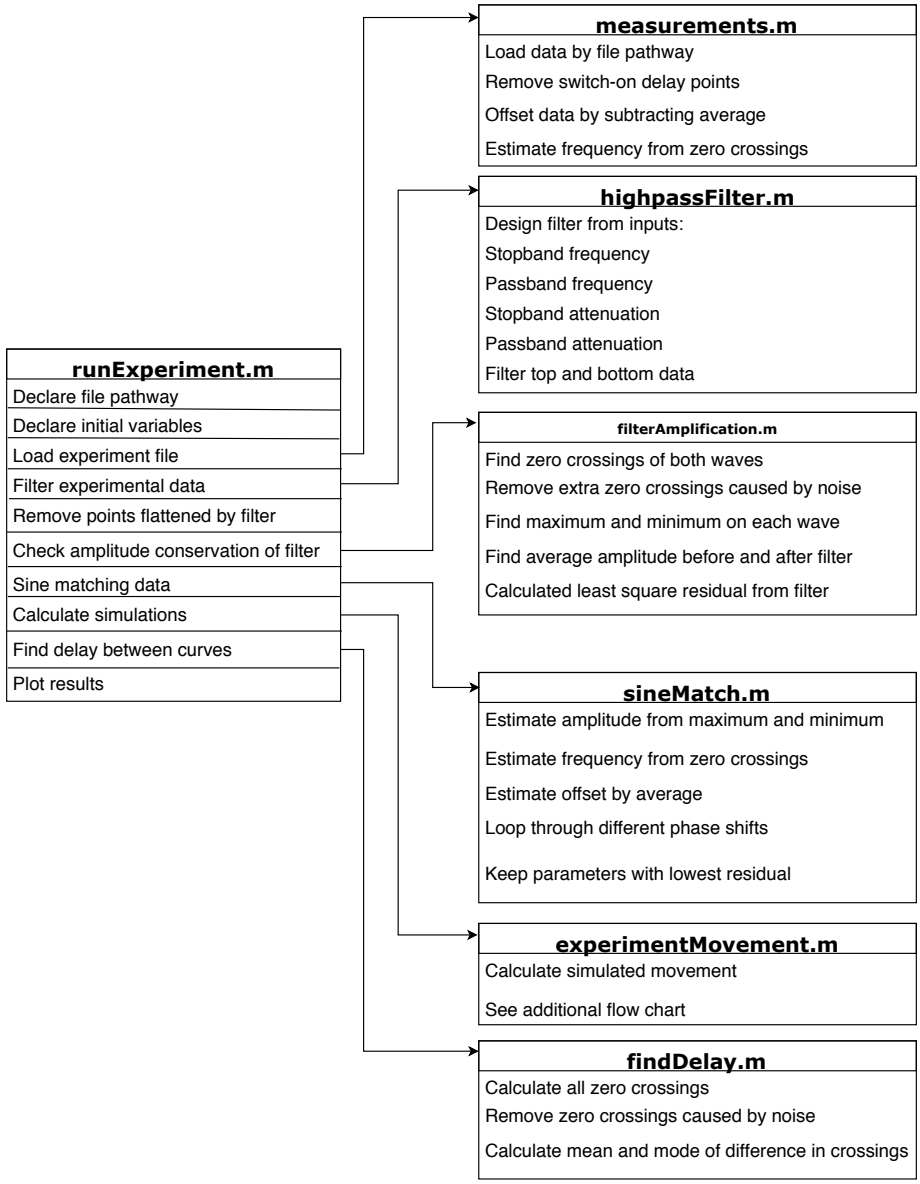

Figure 3.7: Flow chart showing relation between Matlab codes

Chapter 4

Results

A selection of results are presented throughout this chapter. For simplicity and the purpose of interpretation, all presented results were generated with an amplitude of 0.5 mm. This amplitude yielded useful results across the most frequencies, and is hence the best basis for interpretation of frequency dependency. All experiments were conducted at frequencies below that of the first resonant frequency, which was estimated to 1125 rpm (18.75 Hz) and 1090 rpm (18.15 Hz) for air and water respectively. As periodic and steady state trends are seen for all experiments, the time scale presented is limited to a few waves. The curves presented are simulated movement, and sine matched measurements of both top and bottom sensor. The time scale presented is on a dimensionless scale, with conversion to time in seconds found by division of 76.98. Experiment frequencies, measured in rpm, is converted to Hz by division of 60. Additional results showing full scale simulated and measured movement are found in Appendix (A).

4.1 Results of an Air-Filled Well

In Fig. (4.1) the results of a low frequency experiment is seen. All curves follow the same major trend, but some dissimilarities are worth mentioning. At low experiment frequencies, results show that the model overestimates amplification, while measurements show a bottom amplitude consistently lower than the top. This is an indication of damping of the movement along the drillstring. Considering the right part of the figure shows one wavelength of the steady state of the system. In this frequency interval there is a noticeable delay between simulations and sine matched data of the bottom sensor. Simulations predict no delay between top and bottom movement. This naturally implies that the time delay between top and bottom sine matches equals that of simulations and bottom sine match. It should be noted that sine matching of bottom sensor measurements result in larger discrepancies compared to those of high experiment frequency. The sine matched function and measured points of both top and bottom sensors is seen in Fig. (4.2). This figure shows compressed wave tops and bottoms of the bottom element, implying that the

movement is somehow halted. All shifts between simulated and measured movement is summarized in Table (4.1), along with predicted and measured amplitude and the least square residual of the sine fit.

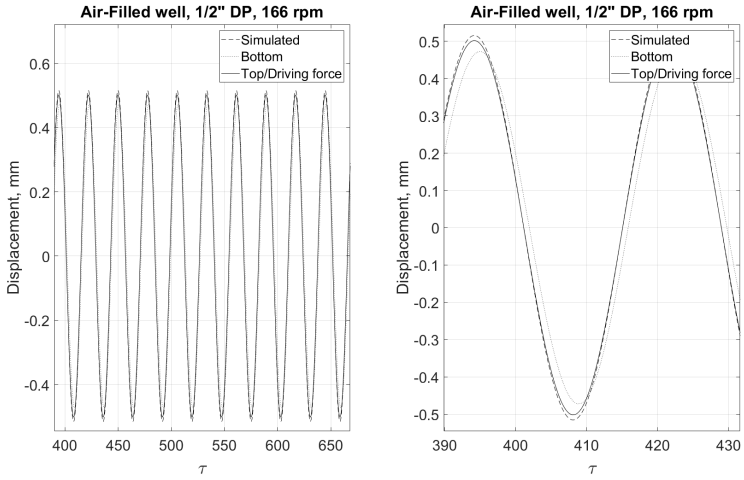

Figure 4.1: Results of 166 rpm experiment in air

The sine fit of the 166 rpm experiment is presented in Fig. (4.2). The figure shows an example of a measurement set of a low frequency experiment, with reduced amplitude in the bottom of the drillstring. The harmonic trend of the driving force is clearly visible from top sensor measurements.

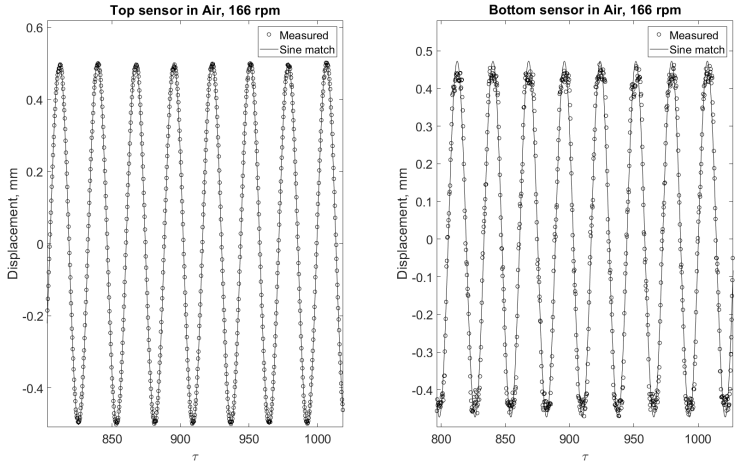

Figure 4.2: Sine matching both sensors at 166 rpm in air

Results of a 451 rpm experiment is seen in Fig. (4.3). The most noticeable difference compared to lower frequency experiments, is the additional amplification predicted by simulations. The measured amplification of the lower ends of the drillstring also show the first signs of surpassing a factor of one. In this range of experiment frequencies, little difference is found between simulated and measured amplification. It is also seen that time delay is considerably smaller than at 166 rpm, at approximately half the original value.

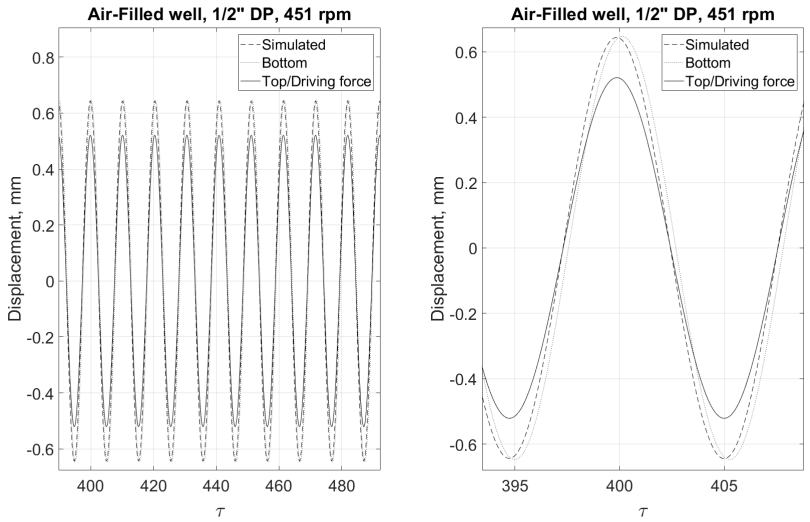

Figure 4.3: Results of 451 rpm experiment in air

The least square residual resulting from sine matching shown in Table (4.1), is approximately constant across all frequencies, except for a few noticeable exemptions. The most inaccurate fit is presented in Fig. (4.4). There seems to be a grouping of samples at the top of each wave. It is believed that this causes the increased least square difference, compared to the sine fits in Fig. (4.2). Nevertheless, by visual inspection the sine matched data still seem representative of the movement, seen in Fig. (4.5).

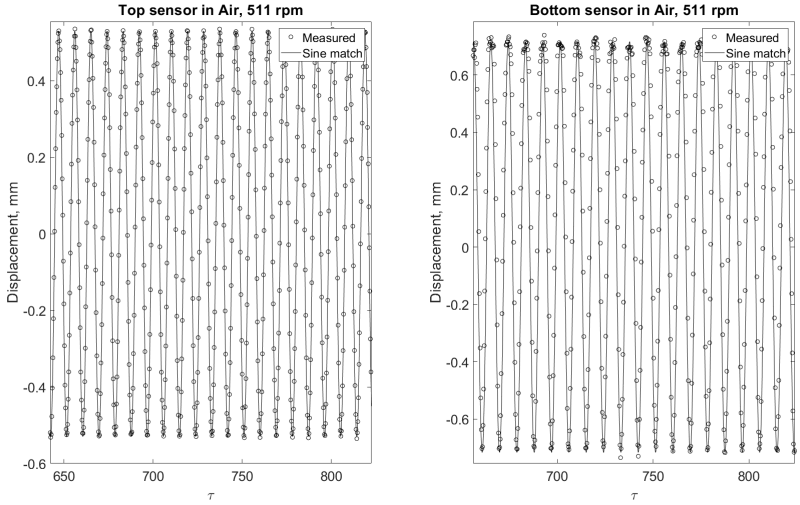

Figure 4.4: Sine matching both sensors at 511 rpm in air

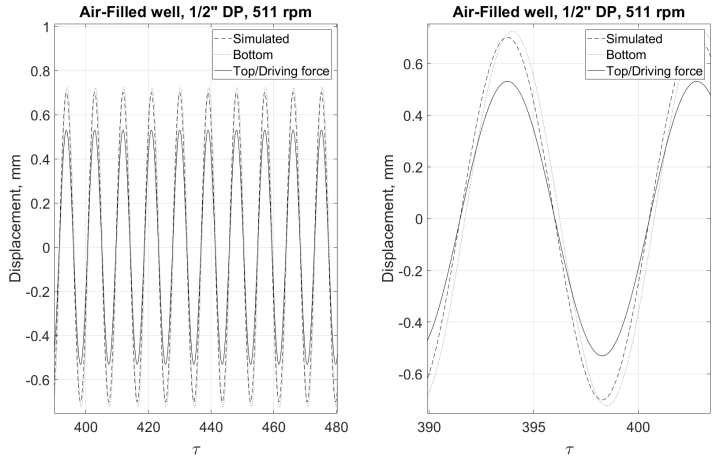

Figure 4.5: Results of 511 rpm experiment in air

At one of the higher experiment frequencies of 752 rpm, the amplification is still relatively accurately predicted by simulations. Predicted and measured amplitude are approximately equal, with the predicted being slightly higher. Time delay have decreased, to less than 3 ms.

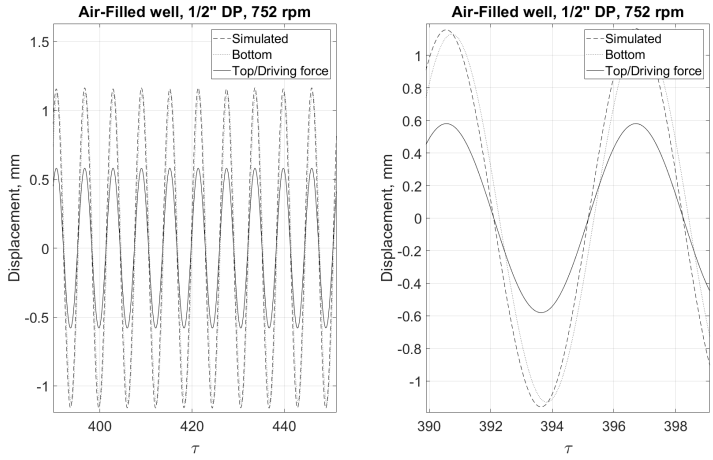

Figure 4.6: Results of 752 rpm experiment in air

4.1.1 Amplitude vs Frequency

Final results from an air filled well are shown in Fig. (4.7), where bottom amplitude is plotted along with predicted amplitude as a function of frequency. Predicted amplitude is strictly increasing, up to the first resonant frequency estimated at 1125 rpm. The measured top amplitude is also included as this is used to calculate simulations. The sum of relative errors between predicted and measured amplitudes was calculated to 143%. It is noticed that predictions seem to be a better fit for the higher frequencies. At frequencies between 360 and 705 rpm, the predicted amplitude and the actually measured amplitude are approximately equal, whereas larger deviations are seen for the lower frequencies. Within this interval, the relative error of all points was calculated to 30%.

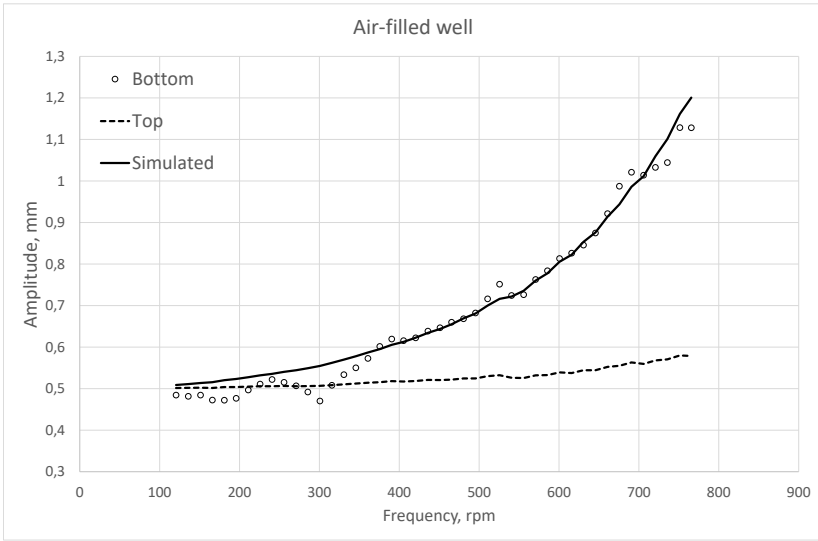

Figure 4.7: Amplitude as a function of frequency for an air-filled well

4.1.2 Delay vs Frequency

The delay between the dotted curves presented in the above plots is summarized in Fig. (4.8). That is, the delay between simulated predictions and sine matched measurements. As no delay was predicted by the model, this is the same delay that is found between top and bottom sine matched movement. The presented data bears resemblance of a step function. The time scale presented is in milliseconds, and the two steps of the data are approximately equal to 4 and 8 ms. As the sampling frequency of experiments was 250 Hz, this corresponds to one and two samples respectively. Indicating that for the lower

frequencies, movement at the bottom sensor occurs approximately two samples later than at the top. For higher frequencies, this is reduced to one sample difference.

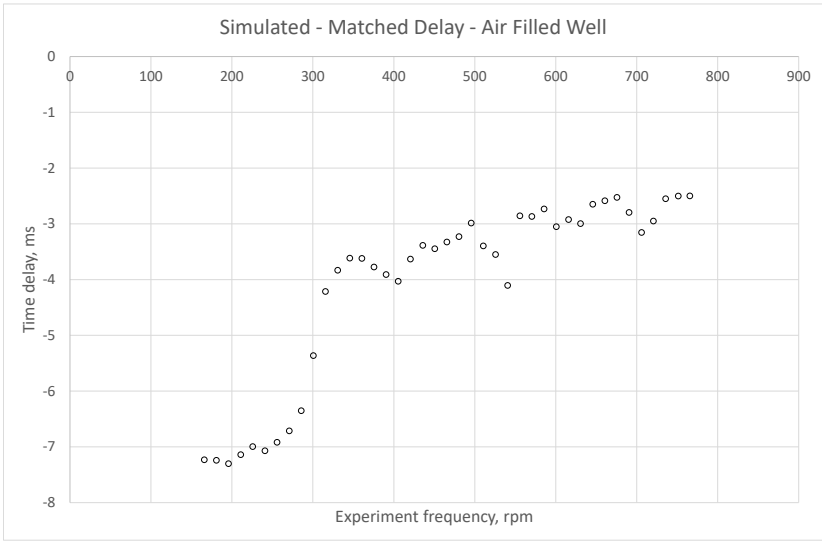

Figure 4.8: Delay between simulated data and sine matched measured data in air

The time delay between measured top and bottom movement is displayed in Fig. (4.9). This is the time delay that is actually measured in experiments. The delay between simulations and sine matched data could also be used as an indication of the accuracy of the sine matching and the smoothness of measurements. Ideally, the two Figs. (4.8) and (4.9) should be equal, and as Table (4.1) show, they approximately are for the higher frequencies. This is not the case for lower frequencies however. There are some uncertainty related to the lower experiment frequencies, caused by the measured data and the approach used to calculate the delay. Top sensor measurements have proved easily recognizable as a sinusoidal movement, while bottom measurements are influenced by factors not accounted for in the model. Comparing the two, gives an indication of the accuracy at which the bottom signal can be fitted to a sinusoidal motion, along with the least square residual from Table (4.1). It should be noted that the least square residual is calculated for an equal duration of time for each frequency. This implies that the residuals from more high-frequent experiments are calculated over more waves compared to the low-frequent experiments, and this feature is believed to explain the trend of slightly increasing residuals.

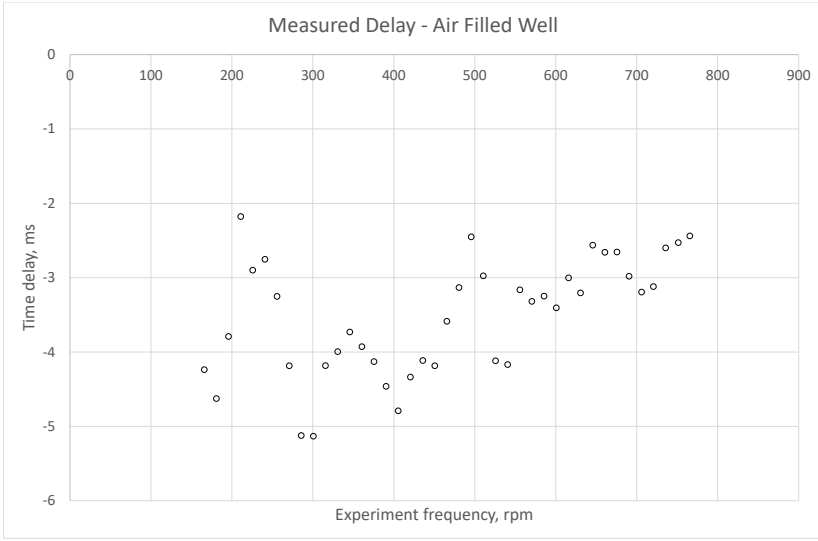

Figure 4.9: Delay between measured top and bottom data in air

Frequency [rpm]	Amplitude Bottom [mm]	Amplitude Top [mm]	Amplitude Simulated [mm]	Measured delay [ms]	Sine Match Delay [mm]	Sine Match Top Least Square	Sine Match Bottom Least Square
166	0.473	0.502	0.516	-4.2	-7.2	1.2	22.1
181	0.471	0.503	0.520	-4.8	-7.2	1.2	20.6
196	0.477	0.504	0.524	-3.6	-7.3	1.7	16.8
211	0.498	0.505	0.527	-2.3	-7.2	1.3	18.7
226	0.511	0.506	0.533	-3.0	-6.9	1.3	19.5
241	0.522	0.506	0.536	-2.4	-7.0	1.6	23.5
256	0.516	0.506	0.540	-3.1	-6.7	1.7	28.6
271	0.508	0.506	0.544	-3.8	-6.5	1.6	31.6
286	0.492	0.506	0.549	-4.9	-6.2	2.0	45.2
301	0.469	0.507	0.555	-4.8	-5.2	1.9	44.4
316	0.505	0.508	0.562	-4.1	-4.2	1.9	49.4
331	0.533	0.511	0.570	-3.8	-3.7	2.1	53.9
346	0.550	0.512	0.578	-3.7	-3.7	2.3	54.9
361	0.573	0.514	0.587	-3.8	-3.5	2.6	56.8
375	0.600	0.515	0.595	-4.1	-3.8	2.9	53.1
390	0.620	0.518	0.606	-4.5	-4.1	2.3	53.0
406	0.616	0.518	0.614	-4.3	-4.2	3.0	37.5
421	0.622	0.518	0.623	-4.4	-3.6	2.5	31.2
436	0.638	0.521	0.634	-4.1	-3.4	2.3	25.1
451	0.647	0.521	0.645	-3.9	-3.3	2.6	30.2
466	0.659	0.522	0.655	-3.8	-3.4	3.3	47.7
480	0.669	0.525	0.669	-3.4	-3.5	5.3	70.3
495	0.681	0.525	0.681	-2.6	-3.1	4.5	176.6
511	0.716	0.530	0.700	-3.5	-3.8	5.0	226.4
526	0.752	0.532	0.716	-4.3	-3.8	2.7	42.0
541	0.725	0.526	0.722	-3.8	-3.8	3.5	158.6
556	0.727	0.525	0.736	-4.0	-3.0	2.5	40.5
571	0.762	0.532	0.760	-2.8	-2.5	2.7	16.6
586	0.783	0.532	0.777	-3.4	-2.8	3.1	17.1
601	0.814	0.539	0.806	-3.8	-3.5	3.1	17.7
616	0.826	0.538	0.823	-3.2	-3.1	3.3	14.2
631	0.847	0.544	0.854	-2.7	-2.6	3.7	16.7
646	0.873	0.544	0.876	-2.7	-2.8	3.2	16.6
661	0.922	0.553	0.914	-3.0	-3.0	4.2	16.2
676	0.992	0.555	0.944	-2.7	-2.7	4.3	17.6
691	1.021	0.563	0.987	-3.1	-2.9	4.5	29.4
706	1.012	0.559	1.011	-3.1	-3.0	21.7	91.3
721	1.035	0.568	1.060	-3.0	-2.8	5.8	42.6
736	1.044	0.571	1.103	-2.6	-2.6	4.8	27.6
752	1.130	0.580	1.164	-2.4	-2.3	6.6	40.1
766	1.130	0.579	1.201	-2.4	-2.4	6.3	44.2

Table 4.1: Results of an air-filled well

4.2 Results of a Water-Filled Well

After filling the well with water, more experiments were performed with the 0.5 mm amplitude. Fig. (4.10) presents the response of the system at a motor frequency of 105 rpm. Simulations predict little to no amplification, while measurements yielded an amplitude lower than that of the driving force, similar to the behaviour seen with an air-filled well. The trend of these low frequent experiments in water are very similar to those in air. Inspection of one wave shows a delay between top and bottom measurements that is not predicted by simulations.

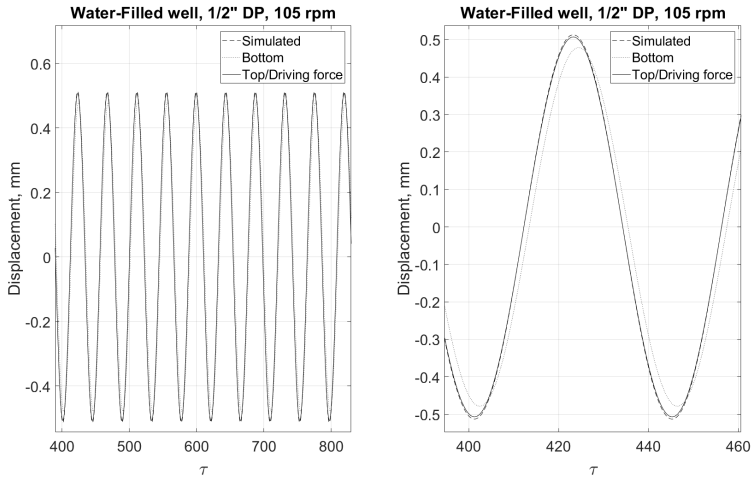

Figure 4.10: Results of 105 rpm experiment in water

At higher experiment frequencies, there are once again a better fit between simulations and measurements. Fig. (4.11) shows a clear amplification predicted at 466 rpm, and a measured amplification that is approximately equal. Also seen is a decreased time delay between simulated and matched movement. This delay is more than halved compared to the delay from the 105 rpm experiment.

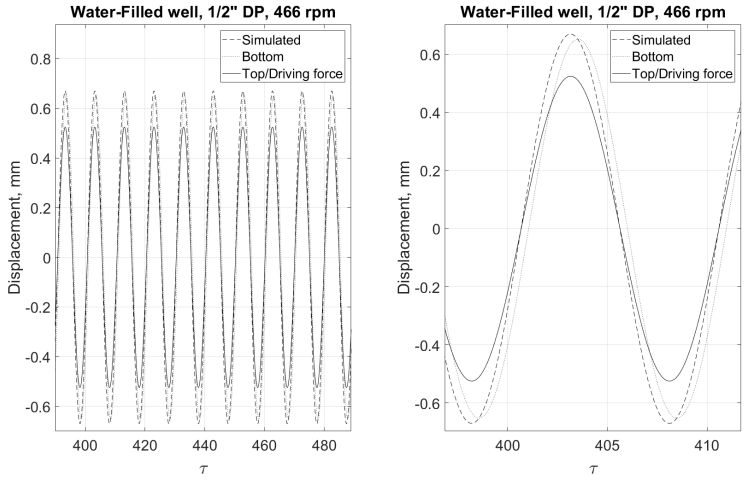

Figure 4.11: Results of 466 rpm experiment in water

One of the higher frequency experiments is presented in Fig. (4.12). This figure shows that predicted amplification exceeds the measured data. Both measured and predicted amplitude are more than double that of the driving force amplitude. Time delay is evident only on a very small time scale.

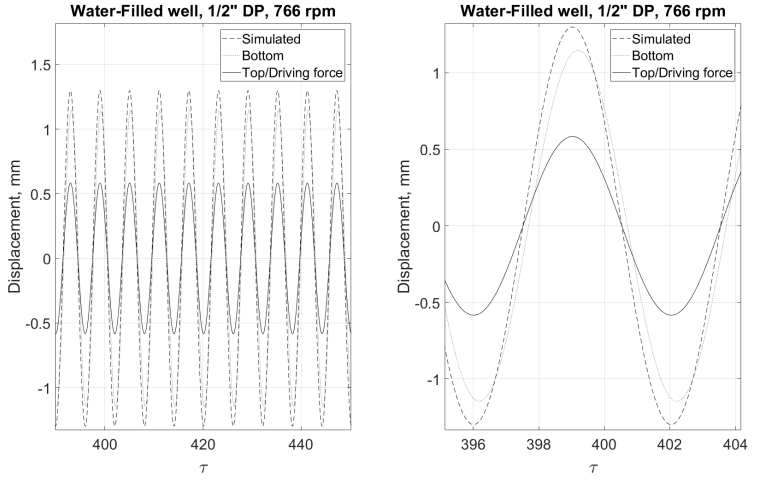

Figure 4.12: Results of 766 rpm experiment in water

4.2.1 Amplitude vs Frequency

Final results of amplification in experiments with a water-filled well are shown in Fig. (4.13). Based on this figure there are three distinct frequency intervals that stand out. In the interval below 350 rpm, the model consistently underestimates the amplitude of the bottom element. Measurements within this interval show a similar trend to that seen in experiments of air is seen. The measured amplitude at the bottom of the drillstring is even less than that of the driving force. In experiments with frequencies between 350 and 700 rpm the movement is relatively accurately predicted by the model. Similar amplification trend is seen for both measurements and simulations. These frequencies also saw the most smooth output data from measurements, with the least amount of noise in both measurements and sound from the well. Above 700 rpm, a sudden shift to lower amplitudes is seen in the experimental data. Predictions show a strictly increasing trend up to the first resonant frequency estimated at 1090 rpm, and not a drop at 700 rpm. The sum of all relative errors for experiments in water was calculated to 256%. Considering only the middle range of experiment frequencies, from 360 to 690 rpm resulted in a relative error of 62 %.

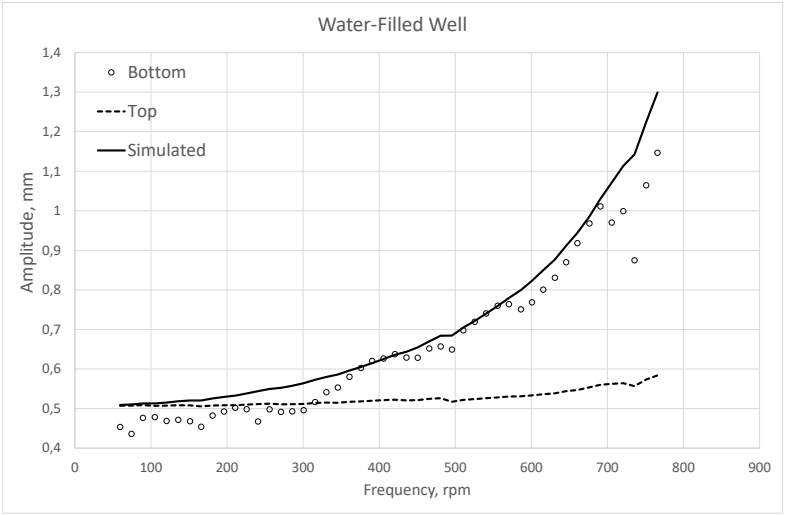

Figure 4.13: Amplitude as a function of frequency for a water-filled well

4.2.2 Delay vs Frequency

The delay between simulation predictions and matched measured data is seen in Fig. (4.14). Initial experiments show an almost linearly decreasing time delay up to approximately 300 rpm experiment frequency. After 300rpm experiment frequency this trend flattens out, and the continuing trend is approximately constant at 4ms.

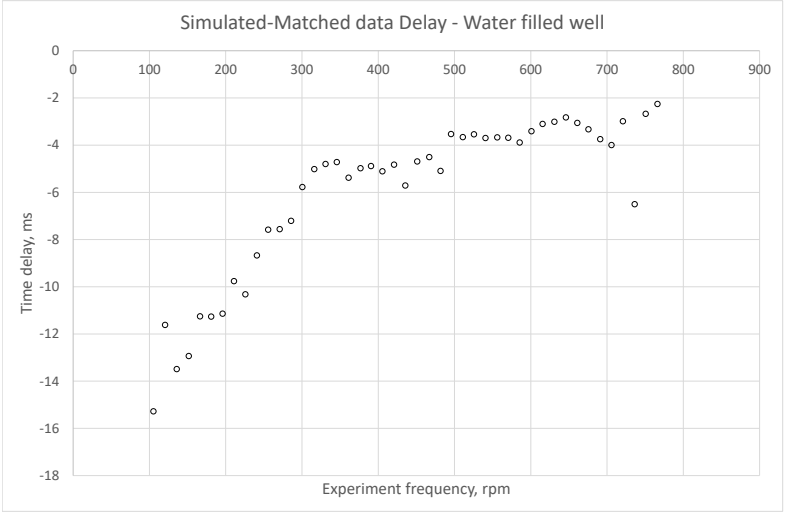

Figure 4.14: Delay between simulated data and sine matched measured data in water

Delay between measurements of both top and bottom sensor is seen in Fig. (4.15). The measured time delay seems more similar to the delay between simulations and bottom movement than was the case for experiments in air. The same initial linearly decreasing trend is also evident in the measured delay, although more indistinguishable, and a little steeper. Consequently, the onset of a flat trend is seen earlier, at about 250 rpm. The values after flattening out is very similar to the simulated delay.

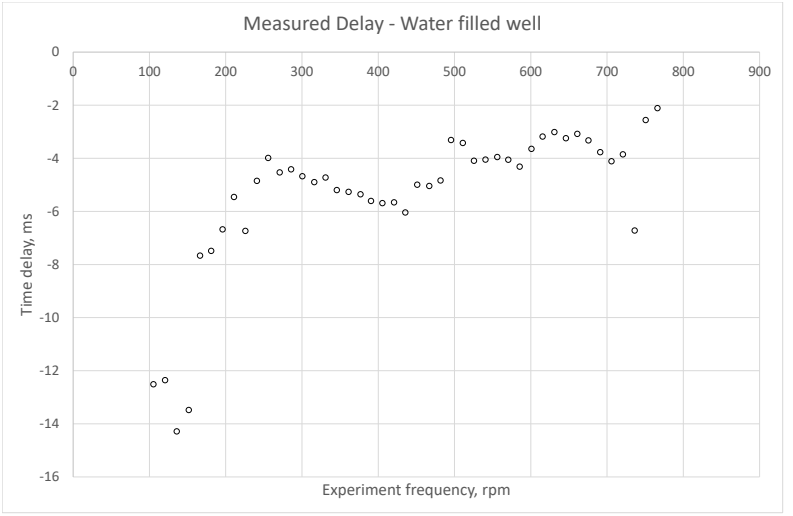

Figure 4.15: Delay between measured top and bottom data in water

Frequency [rpm]	Amplitude Bottom [mm]	Amplitude Top [mm]	Amplitude Simulated [mm]	Measured Delay [ms]	Sine Match Delay [ms]	Sine Match Top Least Square	Sine Match Bottom Least Square
105	0.479	0.507	0.513	-12.5	-15.3	0.8	11.0
120	0.468	0.507	0.515	-12.4	-11.6	0.9	11.4
136	0.472	0.509	0.519	-14.3	-13.5	0.8	12.5
152	0.467	0.508	0.521	-13.5	-12.9	1.0	12.8
166	0.455	0.507	0.522	-7.7	-11.3	1.2	16.6
181	0.479	0.508	0.526	-7.5	-11.3	0.9	14.2
196	0.489	0.508	0.529	-6.7	-11.1	0.8	13.5
211	0.502	0.509	0.533	-5.5	-9.8	0.9	13.0
226	0.497	0.509	0.538	-6.7	-10.3	0.9	14.1
241	0.465	0.512	0.544	-4.8	-8.7	1.1	19.0
256	0.497	0.513	0.550	-4.0	-7.6	1.4	21.1
271	0.489	0.511	0.553	-4.5	-7.6	1.7	25.3
286	0.490	0.511	0.558	-4.4	-7.2	1.4	35.0
301	0.494	0.512	0.564	-4.7	-5.8	1.6	44.4
316	0.518	0.514	0.573	-4.9	-5.0	2.0	48.2
331	0.542	0.515	0.580	-4.7	-4.8	1.7	44.5
346	0.551	0.516	0.588	-5.2	-4.7	1.7	43.2
361	0.581	0.517	0.596	-5.3	-5.4	2.0	47.7
377	0.602	0.518	0.606	-5.4	-5.0	2.1	51.5
390	0.620	0.520	0.615	-5.6	-4.9	2.2	37.8
406	0.627	0.521	0.624	-5.7	-5.1	2.0	29.1
421	0.636	0.522	0.636	-5.7	-4.8	1.8	19.7
436	0.629	0.520	0.643	-6.0	-5.7	1.9	17.8
451	0.629	0.522	0.656	-5.0	-4.7	1.9	19.6
467	0.654	0.525	0.672	-5.0	-4.5	2.1	19.3
482	0.656	0.526	0.685	-4.8	-5.1	3.7	44.0
495	0.647	0.517	0.685	-3.3	-3.5	5.0	205.6
511	0.695	0.522	0.705	-3.4	-3.7	4.6	181.8
525	0.720	0.524	0.722	-4.1	-3.5	2.9	84.8
541	0.740	0.526	0.740	-4.0	-3.7	2.7	51.6
556	0.761	0.529	0.760	-4.0	-3.7	2.8	18.6
571	0.765	0.532	0.782	-4.1	-3.7	2.9	27.5
585	0.752	0.531	0.800	-4.3	-3.9	3.0	22.3
601	0.769	0.534	0.824	-3.6	-3.4	2.8	14.4
616	0.799	0.536	0.849	-3.2	-3.1	3.2	12.1
631	0.832	0.539	0.879	-3.0	-3.0	2.8	13.2
646	0.870	0.544	0.912	-3.2	-2.8	3.3	18.9
661	0.917	0.546	0.944	-3.1	-3.1	4.1	15.0
676	0.968	0.554	0.986	-3.3	-3.3	1.6	16.3
691	1.010	0.560	1.031	-3.8	-3.7	3.9	25.2
706	0.971	0.563	1.072	-4.1	-4.0	4.7	19.3
721	0.999	0.564	1.113	-3.9	-3.0	3.6	25.2
736	0.875	0.557	1.143	-6.7	-6.5	5.0	72.3
751	1.063	0.573	1.223	-2.6	-2.7	5.4	36.5
766	1.145	0.584	1.300	-2.1	-2.3	5.5	36.8

Table 4.2: Final results of a water filled well

4.3 Sensitivity Analysis

Some additional uncertainty is related to the fluid description of the model. A sensitivity analysis was performed to investigate the effects of variations in the fluid model. Parameters were changed with the ambition to match the measured data. Experiments with frequencies below 250 rpm were disregarded due to the erratic data associated. No delay was predicted by simulations in either well fluid. The included Basset forces would cause a delay in simulated delay if sufficiently large. The b-factor from in Eq. (1.19) was multiplied with various factors to find the best fit of the measured data in water experiments. The fit achieved by alteration of the b-factor can be seen in Fig. (4.16).

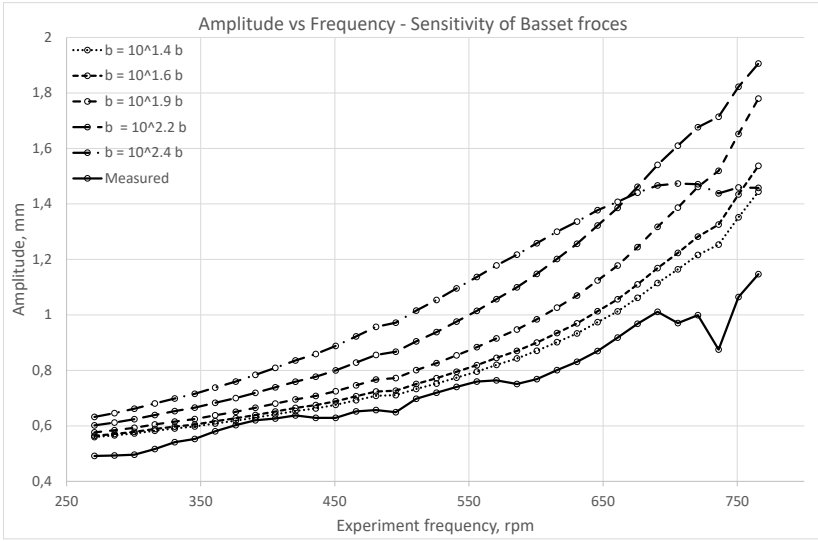

Figure 4.16: Delay between measured top and bottom data with various b-factors

Increasing magnitude of Basset force components suggest a decreasing relationship between frequency and time delay. This is in some part supported by experimental results in the bottom curve, although to a lesser degree. It is also seen that the b-factor must be increased greatly for significant changes in delay. Little change is seen for factors below 10, where the first significant separation from the curve of a b-factor calculated by physical properties. at which the curves separate from that of physically estimated parameters. At higher values of b-factor, the change is accelerated, and larger differences can be seen for smaller changes changes. The best fit was found for a factor of $10^{1.9}$.

Modification of this b-factor was also found to influence amplitude predicted by the model. The amplitude was counter-intuitively found to increase with larger b-factors. The time match obtained by modification of b-factor and the corresponding amplitude of a 600 rpm experiment is shown in Figs. (4.17) and (4.18).

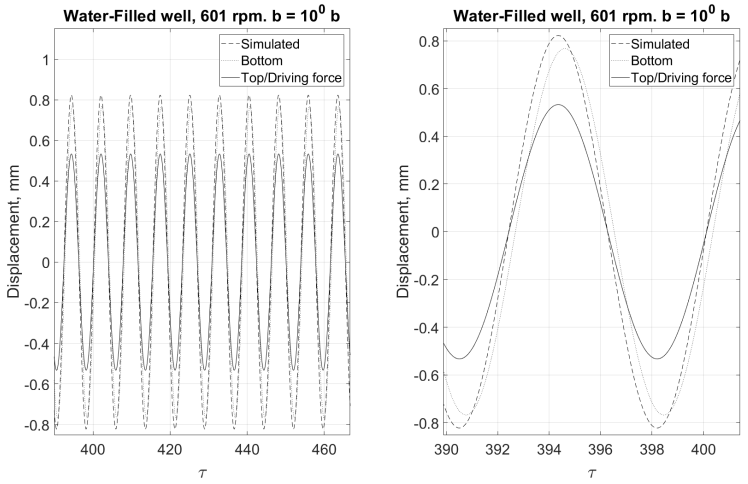

Figure 4.17: Results of 600 rpm experiment with b-factor based on physical parameters

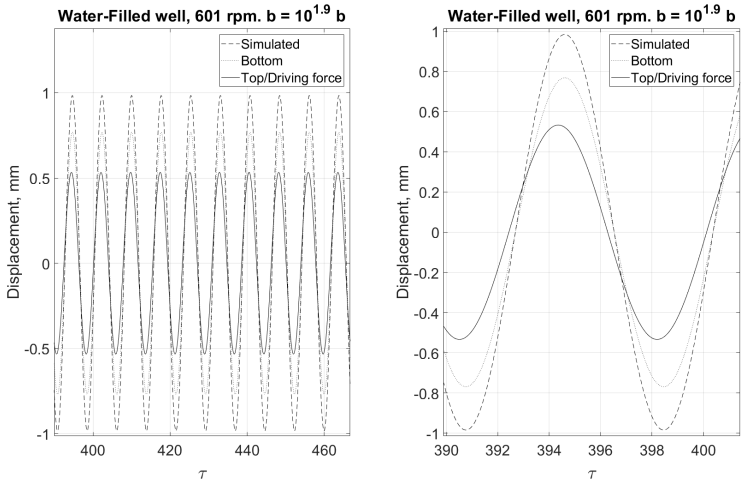

Figure 4.18: Results of 600 rpm experiment with b-factor fitted to match time delay

The corresponding amplitudes by alteration of the b-factor is shown in Fig. (4.19). The increasing amplitudes are seen for throughout increasing b-factors, with the largest b-factor as the exception. For this factor, the amplitude is found to decrease at higher frequencies. As is evident from the figure, the best amplification fit is that with no increase in Basset forces.

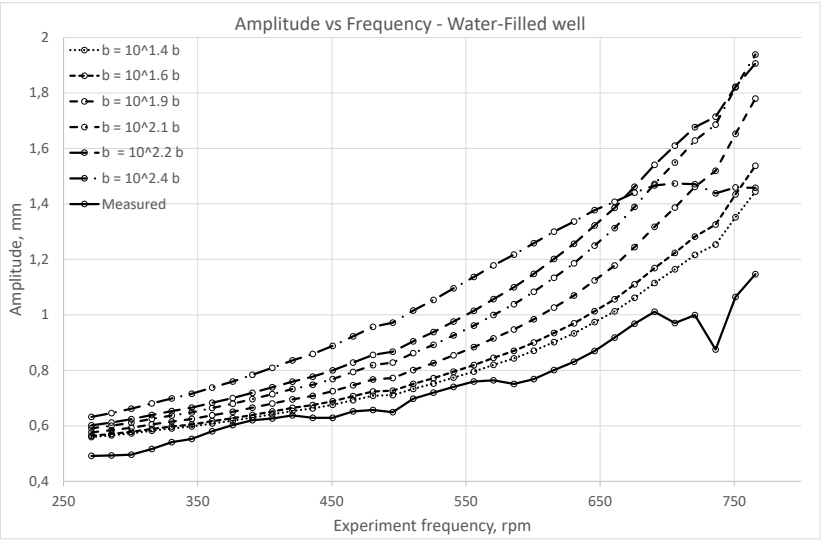

Figure 4.19: Predicted amplitude of bottom element with various b-factors

It was also tried to match the simulated amplification to that of experiments by changing another component of Eq. (1.18) responsible for damping. That is the c-factor from Eq. (1.19). This coefficient accounts for the viscous forces of the system. Sensitivity analysis with changing c-factors is seen in Fig. (4.20), Presented is the amplitude at different frequencies with increasing c-factors.

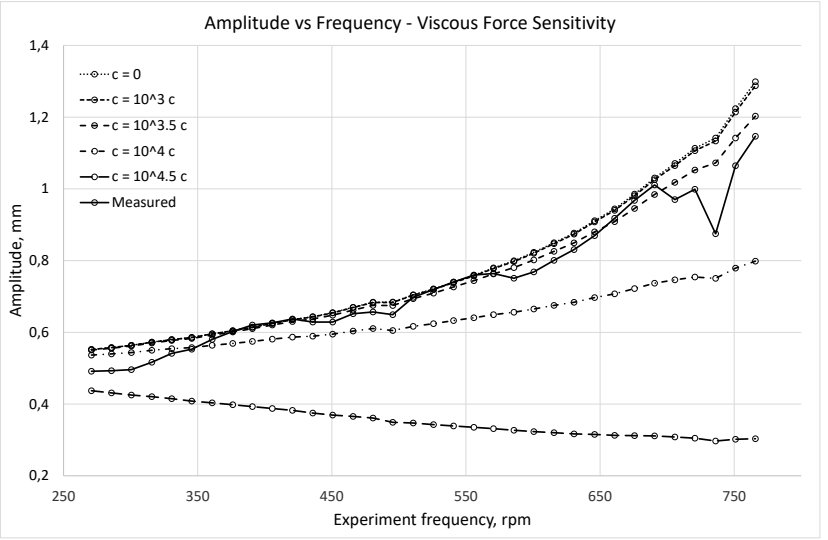

Figure 4.20: Predicted amplitude of bottom element with various c-factors

As is evident from the figure, there is little change from a small increase in c-factor. With large changes however, the motion is damped to a decreasing relationship with frequency. The best fit to the experimental data is found by increasing c-coefficient with a factor of $10^{3.5}$. Similar behavior is seen regarding time delay. Modification of the c-factor also causes a time delay in the simulated movement. The predicted delay by increasing c-factors is displayed in Fig. (4.21). It is visible that the delay between simulations and measurements almost vanishes by increasing the c-factor with $10^{3.5}$, similar to the amplification response.

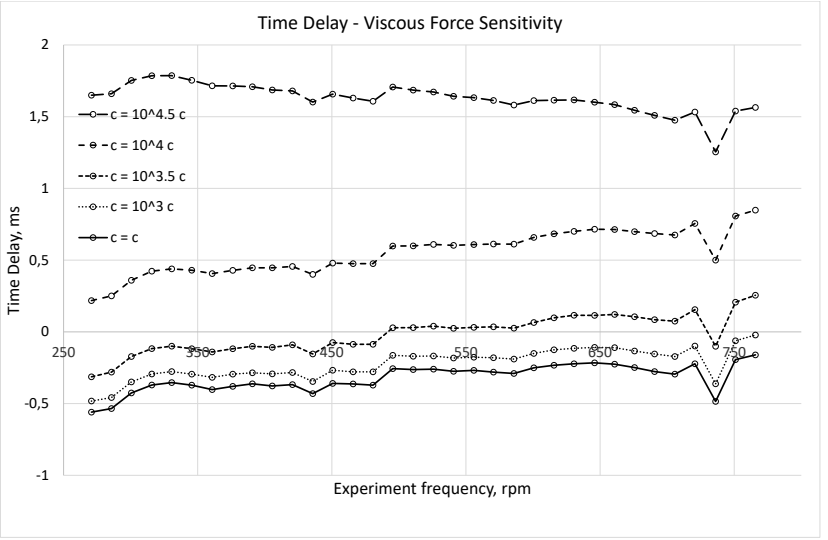

Figure 4.21: Predicted time delay of bottom element with various c-factors

Chapter 5

Discussion

In the following chapter, results will be discussed with regards to amplification and time delay separately. Due to the small differences seen in results with variation of well fluid, it is expedient to merge discussion of results irrespective of fluid. A special consideration is also given to the fluid model, which is discussed in detail based on the findings of experiments in water, and the modification of parameters to match simulated predictions and measurements.

5.1 Amplification

5.1.1 Low Experiment Frequency

Final results of both air-filled and water-filled well plotted in Figs. (4.7) and (4.13) show larger discrepancies at lower frequencies. These discrepancies can be traced back to the output data from the sensors. Comparison of Figs. (5.1) and (5.2) exemplifies the difference. At a low experiment frequency, the data points of the bottom sensor at wave tops and bottoms seem compressed rather than the expected smooth sinusoidal trend. This trend is seen throughout experiments in both air and water with frequencies below approximately 350 rpm. It causes a larger mismatch between the actual measured data and the sine matched data, even though more samples are taken at each wave.

As the same trend is observed in numerous experiments across several frequencies, it is reasonable to assume that it is not caused by wrongful measurements, but rather a physical obstruction of the wave tops and bottoms of the movement. The most appealing explanatory suggestion is that of friction and stick-slip phenomenon. As the same behaviour is seen on both top and bottom of each wave, it is also likely to have the same cause. The driving force does not impose a truly unidirectional movement, so some lateral movement is a natural consequence. According to Zhao et al. (2015), any contact between the drillstring and the borehole wall causes contact friction to dominate the damping of the drillstring motion. The vertical component will however, follow a sinusoidal function.

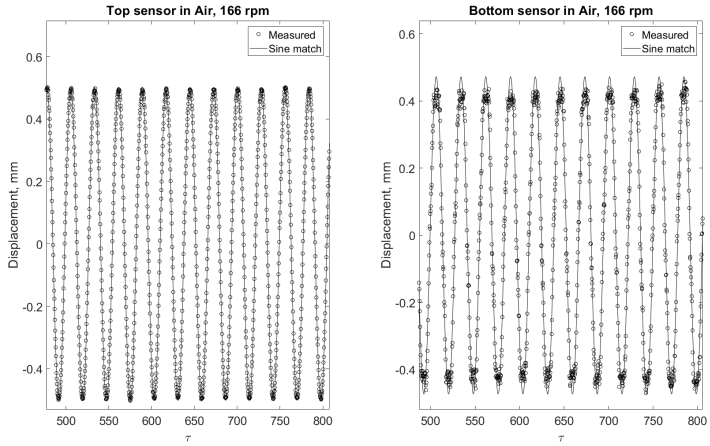

Figure 5.1: Sine matching both sensors at low experiment frequency

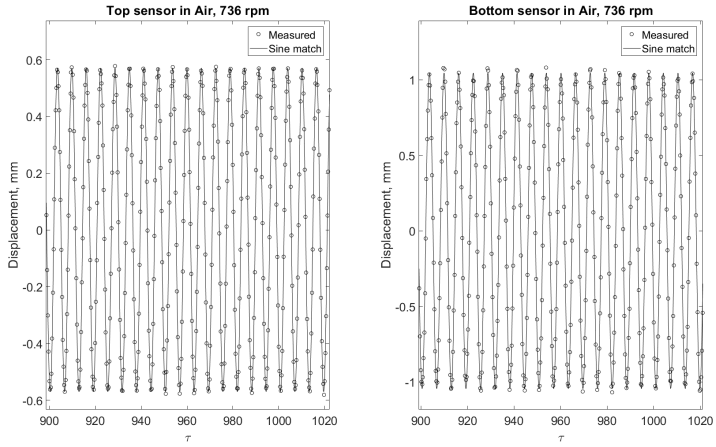

Figure 5.2: Sine matching both sensors at high experiment frequency

Thus, the velocity of the pipe will decrease significantly towards maximum and minimum displacement. The reduction in velocity results in insufficient kinetic energy to overcome friction along the drillstring, suppressing the amplitude to a lower value. Friction is then accumulated over the entire length of the drillstring, such that movement is actually subdued rather than amplified further down. As the most fundamental assumption of the model is that of uni-axial movement and no contact friction, the model falls short of accurate predictions when the friction induced becomes more dominant, as is believed to be the case for frequencies below 350 rpm. As similar amplitudes are found in both experiments of air and water, there are no distinct signs of water lubrication decreasing friction.

5.1.2 Middle Range Experiment Frequency

Within a range of experiment frequencies from roughly 350 to 700 rpm, the measured and predicted amplitude coincide better. Nevertheless, the increased least square difference of sine matching needs addressing. The phenomenon is partially explained by the number of waves to be fitted, as the residual is calculated for an equal number of samples. Additional deviations at frequencies of approximately 500 rpm, such as Fig. (4.5), are attributed to compressed measured points at each wave top. This implies that the drillstring spends more time at each wave top, than at the bottoms. Additionally it is noted that for all three experiments at which this is seen, the amplitude is more or less equal. This indicates that there might be a physical obstruction inhibiting the movement at this frequency or amplification. By inspection of similar frequencies in a water filled well, the same situation is recognized, with slightly lowered amplitudes. The difference in amplitudes is however equal to the buoyancy effect of changing fluid from water to air. Thus it is likely that the absolute position of the obstruction is the same for both experiment types, but that buoyancy causes the amplitude reduction. The source of the obstruction is unknown. One possibility is that of unfavorable connections location. Nevertheless, sine matches in this range are considered representative of the movement, illustrated in Fig. (4.4).

Another possible explanation, though perhaps more far-fetched, is found by studying literature on compressive behaviour of steel tubes. It is a well-known trait that steel is an isotropic material, as it has the same material properties independently of the direction. However, a tube under the influence of a force not perfectly perpendicular to the circular cross-section area will buckle rather than compress at a certain point. As previously mentioned, the driving force cannot be considered perfectly unidirectional. If the force exerted from the pipe oscillating at frequencies around 500 rpm is close to the threshold value of buckling, it is reasonable that top movement is somewhat constant up until this threshold is breached and additional upwards movement caused by buckling is seen. A paper by Alhussainy et al. (2017) inspected the behaviour of steel tubes of different length-diameter ratios (L/D) under compression. The authors found compressive strength to reduce as a function of increasing L/D ratio, along with strain. At increasing L/D ratio, buckling is initiated, rather than compression of the material. As the experiments presented have very low L/D ratios, it is a reasonable deduction that the onset of buckling would be seen at an early stage with the eccentric driving force. It is also noted that pipes with such high L/D ratios as more prone to lateral vibrations by small obstructions than stiffer pipes. Due to the small diameters chosen, the material was not stiff enough to exclude movement in other directions, besides the axial direction, which partially explains the friction seen at lower frequencies.

5.1.3 High Experiment Frequency

At higher experiment frequency there is a deviation between experiments in an air-filled and a water-filled well. Predictions better match results with an air-filled well. In results of a water-filled well, a sudden drop in measured amplification is seen at frequencies above 700 rpm. At similar frequencies the sound originating from the well increased signifi-

cantly. One possible explanation is that collision between casing and the drillstring causes increased vibrations in the string that inhibits the movement. Another is that the increased frequency simply enforces significantly higher viscous forces and larger effects of added mass. It is likely however, that the drop in amplification and the noises are related, rather than a physical phenomenon causing a reduced amplitude at higher frequencies. If fluid forces were the source of reduction, a steady transition would be expected, instead of the abrupt drop. One possible explanation is that of the onset of a resonant frequency in the lateral direction at this frequency. It is however challenging to conclude on the downhole behaviour with only sound and recorded position to go by. This brings up the very fundamental uncertainty in any drilling process; the inability to visually see what happens.

Comparison of simulated amplification suggest slightly higher amplification in water compared to air. This is believed to be caused by the lowered resonance spectrum caused by the increased frictional forces. This is an extension of the lower estimated resonant frequency in water. It is also to a certain degree supported by empirical data. Higher amplitudes are not consistently seen throughout experiment frequencies, but slightly higher values suggest an inherent trend. Top measurement amplitudes are also found to increase ever so slightly with increasing frequency. As a consistent enlargement of amplitude is seen with increasing frequency in all experiments, it is believed to be caused by the elasticity of the material. Even though the distance from motor to sensor is very short, some elastic behaviour is still experienced with high frequencies.

5.2 Delay

5.2.1 Low Experiment Frequency

The uncertainties in low frequency experiments are seen in the amplification estimation, but are also manifested with regards to time delay. The effects of what is believed to be stick-slip and friction, causes a spiky behaviour within individual waves as seen in Fig. (5.3). The measured motion is not strictly decreasing or strictly increasing in between maximum values. In several instances, this causes multiple zero-crossings within one wave. As a consequence, the determination of the true delay between curves have more uncertainty associated. For the sake of this thesis, the fist zero-crossing of each wave was utilized. A possible improvement could be achieved by filtering the data set through a low-pass filter. It was rather decided that the same effect is achieved by sine matching the data, which does not alter the input, but rather find a best fit representative of the data. This implies large uncertainties in the measured delay between top and bottom in experiments of low frequencies, and suggests that sine matched delays such as Figs. (4.8) and (4.14) are more trustworthy for the scope of the model. The sum of uncertainty with regards to both amplification and delay suggests more valuation placed in results of experiments at higher frequencies.

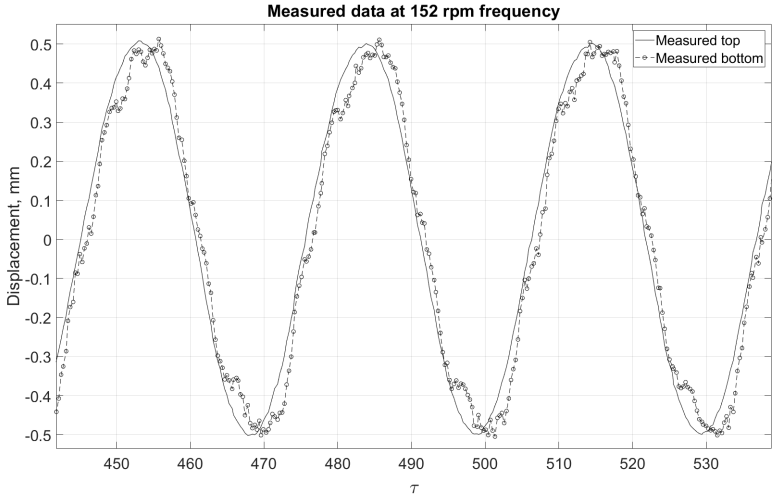

Figure 5.3: Difference in measured data at 152 rpm

5.2.2 Middle and Higher Range Experiment Frequency

With frequencies above 350 rpm, there was a clear distinction in zero-crossings. The issues related to higher least square residuals in the sine matched data was attributed to grouping of measurements at wave tops. The remainder of the waves had a clear sinusoidal trend, making zero-crossings clearly distinguishable and easily comparable. This is also manifested in more or less constant values of time delay irrespective of well fluid, as expected by simulations. It is also seen by measured and sine matched time delay of Figs. (4.15) and (4.14) almost equal above this frequency.

It is worth noticing that the decreasing delay exhibits a linearly decreasing trend in the low frequent experiments of a water filled well, whereas those in air bears more resemblance to a step function. This might be an indication of friction linearly decreasing due to the lubricating effects of water, while less lubrication is seen in air. These steps also coincides with values of one and two time samples respectively. The presence of a delay in the measured data is unquestionable, as it is seen throughout experiments. The correctness of the delay is more doubtful, though. The measured delay is heavily influenced by all exterior factors, such as lateral motion and friction. This could cause a motion to be delayed more than it would be in the case of a truly unidirectional movement, and recorded one or two samples later at the sensors. As average values of delay are utilized, the delay in the measured data is between zero and two samples for the majority of the data. Sine matched delay should yield the true delay irrespective of sampling rate, as the rate is sufficient to perfectly reconstruct all experiment movement according to the Nyquist-Shannon theorem. However, that delay is very small, and the signal that is sought to reconstruct is not necessarily perfectly harmonic due to the influence of other factors. This suggests that the exactness of both measured and sine matched delay is questionable, which could essentially be traced

back to influences of experiment uncertainty.

5.3 Basset Forces

One component of the final matrix equation, Eq. (1.18), that predicts time delay is Basset forces. Basset forces considers the historical acceleration of a body up until present time. This is due to accelerations effects on boundary layers. Viscous forces between a submerged body and a fluid, occur at the interface of the two, in the boundary layers. The forming of such a boundary layer is effected by the previous acceleration of the body, and is potentially large depending on the magnitude of this acceleration, according to Schwarzkopf et al. (2011). For calculations with low-viscous fluids such as air and water, no delay is predicted by the model over the distance of these experiments. Due to the low values of Basset forces in water, a considerable amplification of the b-factor is needed to match time delay to measurements. Manipulating the b-factor of the Basset forces caused a significantly steeper relationship between frequency and time delay that is not seen in the experimental data. It is also noted that the increase of Basset forces altered the predicted amplitude significantly. It is believed that this can be attributed to a shift in the amplification spectrum of the system. That is, the first resonant frequency is shifted significantly, so that larger amplitudes are predicted at lower frequencies. Even though dampening increases with increasing b-factor, the shift in frequency spectrum causes the amplitude to increase even more. Changing the b-factor for a slightly better fit with regards to delay, sets the amplification off to a much larger degree. This is exemplified by Figs. (4.17) and (4.18). In the derivation of Basset forces in Hovda (2017), an assumption of considering the drillstring as an infinite plate is made. Results indicate that the appropriateness of this assumption should be reviewed.

A literature review of sources such as Loewenberg (1993), Van Hinsberg et al. (2011) and Narayanan et al. (2003) indicate that Basset forces are most commonly accounted for in particle settling in fluids, where the boundary layer is large compared to the mass of the submerged object. According to Sarpkaya (2010), equations solving the motion of sinusoidal oscillations in fluids otherwise at rest is only available for amplitudes of about one tenth of diameter size. It is also stated that the effects of an abruptly imposed acceleration is heavily influenced by viscous effects immediately.

5.4 Viscous Forces

It was decided to inspect the relationship between amplitude and increasing viscous forces. The damped amplitude of experiments in a water-filled well were investigated by modification of the c-coefficient seen in Eq. (1.19). Similar to the large alteration needed for Basset forces, the viscous forces were also in need of significant enlargement. This is partly due to the low viscosity of water and the short drillstring. There is a linear relationship between viscous forces and both viscosity and drillstring length. Changing c-factor is seen to change delay irrespective of frequency, which is to a larger degree supported by measured results. Additionally, the resulting amplitude is reduced, which also corresponds

with experimental results. Because of the decreasing relationship between time delay and frequency, an exact match across all frequencies is unobtainable. The best fit between simulations and measurements is in fact found by neglecting Basset forces and increasing the c-coefficient with a factor of $10^{3.5}$. Results with this coefficient is seen in Figs. (5.4) through (5.6), showing one experiment in each frequency range.

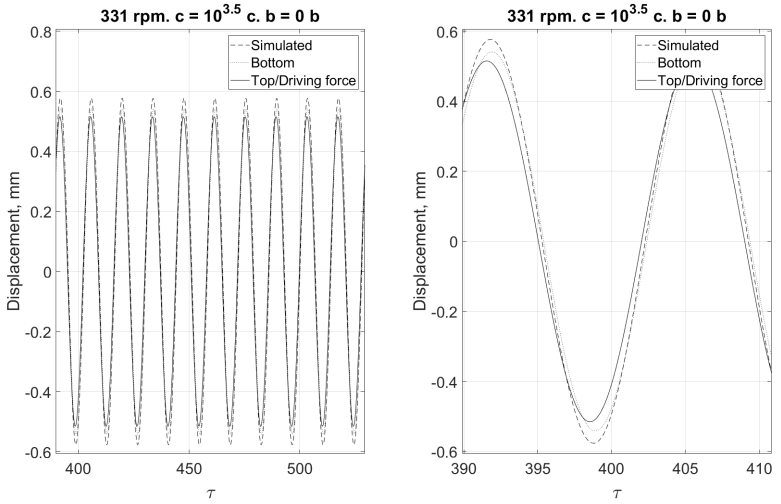

Figure 5.4: Results of 331 rpm experiment with best match of added mass and Basset force coefficients

5.5 Added Mass

Added mass accounts for the energy of an accelerating body of fluid. It is described by the mass displaced, but the effect is rather connected to inertia and energy. Unlike mass, but like inertia and energy, added mass effects can be both positive and negative according to Sarpkaya (2010). When a fluid accelerates, the kinetic energy of the fluid changes correspondingly. The energy supplied to invoke this change is experienced as an additional drag force. This force has the same form as that required to accelerate the mass, and is hence known as added mass. In the case of a sudden acceleration inflicted on a body, the effect is largest at the onset of acceleration, and decreases shortly thereafter. In an experiment with acceleration at all times, larger dampening effects were expected of added mass. As evident from Eq. (1.14), the most important factor influencing added mass is the clearance between casing and drillstring. The bottom element in the drillstring had an outer diameter equal to 38 mm, while the casing inner diameter was equal to 68.9 mm. It is believed that larger diameter drillpipes used for experiments could provide more insights into the effect of added mass in the future.

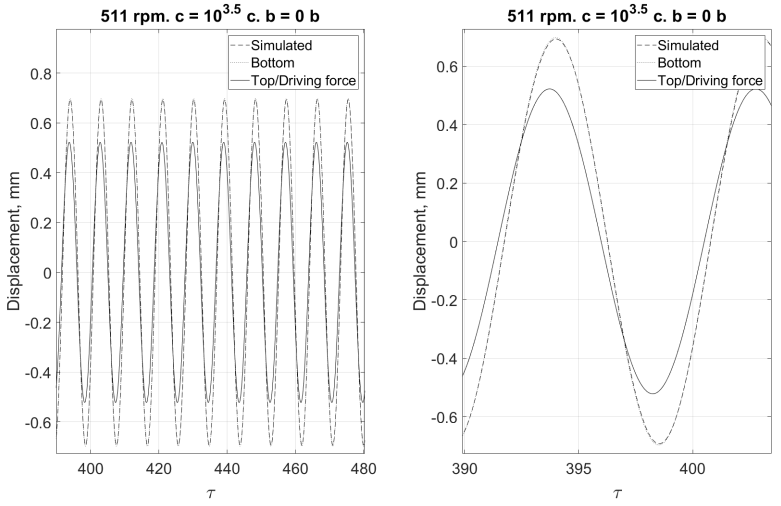

Figure 5.5: Results of 511 rpm experiment with best match of added mass and Basset force coefficients

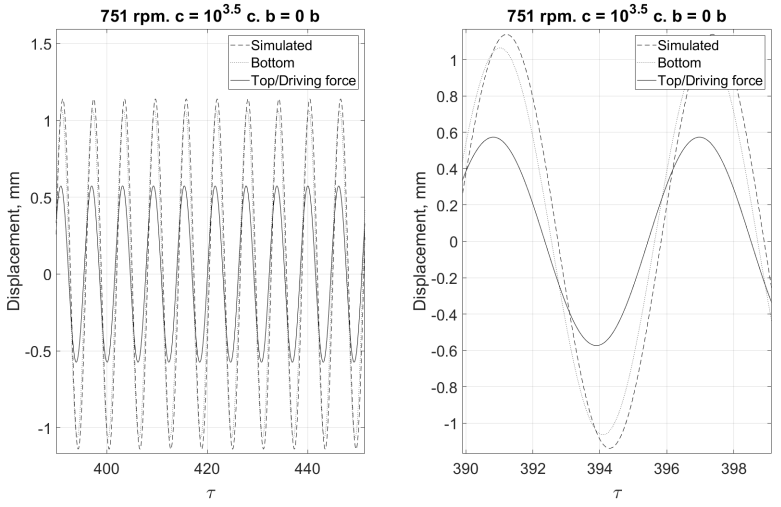

Figure 5.6: Results of 751 rpm experiment with best match of added mass and Basset force coefficients

Chapter 6

Conclusion

This thesis should be considered an initial experimental test of the model presented. Nearly 200 experiments were conducted in both air and water, with frequencies ranging from 105 to 765 rpm. These showed that for frequencies between approximately 350 and 700 rpm, which is believed to be least influenced by dominant exterior factors, the model was able to predict amplification by only topside movement. Amplification in air at 360 rpm (6 Hz) and 705 rpm (11.75 Hz) was predicted to 1.141 and 1.808, with measurements yielding 1.114 and 1.812. The sum of relative errors within this range was found to be 30%. In water, the amplification was predicted to 1.153 and 1.841 at 360 rpm (6 Hz) and 690 rpm (11.5 Hz) respectively, with measurements showing 1.125 and 1.804. All relative errors in this range are summed to 62%. Based on the presented results, friction showed to be principal factor in lower frequency experiments in particular, influencing both amplification and time delay. It is the authors recommendation that results of experiments in this frequency range are excluded from further use, as effects outside the scope of the model are believed to be dominant. At frequencies above 700 rpm, loud noises were heard from the well. It is believed that these noises were caused by collisions between drillstring and casing wall, resulting in vibrations, thus inhibiting drillstring movement. The occurrence of these vibrations is possibly caused by a resonant frequency in lateral motion. It was decided to seize frequency increase to maintain HSE.

Delay was present between both measured top and bottom movement, and the predicted and measured movement of the bottom of the drillstring. Through simulations the delay was expected to be absent, but measurements showed a delay of more than 10 ms at lower frequencies. Larger delay was seen in experiments in air, than in those with water. This might indicate that the measured delay is caused by friction, and that the reduction with water is caused by lubricating effects. At frequencies above 350 rpm, delay is found to be relatively constant in both fluids, and equal to approximately 4 ms. The exactness of the delay is doubtful. This is due to the small size of the number, and the influence that exterior factors proved to have on measurements in other areas. Friction is likely still present at frequencies above 350 rpm, and could easily be attributed a delay of 4 ms. Sine matched

delay is not believed to be completely accurate, as the signal sought to reconstruct deviates from a harmonic trend, due to aforementioned reasons. Besides initial delay, there is little difference seen in measurements with different well fluid, which is attributed to the low viscosity of both fluids, and unaccounted for effects influencing results to a larger degree.

For a better insight to the effect of well fluid and model for description of fluid forces, a sensitivity analysis was preformed with the results from a water-filled well. Matching simulations to measured data required large increase in fluid force coefficients. Modification of viscous force coefficient required a factor of $10^{3.5}$ increase for the best match of amplification. This coefficient resulted in a better match with regards to delay as well. Increasing Basset factors resulted in additional amplification to the simulated movement, which is not supported by physical measurements. The steepness of decreasing delay with increasing frequency of higher Basset forces is neither seen in measurements. It is also noted that the best overall match was found by simply neglecting Basset forces, and matching data by increasing viscous forces. This suggests that assumptions, such as that of the drillstring being an infinite plate, should be revisited, and perhaps even other models could be attempted to better describe fluid mechanical behaviour.

Chapter 7

Further Work

The most important future work will be that of additional experimental testing. Subsequent experiments should include different drillpipe configurations for understanding of material influence. More specifically, larger diameter pipes are recommended. The main argumentation for using larger diameter pipes is the ability to better estimate the fluid model. With the drillstring length and diameter chosen, the sensitivity analysis showed that the damping forces from fluid were overshadowed by effects unaccounted for in the model. This is due to the magnitude of these forces. In low viscous environments such as that of air and water, the damping expected is relatively low. The inclusion of contact friction introduces forces that far exceed those exerted by the well fluid. A selection of more high-viscous well fluid would most likely require an expanded fluid model to account for compressibility. Another advantage of larger diameter piping is reduction in L/D ratio and increased stiffness. With joints of 6m and diameters less than one inch, the pipes curved by only gravity when held horizontally in air. Even though the L/D ratio of the total drillstring is more similar to that in a drilling operation, the L/D ratio in between connections is much smaller.

Another possibility is improvement in the experimental rig up as an effort to minimize these exterior effects. The most important improvement in this perspective would be the development of a new mechanism for transmitting the driving force into a more unidirectional motion.

The results of this initial experimental test suggests that the fluid model should be revisited. A short introduction of a possible approach for a future fluid model is included as well.

7.1 The Morison Equation Approach

According to Sarpkaya and Isaacson (1981) it is impossible to predict the force on the cylinder due to transient behaviour. One possibility might be to consider either preexisting, or the development of an empirical fluid model suitable for describing the fluid

behaviour of the model. A common approach when designing offshore structures such as oil platforms to withstand ocean wave loads is to use the Morison equation. Morison equation summarizes the fluid forces in two individual components; drag and inertia. This is to resemble the force seen by oscillatory flow caused by oscillating motion. The force, F, acting on the body is found as a function of the body's volume and cross-sectional area

$$F = \rho C_m V \dot{u} + \frac{1}{2}\rho C_d A u|u| \tag{7.1}$$

where $\dot{u}$ is the acceleration of the flow, C_m is the inertia coefficient and C_a is the coefficient of added mass. These forces act along the same line, and is hence added. Forces acting transversely are not included in this equation. According to Sarpkaya (2010), theoretical approximations of added mass effects in systems like this are commonly overestimated. The other alternative remaining is the determination of coefficient through empirical data. For the case of an oscillating cylinder, as the model considers, the cross-sectional area is given as $A = \frac{1}{4}\pi D^2$ Hence, the final equation is found to be

$$F = C_m \rho \frac{\pi}{4} D^2 \dot{u} + C_d \frac{1}{2}\rho D u|u| \tag{7.2}$$

Parts of the same issues are present in the case of Morison equations as well. Due to the transient fluid behaviour caused by the oscillating body, an initial force-balance cannot be expected to explain the fluid forces. This is caused by the lack of any physical law accurately describing turbulence. It is possible to use cycle-averaged vales of the coefficients to overcome this obstacle.

Bibliography

Aarsnes, U. J. F., Gleditsch, M. S., Aamo, O. M., Pavlov, A., et al., 2014. Modeling and avoidance of heave-induced resonances in offshore drilling. SPE Drilling & Completion 29 (04), 454–464.

Abdi, H., 2007. The method of least squares. Encyclopedia of Measurement and Statistics. CA, USA: Thousand Oaks.

Alhussainy, F., Sheikh, M. N., Hadi, M. N., 2017. Behaviour of small diameter steel tubes under axial compression. In: Structures. Vol. 11. Elsevier, pp. 155–163.

Balluff, 2018. Magnetostratic sensor. [Online; accessed April 18, 2018].
URL https://www.balluff.com/en/de/productfinder/#?data=selection%5Bca%5D%3DA0001%26selection%5Bcg%5D%3DG0108%26selection%5Bproduct%5D%3DF01802%26selection%5Bproduct_variant%5D%3DPV136698

Bourgoyne Jr, A. T., et al., 1997. Well control considerations for underbalanced drilling. In: SPE Annual Technical Conference and Exhibition. Society of Petroleum Engineers.

Butterworth, S., 1930. On the theory of filter amplifiers. Wireless Engineer 7 (6), 536–541.

Bybee, K., et al., 2008. Compensation of surge and swab pressures in floating drilling operations. Journal of Petroleum Technology 60 (02), 52–54.

Cengel, Y. A., 2010. Fluid mechanics. Tata McGraw-Hill Education.

De Boor, C., De Boor, C., Mathématicien, E.-U., De Boor, C., De Boor, C., 1978. A practical guide to splines. Vol. 27. Springer-Verlag New York.

Everage, S. D., Zheng, N., Ellis, S. E., et al., 2005. Evaluation of heave-induced dynamic loading on deepwater landing strings. SPE Drilling & Completion 20 (04), 230–237.

Hovda, S., 2017. Semi-analytical models on axial motions of an oil well drillstring in vertical wellbores. Journal of Sound and Vibrations (accepted).

Irgens, F., 2006. Fasthetslære. Tapir akademisk forlag.

Kaiser, J., Reed, W., 1977. Data smoothing using low-pass digital filters. Review of Scientific Instruments 48 (11), 1447–1457.

Kreyszig, E., 2010. Advanced engineering mathematics. John Wiley & Sons.

Kvernland, M., Christensen, M., Borgen, H., Godhavn, J.-M., Aamo, O., Sangesland, S., et al., 2018. Attenuating heave-induced pressure oscillations using automated downhole choking. In: IADC/SPE Drilling Conference and Exhibition. Society of Petroleum Engineers.

Lee, U., 2009. Spectral Analysis of Signals. In Spectral Element Method in Structural Dynamics. John Wiley & Sons., Chichester, UK.

Loewenberg, M., 1993. Stokes resistance, added mass, and basset force for arbitrarily oriented, finite-length cylinders. Physics of Fluids A: Fluid Dynamics 5 (3), 765–767.

Mathew, S. G., Nasr, G. G., et al., 2012. Optimized drilling by improved well control using mpd in narrow pressure window. In: Abu Dhabi International Petroleum Conference and Exhibition. Society of Petroleum Engineers.

Narayanan, C., Lakehal, D., Botto, L., Soldati, A., 2003. Mechanisms of particle deposition in a fully developed turbulent open channel flow. Physics of Fluids 15 (3), 763–775.

Nauduri, A. S. S., Medley, G. H., Schubert, J. J., et al., 2009. Mpd: Beyond narrow pressure windows. In: IADC/SPE Managed Pressure Drilling and Underbalanced Operations Conference & Exhibition. Society of Petroleum Engineers.

Rasmussen, O. S., Sangesland, S., et al., 2007. Evaluation of mpd methods for compensation of surge and swab pressures in floating drilling operations. In: IADC/SPE Managed Pressure Drilling & Underbalanced Operations. Society of Petroleum Engineers.

Sarpkaya, T., Isaacson, M., 1981. Mechanics of wave forces on offshore structures.

Sarpkaya, T. S., 2010. Cambridge University Press.
URL https://app.knovel.com/hotlink/toc/id:kpWFOS0004/wave-forces-offshore/wave-forces-offshore

Schwarzkopf, J. D., Sommerfeld, M., Crowe, C. T., Tsuji, Y., 2011. Multiphase flows with droplets and particles. CRC press.

Tobro, H. L., 2017. Experimental predictions of a semi-analytical drill string model.

Van Hinsberg, M., ten Thije Boonkkamp, J., Clercx, H. J., 2011. An efficient, second order method for the approximation of the basset history force. Journal of Computational Physics 230 (4), 1465–1478.

Wolberg, J., 2006. Data analysis using the method of least squares: extracting the most information from experiments. Springer Science & Business Media.

Zhao, D., Sangesland, S., et al., 2015. Down hole pressure variation due to axial stick slip motion effect on drill string. In: SPE Production and Operations Symposium. Society of Petroleum Engineers.

Appendices

Appendix A

Additional results

A.1 Air-Filled Well Results

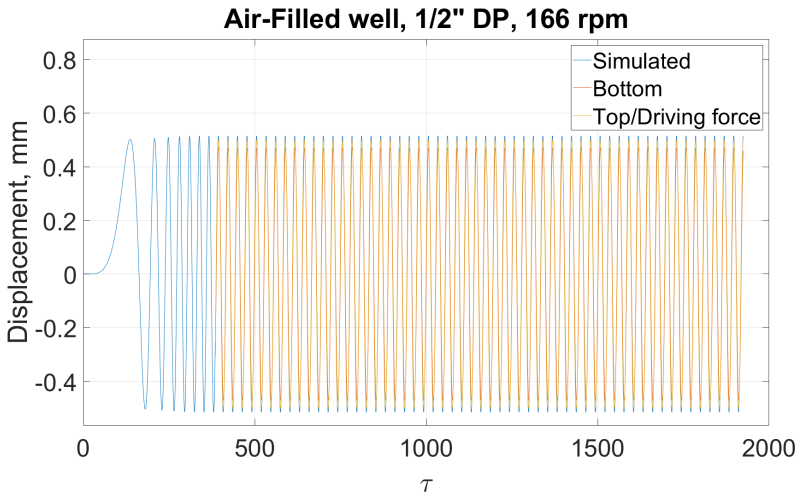

Figure A.1: Full simulation results of 166 rpm experiment in air

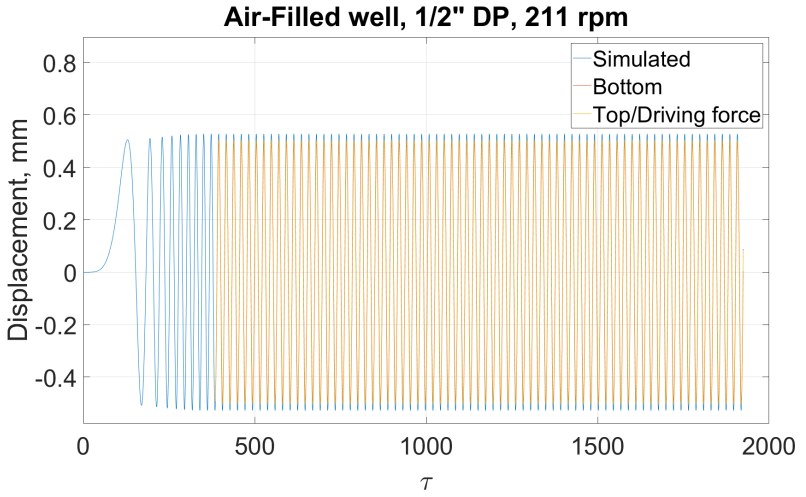

Figure A.2: Full simulation results of 211 rpm experiment in air

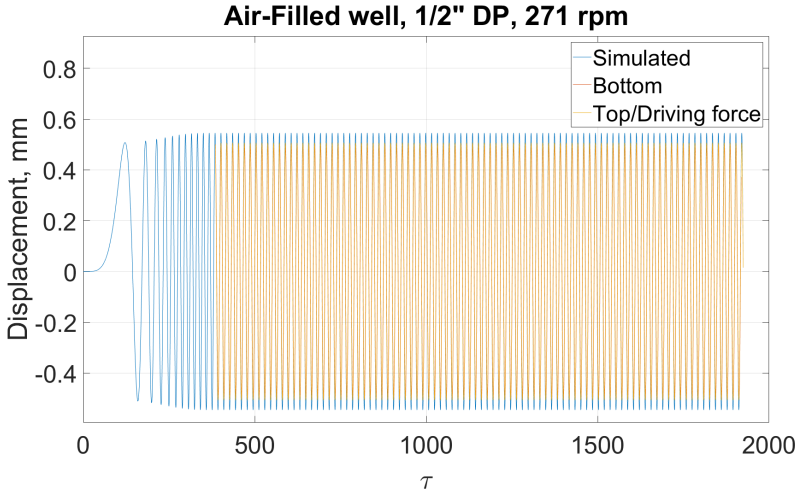

Figure A.3: Full simulation results of 271 rpm experiment in air

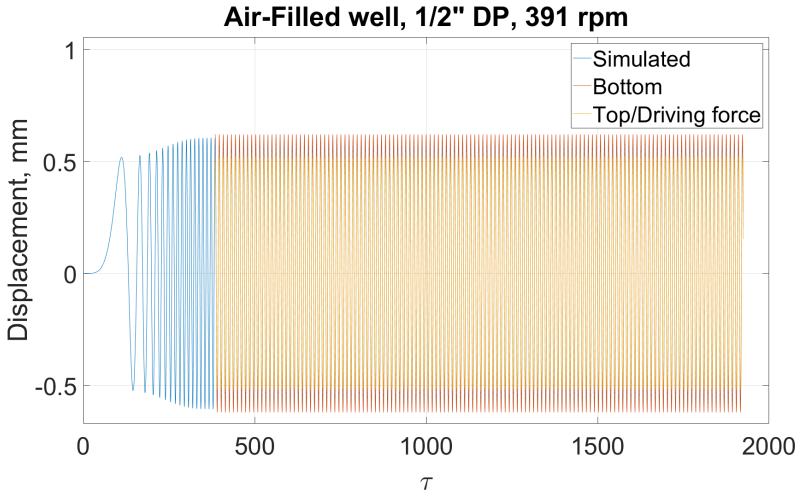

Figure A.4: Full simulation results of 391 rpm experiment in air

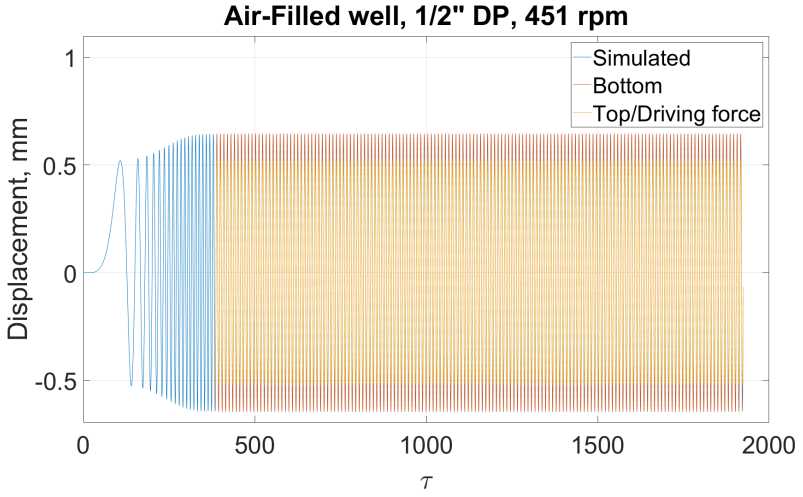

Figure A.5: Full simulation results of 451 rpm experiment in air

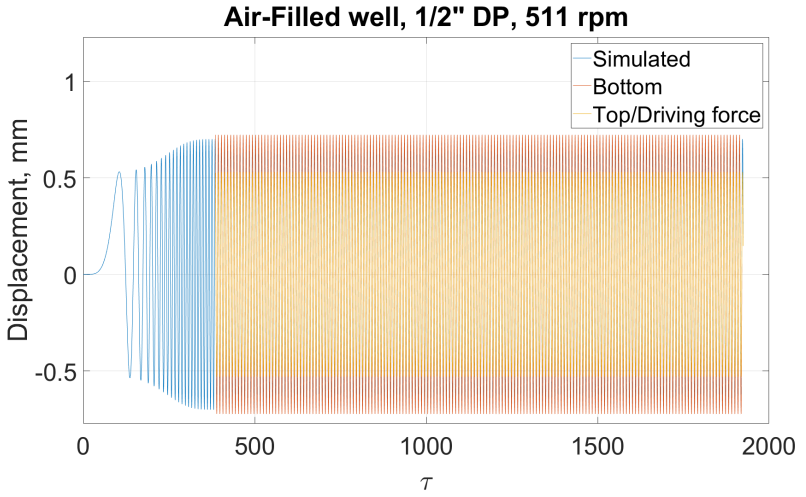

Figure A.6: Full simulation results of 511 rpm experiment in air

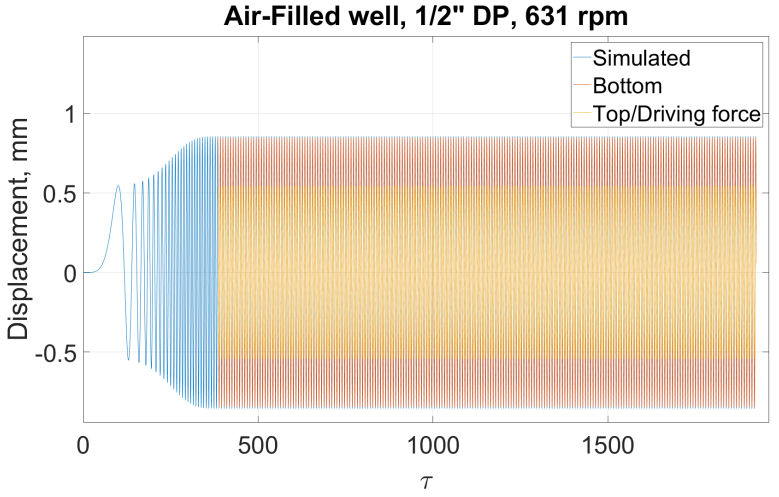

Figure A.7: Full simulation results of 631 rpm experiment in air

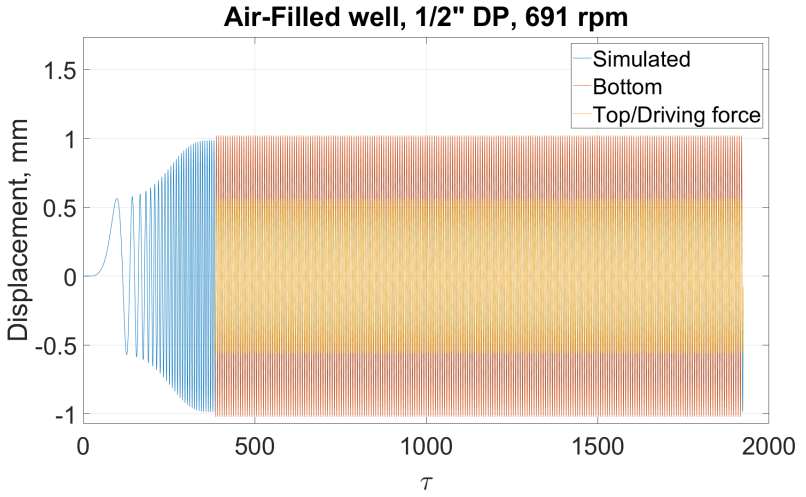

Figure A.8: Full simulation results of 691 rpm experiment in air

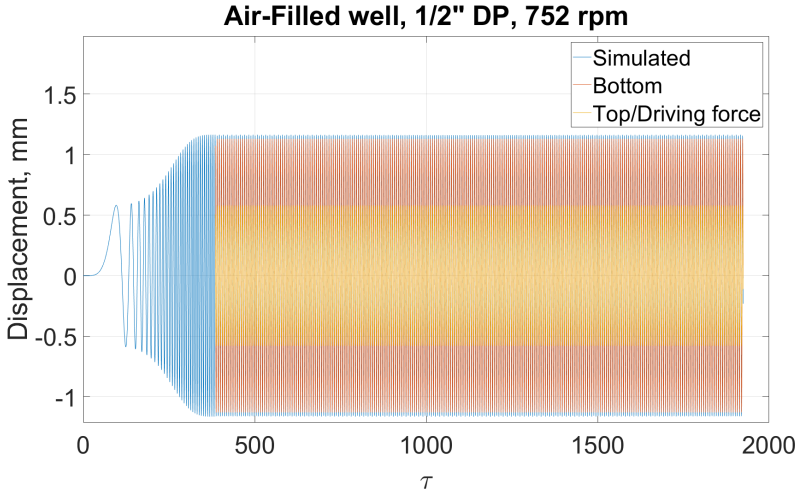

Figure A.9: Full simulation results of 752 rpm experiment in air

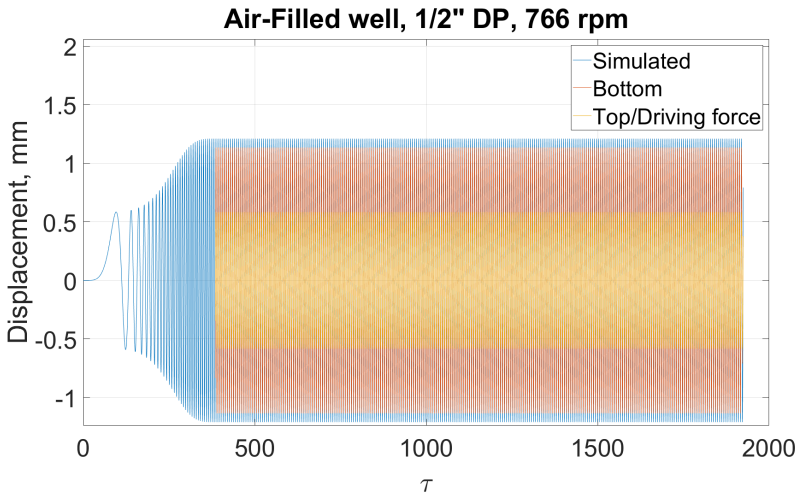

Figure A.10: Full simulation results of 765 rpm experiment in air

A.2 Water-Filled Well Results

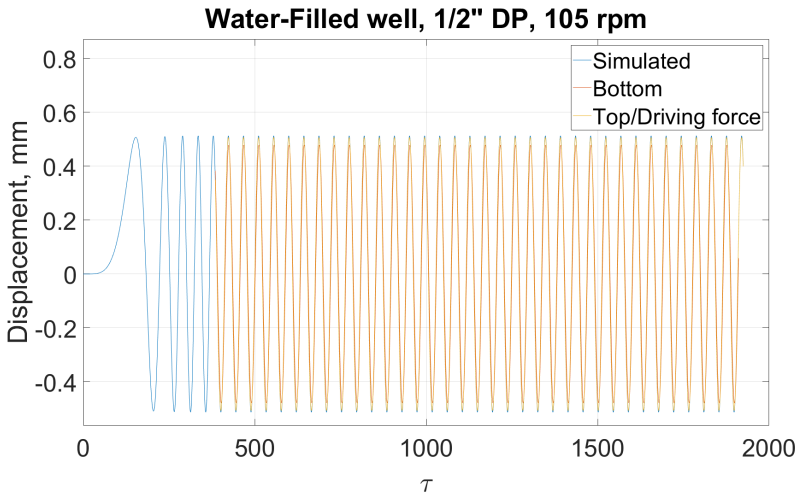

Figure A.11: Full simulation results of 105 rpm experiment in water

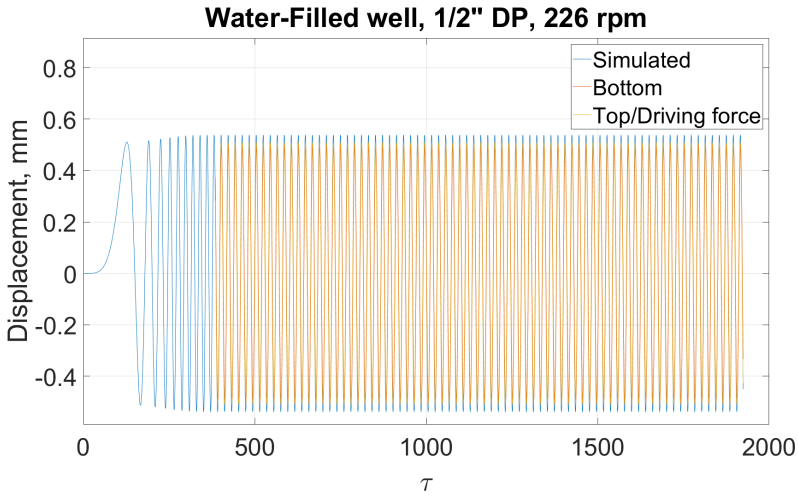

Figure A.12: Full simulation results of 226 rpm experiment in water

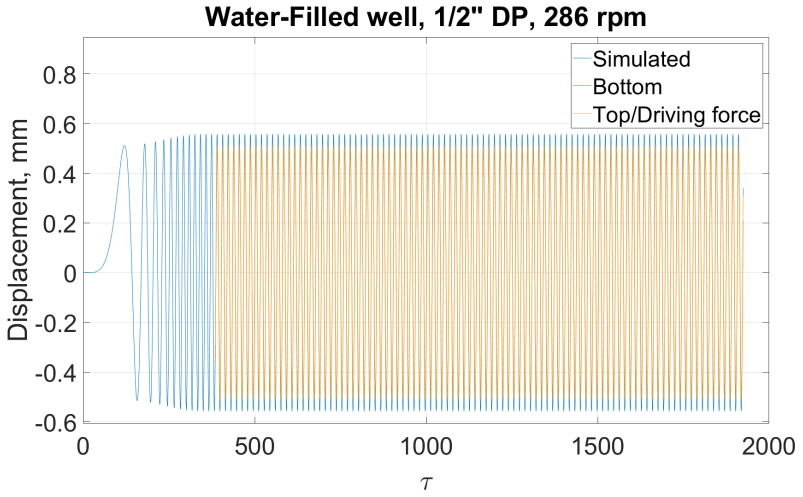

Figure A.13: Full simulation results of 286 rpm experiment in water

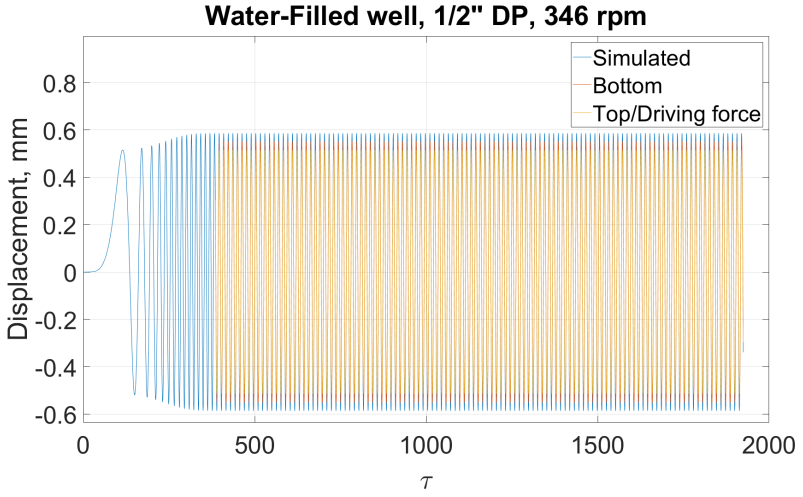

Figure A.14: Full simulation results of 346 rpm experiment in water

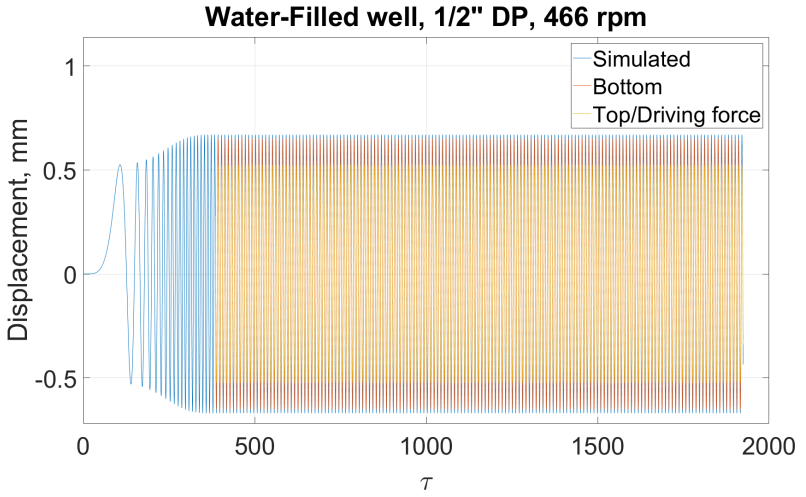

Figure A.15: Full simulation results of 466 rpm experiment in water

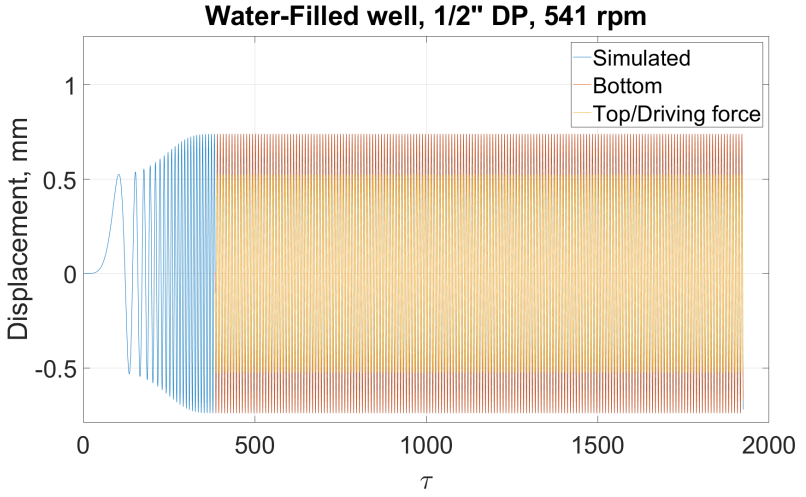

Figure A.16: Full simulation results of 541 rpm experiment in water

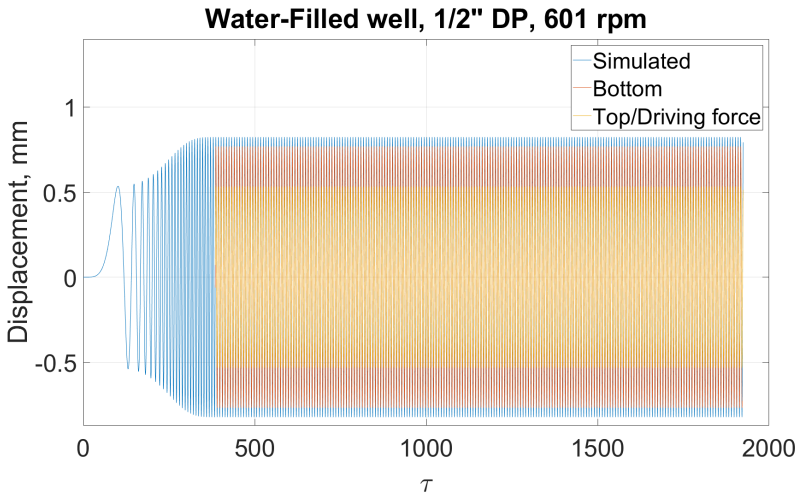

Figure A.17: Full simulation results of 601 rpm experiment in water

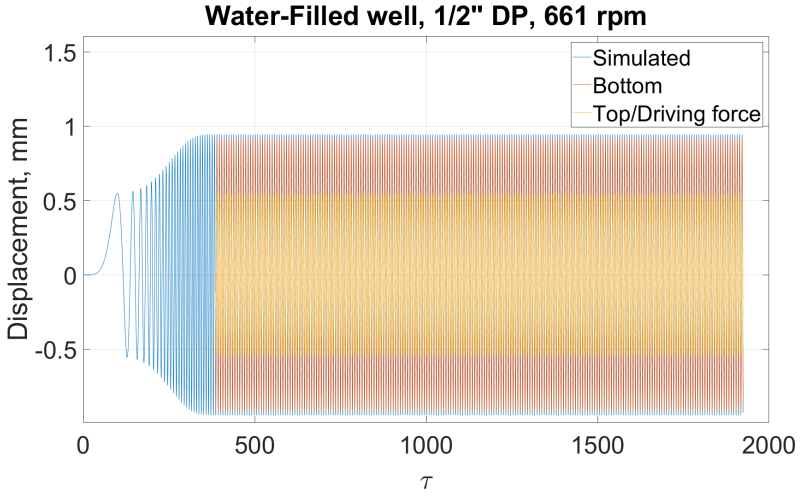

Figure A.18: Full simulation results of 661 rpm experiment in water

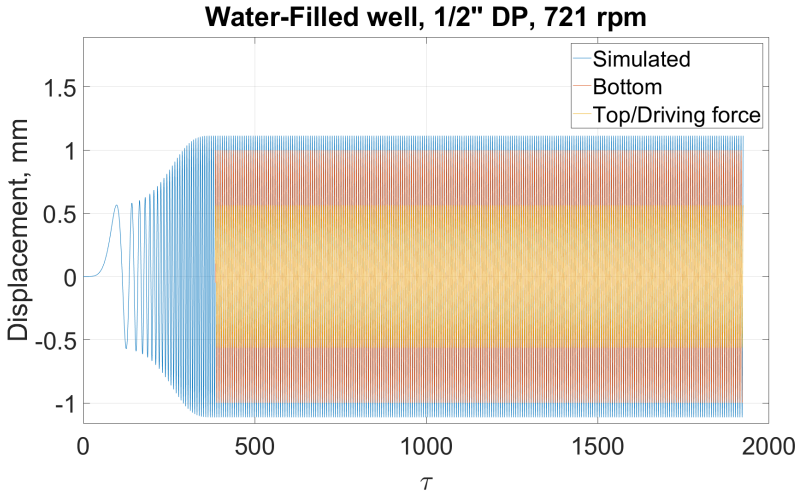

Figure A.19: Full simulation results of 721 rpm experiment in water

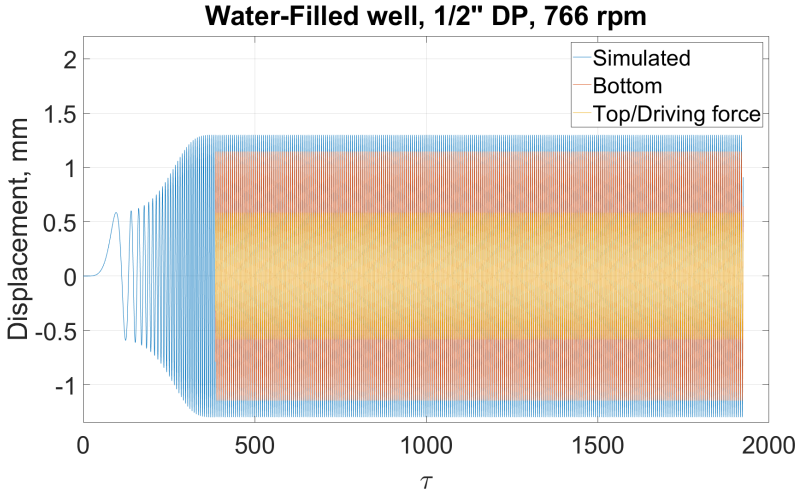

Figure A.20: Full simulation results of 766 rpm experiment in water

Appendix B

Matlab Scripts and Functions

B.1 Main Script

```
clc
clear all
close all
tic
%% Filename to consider
Nmbr = 2; %Experiment Number in .csv file
if Nmbr == 1
    exp_type = 'Air-Filled';
elseif Nmbr == 2
    exp_type = 'Water-Filled';
end
%Filename inputs
day = '03-'; month = '06-'; year = '18';
run = ', Run Number ';
filenumbers = 45;

results = zeros(filenumbers,14);

%for iteration = 1:filenumbers
iteration = 44;
number = num2str(iteration);
filename = ['Experiments/' exp_type '/' day month year '/
    Experiments Halvor ' day month year run number '.txt'];

%% Declaring variables

E = 210E9; %Young's modulus steel
```

```
27 par = experimentInfo(Nmbr); %Struct containing section
       information
28 dimensionless = sqrt(E/par.rho_s)/par.stringLength; %
       Dimensionless conversion factor
29 tbuild = 5; %Duration of build up to frequency
30 tend = 25; %Length of experiments in seconds
31 tauend = tend*dimensionless; %Length of experiments
       dimensionless time
32 taubuild = tbuild*dimensionless; %Dimensionless
33 steps = 250001; %Timesteps
34 tau = linspace(0,tauend,steps); %Dimensionless time vector
35 n = 170; %Number of modelled blocks
36 Fs = 250;
37
38 %% Load measurements
39 [posT, posB, time, freq] = measurements(filename); %Load
       measurements
40
41 %% Signal processing
42 %Filter settings
43 if freq < 400
44     filterset = 1.1;
45 else
46     filterset = 1.4;
47 end
48 [posBot, posTop] = highpassFilter(posB, posT, freq/(
       filterset*60));
49 %[posBot, posTop] = lowpassFilter(posBot, posTop, 2);
50
51 %Removing first movements flattened by filter
52 m_zx = time(posTop.*circshift(posTop,[0 1]) <= 0); %
       measured zero-crossings
53 t_zx = 1/(2*freq/60); %expected time between zero-crossings
54 dev = 50/(Fs*freq); %accepted deviation from estimated time
       between zero-crossings
55 for i = 2:length(m_zx)-1
56     if ((m_zx(i+1)-m_zx(i) > t_zx-dev) && (m_zx(i+1)-m_zx(i
           ) < t_zx+dev))
57         startTime = m_zx(i);
58         break
59     end
60 end
61 for i = 1:length(time)
62     if (time(i) == startTime)
63         startIndex = i+1;
```

```
64          break
65      end
66  end
67
68  %Removing points flattened by filter
69  posTop=posTop(startIndex:end); posBot=posBot(startIndex:end
        ); time=time(startIndex:end);
70  posB=posB(startIndex:end); posT=posT(startIndex:end);
71
72  [ampChange] = filterAmplification(time,posB,posBot); %Find
        amplification caused by amplitude
73
74  %% Sine matching
75  time_dim = (time.*dimensionless); %dimensionless time
76  posTop = posTop - (max(posTop)+min(posTop))/2; %Offsetting
        (more accurate)
77  posBot = posBot - (max(posBot)+min(posBot))/2; %Offsetting
        (more accurate)
78  [posTopSine, sine_fit_top, s_top, topLeast] = SineMatch(
        posTop, time_dim, tau); %Match to a sine function
79  [posBotSine, sine_fit_bot, s_bot, botLeast] = SineMatch(
        posBot, time_dim, tau); %Match to a sine function
80  phase = s_top(3); s_bot(2) = s_top(2);
81
82  %% Calculate simulations
83  freq_dim = freq/60*2*pi/dimensionless; %dimensionless
        angular frequency
84  [Int,omega_t] = freqfunc(3,tau,taubuild,freq_dim); %
        Smoothstep build-up frequency
85
86  index = ceil(((steps-1)*tbuild/tend)+1); %End of build-up
87
88  s_sim = s_top; s_sim(4) = 0;
89  amplitude = s_sim(1); %Utilizing top function as driving
        force
90  method = 'basset';
91  f = @(x)(amplitude.*sin(x)); %Driving force with amplitude
        1cm
92  g = zeros(1,length(tau));
93  g(1:index) = f(Int);
94
95  %Locating common phase shift to connect build-up to
        sinusoid top fit
96  x = (pi-asin((g(index)-s_sim(4))/s_sim(1)))-2*pi*taubuild/
        s_sim(2);
```

```
97  s_sim(3) = 2*pi/x; s_top(3) = 2*pi/x;
98  g(index+1:end) = sine_fit_top(s_sim,tau(index+1:end));
99
100 % Finding correct arcsin value (two options)
101 if (g(index)-g(index-1) > 0)
102     up = 1;
103 else
104     up = 0;
105 end
106
107 if (g(index+1)-g(index) > 0)
108     if (up ~= 1)
109         x = (asin((g(index)-s_sim(4))/s_sim(1)))-2*pi*
                taubuild/s_sim(2);
110         s_sim(3) = 2*pi/x; s_top(3) = 2*pi/x;
111     end
112 else
113     if (up ~= 0)
114         x = (asin((g(index)-s_sim(4))/s_sim(1)))-2*pi*
                taubuild/s_sim(2);
115         s_sim(3) = 2*pi/x; s_top(3) = 2*pi/x;
116     end
117 end
118
119 %Equal time shift for all curves
120 g(index+1:end) = sine_fit_top(s_sim,tau(index+1:end));
121 posTopSine = sine_fit_top(s_top,tau); posBotSine =
        sine_fit_bot(s_bot,tau);
122 posBotSine = posBotSine-s_bot(4); posTopSine = posTopSine-
        s_top(4);
123 deltaTau = s_top(2)*(1/phase-1/s_top(3));
124 bottomtau = tau + deltaTau - round(deltaTau/s_top(2))*s_top
        (2);
125 time_plot = time_dim + deltaTau - round(deltaTau/s_top(2))*
        s_top(2);
126
127 %Find simulated movement
128 [mov, resonance, tau] = experimentMovement(g,tau,method,n,
        par); %Calculate simulated movement
129 resonance = resonance*dimensionless/(2*pi)*60;
130
131 [delay] = findDelay(bottomtau, time_plot, tau, taubuild,
        posTopSine, posBotSine, posTop, posBot, mov, g); %
        Calculate delay by zero-crossings
132 %measured, sine simulated
```

```
133
134 amplitude(1) = abs(s_bot(1)); amplitude(2) = abs(s_top(1));
        amplitude(3) = max(mov);
135
136 results(iteration,1) = freq; results(iteration,2:4) = abs(
        amplitude(:));
137 results(iteration,5:8) = delay(:); results(iteration,9:12)
        = ampChange;
138 results(iteration,13) = topLeast; results(iteration,14) =
        botLeast;
139
140 %% Plotting
141
142 tauend = tend*dimensionless;
143 [~, bottom_start] = min(abs(bottomtau-taubuild));
144 [~, bottom_end] = min(abs(bottomtau-tauend));
145 [~, tau_start] = min(abs(tau-taubuild));
146 [~, time_startIndex] = min(abs(time_plot-taubuild));
147 [~, time_endIndex] = min(abs(time_plot-tauend));
148 freq = round(freq,0);
149 tittel = [exp_type ' well, 1/2" DP, ' num2str(freq) ' rpm'
        ];
150
151 figure
152 plot(tau,mov); hold on
153 title(tittel)
154 ylabel('Displacement, mm')
155 set(gca,'FontSize',40)
156 xlabel('\tau','FontSize',46)
157 toc
158 plot(bottomtau(bottom_start:bottom_end),posBotSine(
        bottom_start:bottom_end)); hold on
159 plot(tau(tau_start:end),posTopSine(tau_start:end)); grid on
160 ylim([-(max(amplitude)+0.05) max(amplitude)*1.7]);
161 legend('Simulated','Bottom','Top/Driving force','Location',
        'NorthEast');
162 hold off
163 figure
164 subplot(1,2,1)
165 plot(tau,mov,'--k'); hold on
166 plot(bottomtau(bottom_start:bottom_end),posBotSine(
        bottom_start:bottom_end),':k'); hold on
167 plot(tau(tau_start:end),posTopSine(tau_start:end),'-k');
        grid on
168 t_dim = 1/(freq/60)*dimensionless;
```

```
169 xlim([taubuild+5 taubuild+5+t_dim*10]);
170 ylim([-(max(amplitude)+0.03) (max(amplitude))*1.4]);
171 title(tittel)
172 ylabel('Displacement, mm')
173 set(gca,'FontSize',24)
174 xlabel('\tau','FontSize',30)
175 legend('Simulated','Bottom','Top/Driving force','Location',
        'NorthEast');
176
177 subplot(1,2,2)
178 plot(tau,mov,'--k'); hold on
179 plot(bottomtau(bottom_start:bottom_end),posBotSine(
        bottom_start:bottom_end),':k'); hold on
180 plot(tau(tau_start:end),posTopSine(tau_start:end),'-k');
        grid on
181 t_dim = 1/(freq/60)*dimensionless;
182 xlim([taubuild+5 taubuild+5+t_dim*1.5]);
183 ylim([-(max(amplitude)+0.03) (max(amplitude))+0.03]);
184 title(tittel)
185 ylabel('Displacement, mm')
186 set(gca,'FontSize',24)
187 xlabel('\tau','FontSize',30)
188 legend('Simulated','Bottom','Top/Driving force','Location',
        'NorthEast');
189
190 %iteration
191 %end
```

B.2 Read Experiment Information

```
function par = experimentInfo(Nmbr)

data = csvread('experimentsInfo.csv');

[n,m] = size(data);
par = struct();

for i = 1:n
    par(i).section = data(i,1); %Experiment number
    par(i).stringLength = data(i,2); %Drillstring length
    par(i).pipeOD = data(i,3); %Drill pipe OD
    par(i).pipeID = data(i,4); %Drill pipe ID
    par(i).pipeWeight = data(i,5); %Drill pipe weight
    par(i).collarLength = data(i,6); %Collar length
    par(i).collarOD = data(i,7); %Collar OD
    par(i).collarID = data(i,8); %Collar ID
    par(i).collarWeight = data(i,9); %Collar weight
    par(i).casingID = data(i,10); %Casing ID
    par(i).rho_m = data(i,11); %Density fluid
    par(i).viscosity = data(i,12); %Fluid viscosity
    par(i).alphaPipe = par(i).pipeOD/par(i).casingID; %
        Calculate alpha
    par(i).alphaCollar = par(i).collarOD/par(i).casingID; %
        Alpha collar
    par(i).pipeArea = pi/4*(par(i).pipeOD^2-par(i).pipeID
        ^2); %Cross-section area
    par(i).collarArea = pi/4*(par(i).collarOD^2-par(i).
        collarID^2);
    par(i).pipeRho_s = par(i).pipeWeight/par(i).pipeArea; %
        Steel density pipe
    par(i).collarRho_s = par(i).collarWeight/par(i).
        collarArea; %Steel density collar
    if i == 1
        par(i).startDepth = 0;
    else
        par(i).startDepth = par(i-1).stringLength;
    end
end
rho_s = mean([par(:).pipeRho_s, par(:).collarRho_s]); %
    average steel density
par = par(Nmbr);
par.rho_s = rho_s;
par.endDepth = par.stringLength+0.60;
```

```
37 end
```

B.3 Load Experiment Measurements

```
function [posT, posB, time, freq] = measurements(filename)

%Measurements
fileID=fopen(filename,'r');

%Importing data to a struct
Data = importdata(filename,'\t',5); %delimiter and number
    of header lines
fclose(fileID);

time = Data.data(:,3)';
posB = -Data.data(:,2)';
posT = -Data.data(:,1)';

%% %Removing initial transient behaviour of measurements
for i = 2:length(time)-1 %Checking for equality in time
    stamp
    if (time(i) ~= time(i+1) && time(i+1) ~= time(i+2))
        time = time(i:end);
        posB = posB(i:end);
        posT = posT(i:end);
        break
    end
end

%Remove points from sqitch-on delay
for i = 1:length(time)-2
    if (time(i) == time(i+1))
        for j = i:length(time)
            if time(j) ~= time(i)
                if i>5
                    startIndex = i-5;
                else
                    startIndex = i;
                end
                endIndex = j+5;
                newTime = linspace(time(startIndex),time(
                    endIndex),endIndex-startIndex+1);
                time(startIndex+1:endIndex) = newTime(2:end
                    );
                break
            end

```

```
40          end
41      end
42  end
43
44  %Offset data
45  posT = posT - mean(posT);
46  posB = posB - mean(posB);
47  measured_crossings = time(posT.*circshift(posT,[0 1]) <= 0)
        ;
48  freq = 60/(2*mean(diff(measured_crossings))); %Freq in rpm
49  end
```

B.4 High-pass Filter

```
function [posBot, posTop] = highpassFilter(posB, posT,
    cutoff)
%highPass filter

d = fdesign.highpass('Fst,Fp,Ast,Ap',0.001,cutoff
    ,80,0.01,250);
Hd = design(d,'equiripple');
posBot = filter(Hd,posB);
posTop = filter(Hd,posT);

% d2 = fdesign.highpass('Fst,Fp,Ast,Ap
    ',0.001,0.7,80,0.01,250);
% Hd2 = design(d2,'equiripple');
% posBot2 = filter(Hd2,posB);
% posTop2 = filter(Hd2,posT);


% fvtool(Hd)

% %plot(psd(periodogram,output,'Fs',250))

end
```

B.5 Filter Amplification Check

```
function [ampChange] = filterAmplification(time, prePos,
    postPos)
%Calculate change in amplitude of each wavelength

if ((prePos(1)*postPos(1) > 0) && (prePos(end)*postPos(end)
    >0)) %Check if top and bottom have different sign
    %This would cause unequal number of zero crossings
    pre_zx = time(prePos.*circshift(prePos, [0 1]) <= 0);
    post_zx = time(postPos.*circshift(postPos, [0 1]) <= 0)
        ;
else
    for i = 1:length(postPos) %Find first instance where
        both have same sign
        if (postPos(i)*prePos(i)>0)
            startIndex = i;
            break
        else
            continue
        end
    end
    for i = length(postPos):-1:1 %Find last instance where
        both have same sign
        if (postPos(i)*prePos(i)>0)
            endIndex = i;
            break
        else
            continue
        end
    end
    pre_zx = time(prePos(startIndex:endIndex).*circshift(
        prePos(startIndex:endIndex), [0 1]) <= 0);
    post_zx = time(postPos(startIndex:endIndex).*circshift(
        postPos(startIndex:endIndex), [0 1]) <= 0);
end

%Removing if there are multiple crossings each wave
per = mean(diff(pre_zx));
time_between = diff(pre_zx);
indices = find(abs(time_between < per/2));
indices = indices + 1;
pre_zx(indices) = [];
time_between = diff(post_zx);
indices = find(abs(time_between < per/2));
```

```
37 indices = indices + 1;
38 post_zx(indices) = [];
39 m = length(post_zx);
40 n = length(pre_zx);
41
42 %Search through each wave for max and min value, and
       calculate difference
43 k = 1;
44 for i = 1:2:n-2
45     [~, start] = min(abs(time-pre_zx(i)));
46     [~, stop] = min(abs(time-pre_zx(i+2)));
47     tempMax = max(prePos(start:stop));
48     tempMin = min(prePos(start:stop));
49     preAmp(k) = (tempMax-tempMin)/2;
50     k = k + 1;
51 end
52
53 %Search through each wave for max and min value, and
       calculate difference
54 k = 1;
55 for i = 1:2:m-2
56     [~, start] = min(abs(time-post_zx(i)));
57     [~, stop] = min(abs(time-post_zx(i+2)));
58     tempMax = max(postPos(start:stop));
59     tempMin = min(postPos(start:stop));
60     postAmp(k) = (tempMax-tempMin)/2;
61     k = k + 1;
62 end
63
64 %Calculate amplitude pre and post filter
65 %Calculate difference and least square residual
66 n = length(preAmp);
67 m = length(postAmp);
68 ampChange(1) = mean(preAmp);
69 ampChange(2) = mean(postAmp);
70 ampChange(3) = mean(preAmp)-mean(postAmp);
71
72 if (n == m)
73     ampChange(4) = sum((preAmp-postAmp).^2);
74 elseif (n > m)
75     shift = n-m;
76     preAmp = preAmp(1:end-shift);
77     ampChange(4) = sum((preAmp-postAmp).^2);
78 else
79     shift = m-n;
```

```
80      postAmp = postAmp(1:end-shift);
81      ampChange(4) = sum((preAmp-postAmp).^2);
82  end
83
84  end
```

B.6 Sine Matching

```
function [posOut, sine_fit, s, sineLeast] = SineMatch(posIn, time, tau)
%Sine Curve Matching

topUpper = max(posIn);
topLower = min(posIn);
topRange = (topUpper-topLower)/2; %Amplitude
zx = time(posIn .* circshift(posIn,[0 1]) <= 0); % Find time of zero-crossings

%Remove noise
per = mean(diff(zx));
time_between = diff(zx);
indices = find(abs(time_between < per/2));
indices = indices + 1;
zx(indices) = [];
T = abs(2*mean(diff(zx))); % Estimate period by time between zero-crossings
%topMean = mean(posIn); % Estimate offset
topMean = (topUpper+topLower);
sine_fit = @(b,time) b(1).*(sin(2*pi.*time./b(2) + 2*pi/b(3))) + b(4); % Sine function
fcn = @(b) sum((sine_fit(b,time) - posIn).^2); % Least-Squares function
%Initial estimate of phase shift
%Due to sensitivity of phase, several are tried
phase = -1;
s = fminsearch(fcn,[topRange, T, phase, topMean]);
%Loop through phase shifts due to sensitivity of phase estimate
for i = 2:11
    tempS = fminsearch(fcn,[topRange, T, (i-1)/5-1, topMean]);
    if fcn(tempS) < fcn(s)
        if tempS(2) > 0
        s = tempS;
        end
    end
end

posOut = sine_fit(s,tau);
sineLeast = fcn(s); %Least square residual
```

B.7 Movement Function

```
function [mov, omega_i1, time] = experimentMovement(f,tau,
    method, n, par)
%f is the driving force function
%tau is the dimensionless timescale
%method is to consider Basset forces or not
%n is number of blocks
%par is struct containing section information
%Int is the entry of the driving force

%Choosing block to look at
block = n;

steps = length(tau);
dtau = (tau(end)-tau(1))/steps;
tau = tau + dtau; %To avoid division with zero
%Number of modelled blocks
depth = par.endDepth;
par.nBlocks = n;
z = depth/n;
par.pipeLength = par.stringLength - par.collarLength;

%This function returns eigenvalues and eigenvectors
mat = createMatrixExp(par);

D = mat.D; %Eigenvalues
V = mat.V; %Eigenvectors

omega_i = n.*sqrt(diag(D));
alpha_1 = par.alphaPipe; %Alpha first pipe

%General constants
E = 210e9;
speed_sound = sqrt(E/par.rho_s);

%Approximations for b and c
c1 = 2*pi*z*par.viscosity*((1+alpha_1^2)/...
    (1-alpha_1^2)*log(alpha_1^(-1))-1)^(-1);
cd = c1/mat.a1;
c = cd*n*speed_sound/(E*mat.a_hat);
zeta_i = c./(2.*omega_i);
omega_di = omega_i.*sqrt(1-zeta_i.^2);
b = par.casingID*sqrt(depth*speed_sound^(3)*pi*par.rho_m*
    par.viscosity)...
```

```
42      /(E*mat.a1*mat.a_hat)*(alpha_1/(1-alpha_1^2));
43
44  kappa_ij = zeros(n,n);
45
46  for ii = 1:n
47      kappa_ij(ii,:) = n^2*mat.a1.*V(:,ii).*V(1,ii)./omega_i(
            ii).^2;
48  end
49
50  Nterms = 100; %Number of terms used for complimentary error
        function
51  switch method
52      case 'basset'
53          y = zeros(1,length(tau));
54          for j = 1:n
55              %Partial fraction decomposition
56          [R,P,K] = residue(kappa_ij(j,block)*omega_i(j)
                ^2,[1,-b*sqrt(pi), c, 0, omega_i(j)^2]);
57          y = y + ...
58              R(1)*(1./sqrt(pi.*tau) + P(1).*cef(1i*P(1).*
                    sqrt(tau),Nterms)) + ...
59              R(2)*(1./sqrt(pi.*tau) + P(2).*cef(1i*P(2).*
                    sqrt(tau),Nterms)) + ...
60              R(3)*(1./sqrt(pi.*tau) + P(3).*cef(1i*P(3).*
                    sqrt(tau),Nterms)) + ...
61              R(4)*(1./sqrt(pi.*tau) + P(4).*cef(1i*P(4).*
                    sqrt(tau),Nterms));
62
63          end
64          y = real(y);
65      case 'regular'
66          s1 = 0;
67          for ii = 1:n
68              s1 = s1 + kappa_ij(ii,block)*omega_i(ii)/sqrt
                    (1-zeta_i(ii)^2)*sin(omega_di(ii).*tau);
69          end
70         y = s1.*exp(-c/2.*tau); %Damping term
71  end
72  omega_i1 = omega_i(1);
73
74
75  Q = f;
76  zeropad = length(y) + length(Q) - 1;  %Zero-padding
77
```

```
78  mov = dtau*ifft(fft(y,zeropad) .* fft(Q,zeropad)); %Solving
        convolution
79
80  mov = mov(1:length(tau));
81  tau = tau - dtau;
82
83  %% Finding constant frequency part of plot
84  %Finding start of constant frequncy period
85  % tbuild = 5;
86  % tend = 20;
87  % for i = steps*tbuild/tend:steps-1 %Start searching after
        build up is finished
88  %     if ((mov(i) < 0.02 && mov(i) > -0.02) && mov(i) < mov
        (i+1))
89  %         startindex = i;
90  %         break
91  %     end
92  % end
93  %
94  % %Find natural endpoint of plotted data
95  % for i = steps-1:-1:steps*tbuild/tend
96  %     if ((mov(i) < 0.02 && mov(i) > -0.02) && mov(i) < mov
        (i+1))
97  %         endindex = i;
98  %         break
99  %     end
100 % end
101 %
102 % %Considering only cosntant-frequency period
103 % mov = mov(startindex:endindex);
104 % time = tau(startindex:endindex);
105 time = tau;
106
107 end
```

B.8 Solve Generalized Eigenvalue Problem

```
function mat = createMatrixExp(par)
%Length of section
depth = par.endDepth;
%Number of blocks
n = par.nBlocks;
%Length of each modelled block
h = depth/n;
%Finding smallest remainder to determine start of collar
collarstart1 = floor(par.pipeLength/h);
collarstart2 = ceil(par.pipeLength/h);
rem1 = abs(par.pipeLength - collarstart1*h);
rem2 = abs(collarstart2*h - par.pipeLength);

if rem1 < rem2 %Deciding to round up or down
    collarStart = collarstart1;
else
    collarStart = collarstart2;
end

%Preallocating up A1 and A2
A1 = zeros(1,n);
alpha = A1;
A_central = A1;

for i = 1:n
    if i <= collarStart
        A1(i) = par.pipeArea;
        alpha(i) = par.alphaPipe;
    else
        A1(i) = par.collarArea;
        alpha(i) = par.alphaCollar;
    end
end

%Geometric average of A1
a_hat = exp(sum(log(A1))/n);
A1 = A1./a_hat; %Normalising A1
mat.a_hat = a_hat;
mat.a1 = A1(1);

%Creating entries for A2
A_central(1:end-1) = A1(1:end-1)+A1(2:end);
A_central(end) = A1(end);
```

```
44 A2 = diag(-A1(2:end),-1) + diag(A_central,0) + diag(-A1(2:
       end),1);
45
46 %Added mass effect
47 added = par.rho_m*pi*(par.casingID/2)^2*alpha(1)^2/(par.
       rho_s*a_hat)*sum((alpha.^2)./(1 - alpha.^2));
48 A1(n) = A1(n) + added;
49
50
51 A1 = diag(A1);
52
53 %Solving generalized eigenvalues
54 [V,D] = eig(A2,A1);
55
56 mat.V = V;
57 mat.D = D;
58
59 end
```

B.9 Frequency Function

```
function [S,Smooth] = freqfunc(N,tau,taubuild,A)
%N is the order of smoothstep
%Tau is the dimensionless time vector
%c is the dimensionless time to build up the step function
%A is the value to build up to
index = ceil((length(tau)-1)*taubuild/tau(end)+1);
S = zeros(1,index);
Smooth = S;
step = tau(2)-tau(1);
%Creating smoothstep function
for i = 1:index
    if tau(i) <= 0
        Smooth(i) = 0;
    elseif tau(i)/taubuild <= 1
        tempS = 0;
        for j = 1:N+1
            tempS = tempS + nchoosek(N+(j-1),(j-1))*
                nchoosek((2*N+1),(N-(j-1)))*(-tau(i)/
                taubuild)^(j-1);
        end

        Smooth(i) = A*(tau(i)/taubuild)^(N+1)*tempS;

    else
        Smooth(i) = A;
    end
end

%Integrating smoothstep
for i = 2:2:index
    if i > 2
        S(i) = simpson(Smooth(1:i),step);
        S(i-1) = mean([S(i),S(i-2)]);
    else
        S(1) = S(2)/2;
    end
end
S(index) = S(end-1)+(S(end-1)-S(end-2));
end
```

B.10 Simpsons Method

```
function I = simpson(f,dx)
I = 0;
n = length(f);


for i = 2:2:n-1
    I = I + 2*dx/6*(f(i-1)+4*f(i)+f(i+1));
end

end
```

B.11 Complimentary Error Function

```
function w = cef(z,N)
% Computes the function w(z) exp(-zA2)erfc(-iz) using a
    rational series with N terms.
% It is assumed that Im(z)>0 or Im(z) 0.



if imag(z(1,2)) < 0,
z = -z;
M = 2*N;
M2 = 2*M;
k = [-M+1:1:M-1]';
L = sqrt(N/sqrt(2));
theta = k*pi/M;
t = L*tan(theta/2);
f = exp(-t.^2).*(L^2 + t.^2);
f = [0;f];
a = real(fft(fftshift(f)))/M2;
a = flipud(a(2:N+1));
Z = (L+i*z)./(L-i*z);
p = polyval(a,Z);
w = 2*p./(L-i*z).^2+(1/sqrt(pi))./(L-i*z);
w = 2.*exp(-(-z).^2) - w;
else
M = 2*N;
M2 = 2*M;
k = [-M+1:1:M-1]';
L = sqrt(N/sqrt(2));
theta = k*pi/M;
t = L*tan(theta/2);
f = exp(-t.^2).*(L^2 + t.^2);
f = [0;f];
a = real(fft(fftshift(f)))/M2;
a = flipud(a(2:N+1));
Z = (L+i*z)./(L-i*z);
p = polyval(a,Z);
w = 2*p./(L-i*z).^2+(1/sqrt(pi))./(L-i*z);
end
end
```

B.12 Find Delay Between Curves

```
function [delay] = findDelay(tau_bottom, time_plot, tau,
    taubuild, posTopSine, posBotSine, posTop, posBot, mov, g
    )
%% Find time shift of measurements
%% Shift of sines

%Find equal starting point in time
if (tau_bottom(1) < tau(1))
    [~, startIndex] = min(abs(tau(1)-tau_bottom));
    [~, endIndex] = min(abs(tau-tau_bottom(end)));
    posTopSine = posTopSine(1:endIndex); tau_top = tau(1:
        endIndex);
    tau_bottom = tau_bottom(startIndex:end); posBotSine =
        posBotSine(startIndex:end);
else
    [~, startIndex] = min(abs(tau_bottom(1)-tau));
    [~, endIndex] = min(abs(tau(end)-tau_bottom));
    posBotSine = posBotSine(1:endIndex); tau_bottom =
        tau_bottom(1:endIndex);
    tau_top = tau(startIndex:end); posTopSine = posTopSine(
        startIndex:end);
end

%Check if top and bottom have different sign
%This would cause unequal number of zero crossings
if ((posTopSine(1)*posBotSine(1) > 0) && (posTopSine(end)*
    posBotSine(end)>0))
      st_zx = tau_top(posTopSine.*circshift(posTopSine, [0
          1]) <= 0); %Sinusoid top zero crossings
      sb_zx = tau_bottom(posBotSine.*circshift(posBotSine,
          [0 1]) <= 0); %Sinusoid bot zero crossings
 else
      for i = 1:length(posBotSine) %Find first instance
          where both have same sign
          if (posBotSine(i)*posTopSine(i)>0)
              startIndex = i;
              break
          else
              continue
          end
     end
     for i = length(posTopSine):-1:1 %Find last instance
         where both have same sign
```

```
33          if (posBotSine(i)*posTopSine(i)>0)
34              endIndex = i;
35              break
36          else
37              continue
38          end
39      end
40      tau_top = tau_top(startIndex:endIndex); posTopSine =
            posTopSine(startIndex:endIndex);
41      tau_bottom = tau_bottom(startIndex:endIndex);
            posBotSine = posBotSine(startIndex:endIndex);
42      st_zx = tau_top(posTopSine.*circshift(posTopSine, [0
            1]) <= 0); %Sinusoid top zero crossings
43      sb_zx = tau_bottom(posBotSine.*circshift(posBotSine, [0
             1]) <= 0); %Sinusoid bot zero crossings
44  end
45  %% Shift of measurements
46  if ((posTop(1)*posBot(1) > 0) && (posTop(end)*posBot(end) >
        0))
47      mt_zx = time_plot(posTop.*circshift(posTop, [0 1]) <=
            0); %Measured top zero crossings
48      mb_zx = time_plot(posBot.*circshift(posBot, [0 1]) <=
            0); %Measured bot zero crossings
49  else
50      for i = 1:length(posBot)
51          if (posBot(i)*posTop(i)>0)
52              startIndex = i;
53              break
54          else
55              continue
56          end
57      end
58      for i = length(posTop):-1:1
59          if (posBot(i)*posTop(i)>0)
60              endIndex = i;
61              break
62          else
63              continue
64          end
65      end
66      posTop = posTop(startIndex:endIndex); posBot = posBot(
            startIndex:endIndex);
67      time_plot = time_plot(startIndex:endIndex);
68      mt_zx = time_plot(posTop.*circshift(posTop, [0 1]) <=
            0); %Sinusoid top zero crossings
```

```
69      mb_zx = time_plot(posBot.*circshift(posBot, [0 1]) <=
            0); %Sinusoid bot zero crossings
70
71  end
72  %% Measured
73  if (length(mt_zx) ~= length(mb_zx))
74      per = mean(diff(mt_zx));
75      time_between = diff(mt_zx);
76      indices = find(abs(time_between < per/2));
77      indices = indices + 1;
78      mt_zx(indices) = [];
79      time_between = diff(mb_zx);
80      indices = find(abs(time_between < per/2));
81      indices = indices + 1;
82      mb_zx(indices) = [];
83      if (length(mt_zx) ~= length(mb_zx))
84          delay(1) = 100;
85      else
86      delay(1) = mean(mt_zx-mb_zx);
87      end
88  else
89      delay(1) = mean(mt_zx-mb_zx); %Time lag between
            measured top and bottom zero crossings
90  end
91  %% Sine delay
92  if (length(st_zx) ~= length(sb_zx))
93      per = mean(diff(st_zx));
94      time_between = diff(st_zx);
95      indices = find(abs(time_between < per/2));
96      indices = indices + 1;
97      st_zx(indices) = [];
98      time_between = diff(sb_zx);
99      indices = find(abs(time_between < per/2));
100     indices = indices + 1;
101     sb_zx(indices) = [];
102     if (length(st_zx) ~= length(sb_zx))
103         delay(2) = 100;
104     else
105         delay(2) = mode(round(st_zx-sb_zx,7));
106     end
107 else
108     delay(2) = mode(round(st_zx-sb_zx,7)); %Time lag
            between sine matched zero crossings
109 end
110 %% Simulated delay
```

```
111 [~, index] = min(abs(tau-taubuild));
112 tau = tau(index:end); g = g(index:end); mov = mov(index:end
    );
113 df_zx = tau(g.*circshift(g,[0 1]) <= 0);
114 sim_zx = tau(mov.*circshift(mov,[0 1]) <= 0);
115 if (length(df_zx) ~= length(sim_zx))
116     delay(3) = 100;
117 else
118     delay(3) = mode(round(df_zx - sim_zx-(tau(2)-tau(1)),7)
        );
119 end
120 %% Delay between simulated and sine matched bottom
121 [~, index] = min(abs(tau_bottom-taubuild));
122 tau_bottom = tau_bottom(index:end); posBotSine = posBotSine
    (index:end);
123 [~, endIndex] = min(abs(tau_bottom(end)-tau));
124 tau = tau(1:endIndex);
125 mov = mov(1:endIndex);
126 if ((mov(1)*posBotSine(1) > 0) && (mov(end)*posBotSine(end)
    >0)) %Check if top and bottom have different sign
127 %     %This would cause unequal number of zero crossings
128     sb_zx = tau_bottom(posBotSine.*circshift(posBotSine, [0
        1]) <= 0);
129     sim_zx = tau(mov.*circshift(mov,[0 1]) <= 0);
130 else
131     for i = 1:length(posBotSine) %Find first instance
        where both have same sign
132         if (posBotSine(i)*mov(i)>0)
133             startIndex = i;
134             break
135         else
136             continue
137         end
138     end
139     for i = length(posBotSine):-1:1 %Find last instance
        where both have same sign
140         if (posBotSine(i)*mov(i)>0)
141             endIndex = i;
142             break
143         else
144             continue
145         end
146     end
147     tau = tau(startIndex:endIndex); mov = mov(startIndex:
        endIndex);
```

```
148     tau_bottom = tau_bottom(startIndex:endIndex);
            posBotSine = posBotSine(startIndex:endIndex);
149     sb_zx = tau_bottom(posBotSine.*circshift(posBotSine, [0
            1]) <= 0);
150     sim_zx = tau(mov.*circshift(mov,[0 1]) <= 0);
151 end
152
153 delay(4) = mode(round(sim_zx-sb_zx,7))+tau(2)-tau(1);
```

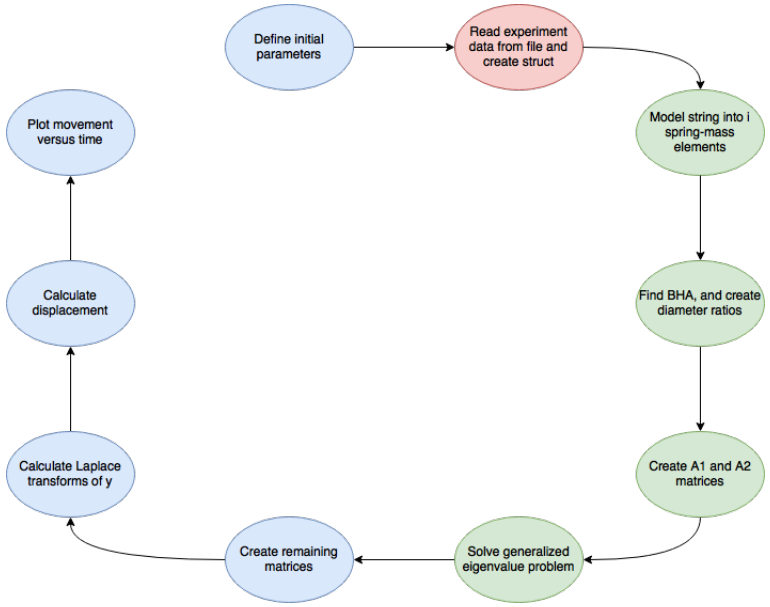

Figure B.1: Flowchart showing procedure of code calculating displacement, different colors for different functions

Appendix C

LabView

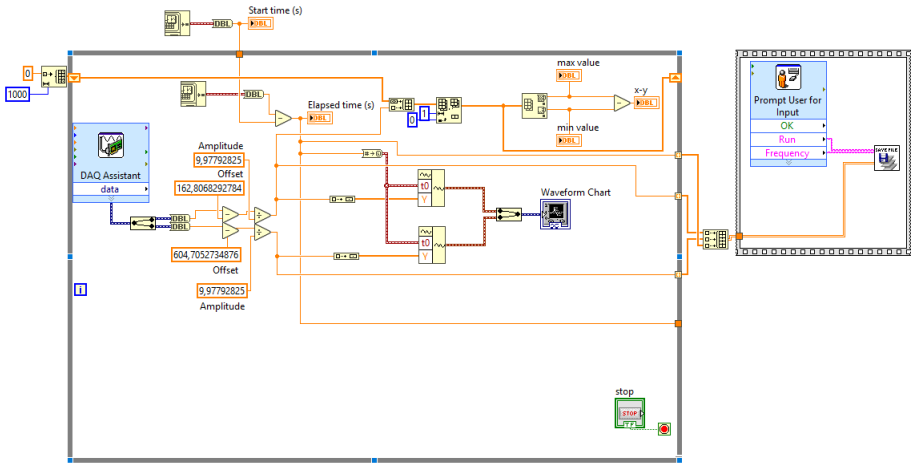

Figure C.1: Main LabView Virtual Instrument

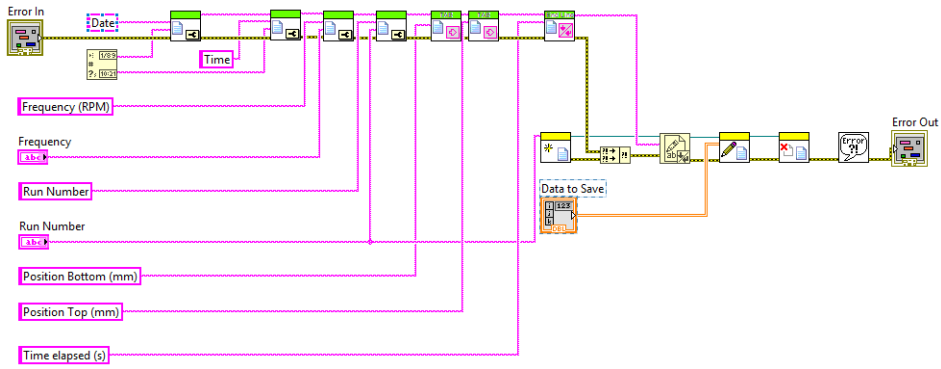

Figure C.2: LabView Save to file VI

Appendix D

Matrices

$$\mathbf{M} = \begin{bmatrix} -m_1 & & & & & & & \\ & -m_2 & & & & & & \\ & & -m_3 & & & & & \\ & & & \ddots & & & & \\ & & & & -m_{n-2} & & & \\ & & & & & -m_{n-1} & & \\ & & & & & & -m_n & \end{bmatrix}. \tag{D.1}$$

$$\mathbf{K} = \begin{bmatrix} k_1+k_2 & -k_2 & & & & & & \\ -k_2 & k_2+k_3 & -k_3 & & & & & \\ & -k_3 & k_3+k_4 & -k_4 & & & & \\ & & \ddots & \ddots & \ddots & & & \\ & & & -k_{n-2} & k_{n-2}+k_{n-1} & -k_{n-1} & & \\ & & & & -k_{n-1} & k_{n-1}+k_n & -k_n & \\ & & & & & -k_n & k_n & \end{bmatrix}. \tag{D.2}$$

$$\mathbf{A}_1 = \begin{bmatrix} a_1 & & & & & & \\ & a_2 & & & & & \\ & & a_3 & & & & \\ & & & \ddots & & & \\ & & & & a_{n-2} & & \\ & & & & & a_{n-1} & \\ & & & & & & a_n + a_{added} \end{bmatrix}. \tag{D.3}$$

$$\mathbf{A}_2 = \begin{bmatrix} a_1+a_2 & -a_2 & & & & & & \\ -a_2 & a_2+a_3 & -a_3 & & & & & \\ & -a_3 & a_3+a_4 & -a_4 & & & & \\ & & \ddots & \ddots & \ddots & & & \\ & & & -a_{n-1} & a_{n-2}+a_{n-1} & -a_{n-1} & & \\ & & & & -a_{n-1} & a_{n-1}+a_n & -a_n & \\ & & & & & -a_{n-1} & a_n & \end{bmatrix}. \tag{D.4}$$

$$\mathbf{B} = \begin{bmatrix} b_1 & & & & & & & \\ & b_1 & & & & & & \\ & & b_1 & & & & & \\ & & & \ddots & & & & \\ & & & & b_1 & & & \\ & & & & & b_1 & & \\ & & & & & & b_1 & \end{bmatrix}. \tag{D.5}$$

$$\mathbf{B} = \begin{bmatrix} c_1 & & & & & & & \\ & c_1 & & & & & & \\ & & c_1 & & & & & \\ & & & \ddots & & & & \\ & & & & c_1 & & & \\ & & & & & c_1 & & \\ & & & & & & c_1 & \end{bmatrix}. \tag{D.6}$$

Appendix E

Rig Up

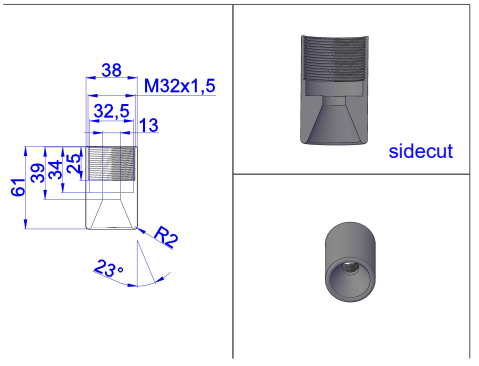

Figure E.1: Funnel for guiding drillpipe to sensor

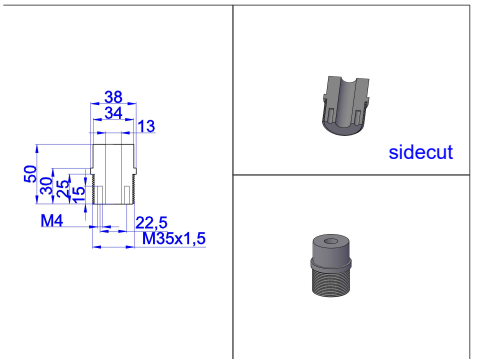

Figure E.2: Crossover from pipe to funnel

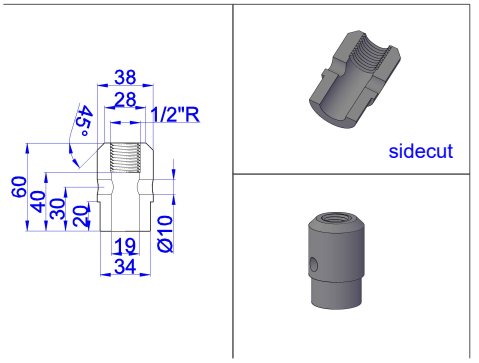

Figure E.3: Crossover for different pipes

SIEMENS

Data sheet for three-phase Squirrel-Cage-Motors

MLFB-Ordering data: **1LE1001-1BB62-2AA4**

Motor type: **1AV2116B**
Client order no.: Item no.:
Order no.: Consignment no.:
Offer no.: Project:
Remarks:

U [V]	Δ / Y	f [Hz]	P [kW]	P [hp]	I [A]	n [1/min]	M [Nm]	NOM. EFF at ... load [%] 4/4	3/4	2/4	Power factor at ... load 4/4	3/4	2/4	I_A/I_N I_r/I_N	M_A/M_N T_r/T_N	M_K/M_N T_B/T_N	IE-CL
230	Δ	50	5.50	- / -	19.50	1460	36.0	87.7	88.2	87.2	0.81	0.73	0.60	7.1	2.5	3.2	IE2
400	Y	50	5.50	- / -	11.20	1460	36.0	87.7	88.2	87.2	0.81	0.73	0.60	7.1	2.5	3.2	IE2
460	Y	60	6.30	- / -	10.80	1760	34.0	89.5	89.8	88.6	0.82	0.75	0.63	7.4	2.5	3.2	IE2
460	Y	60	5.50	- / -	9.60	1765	30.0	89.5	89.3	87.4	0.80	0.72	0.59	8.3	2.8	3.6	IE2
IM B3 / IM 1001		FS 112 M			34 kg	IP55	CC032A	IEC/EN 60034			IEC, DIN, ISO, VDE, EN						

Mechanical data		
Sound pressure level 50Hz/60Hz (load)	58 dB(A)	62 dB(A)
Moment of inertia	0.017 kg m²	
Bearing DE | NDE	6206 2Z C3	6206 2Z C3
Bearing lifetime	40000 h	
Lubricants	Esso Unirex N3	
Regreasing device	No	
Grease nipple	- / -	
Type of bearing	Preloaded bearing DE	
Condensate drainage holes	No	
External earthing terminal		
Vibration class	A	
Insulation	155(F) to 130(B)	
Duty type	S1	
Direction of rotation	bidirectional	
Frame material	aluminum	
Data of anti condensation heating	-/-	
Coating (paint finish)	Standard paint finish C2	
Color, paint shade	RAL7030	
Motor protection	(A) without (Standard)	
Method of cooling	IC411 - self ventilated, surface cooled	

Environmental conditions	
Ambient temperature	-20 °C - +40 °C
Altitude above sea level	1000 m

Terminal box	
Terminal box position	top
Material of terminal box	Aluminium
Type of terminal box	TB1 F00
Contact screw thread	M4
Max. cross-sectional area	4.0 mm²
Cable diameter from ... to ...	11.0 mm - 21.0 mm
Cable entry	2xM32x1,5
Cable gland	2 plugs

Special design (0)

Technical data are subject to change! There may be discrepancies between calculated and rating plate values.

Page 1/1 Version: 2016.10
Generated: 28.11.2017 08:06:50

Figure E.4: Motor specifications (Vedvik and Moen)

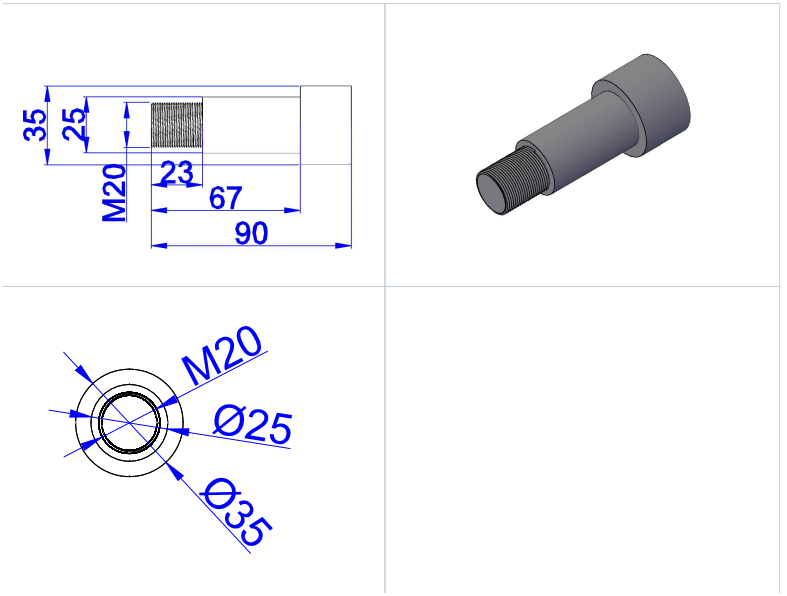

Figure E.5: Motor shaft (Vedvik and Moen)

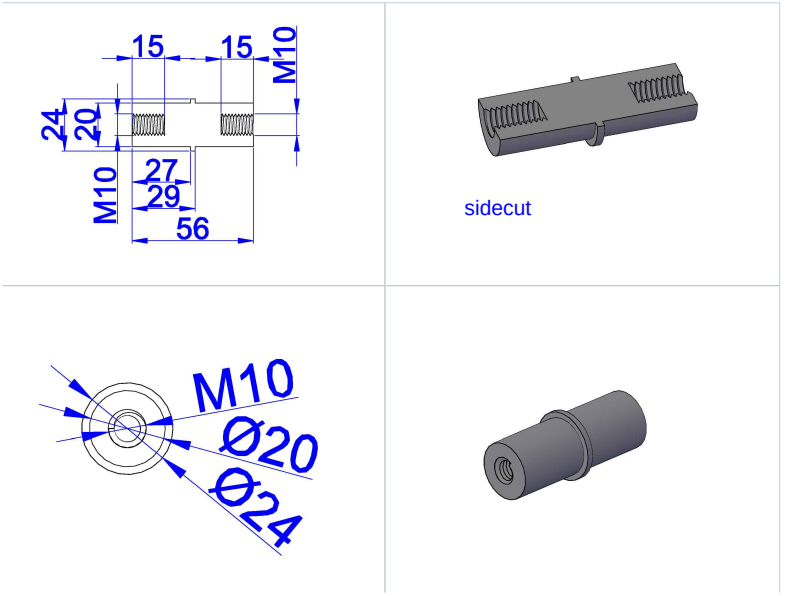

Figure E.6: Shaft (Vedvik and Moen)

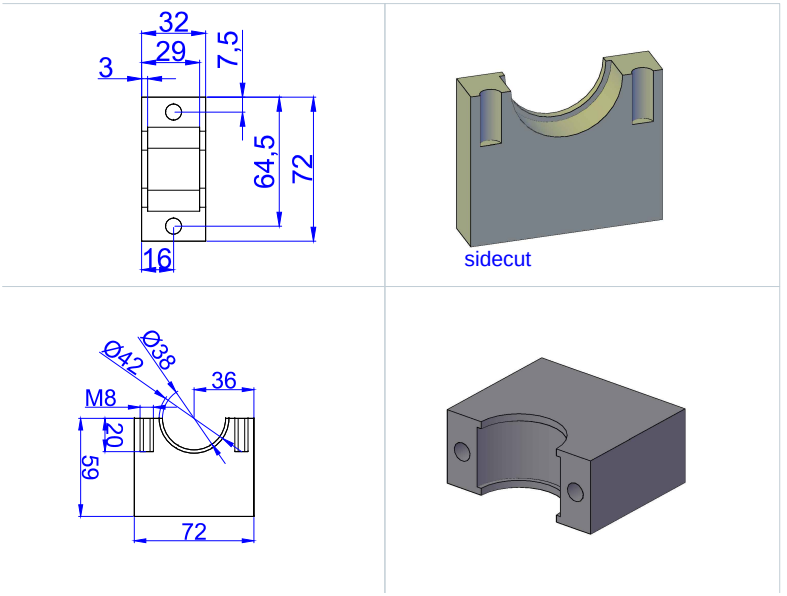

Figure E.7: Bottom mount (Vedvik and Moen)

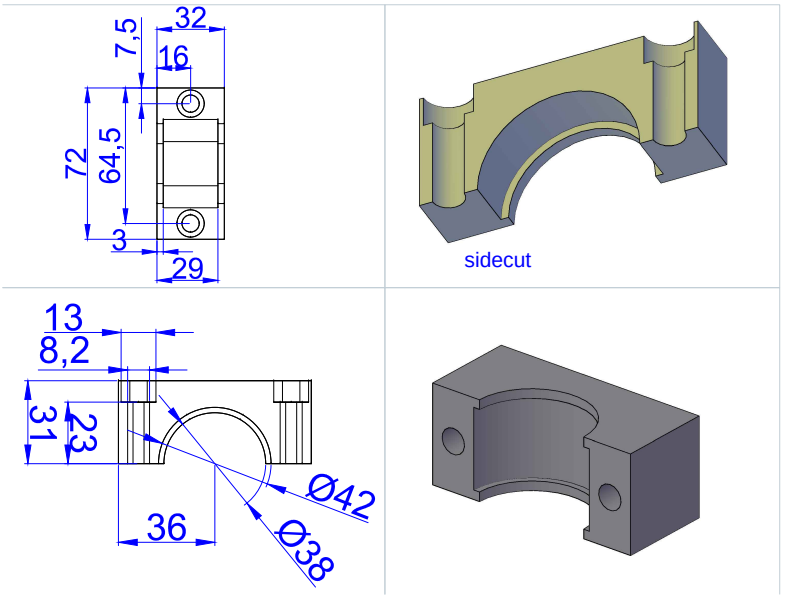

Figure E.8: Top mount (Vedvik and Moen)

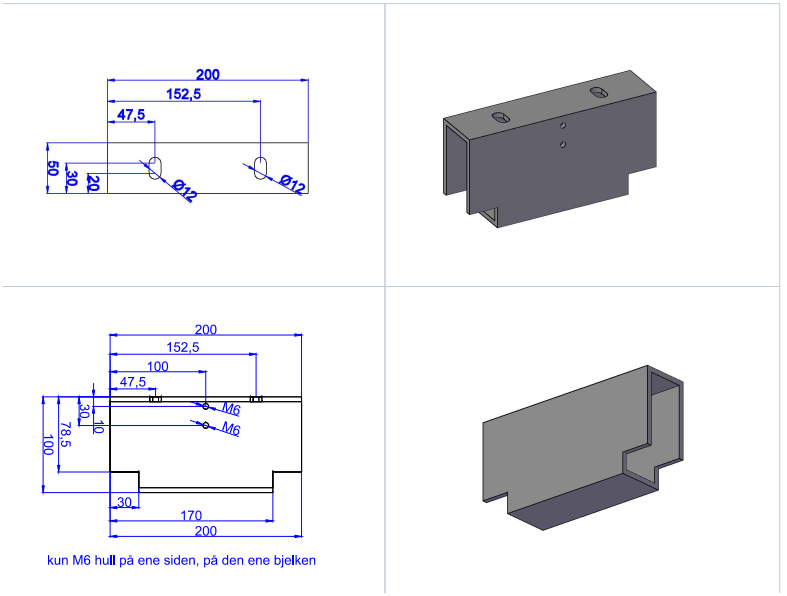

Figure E.9: Bearing mount (Vedvik and Moen)

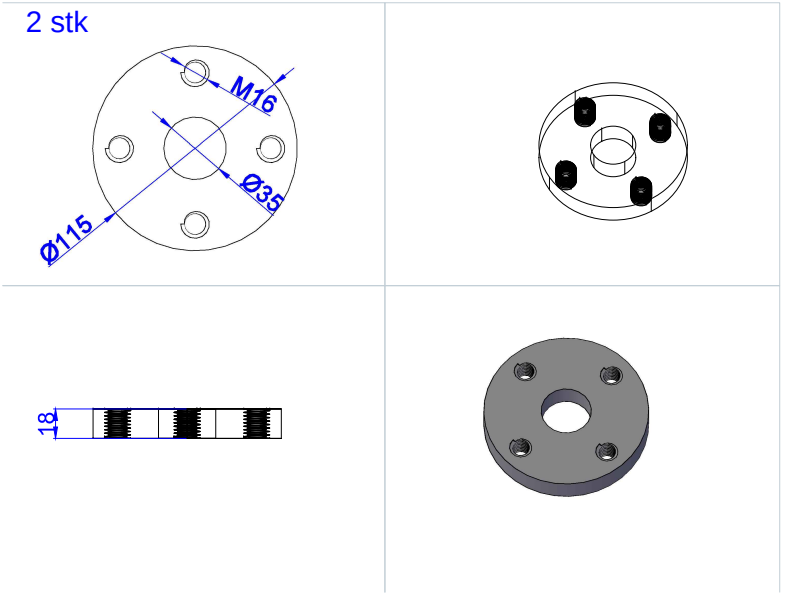

Figure E.10: Offset disc mount (Vedvik and Moen)

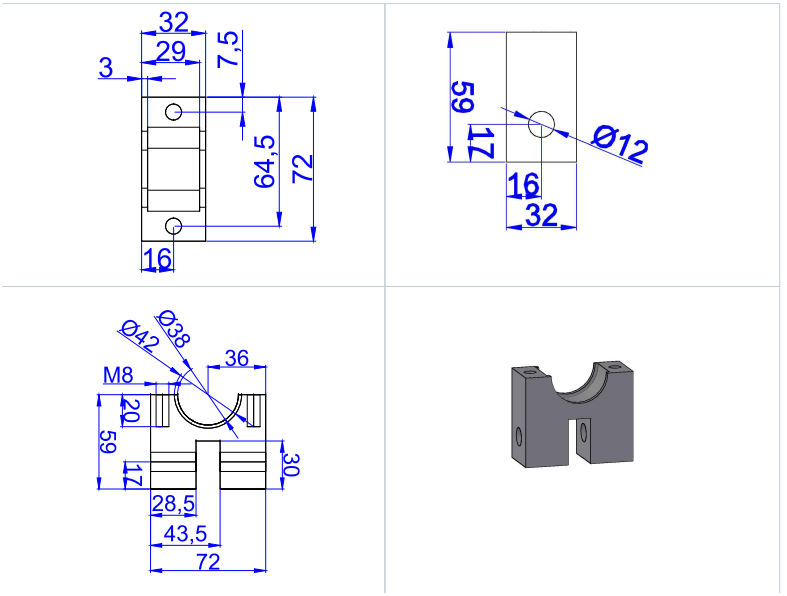

Figure E.11: Offset disc holder (Vedvik and Moen)

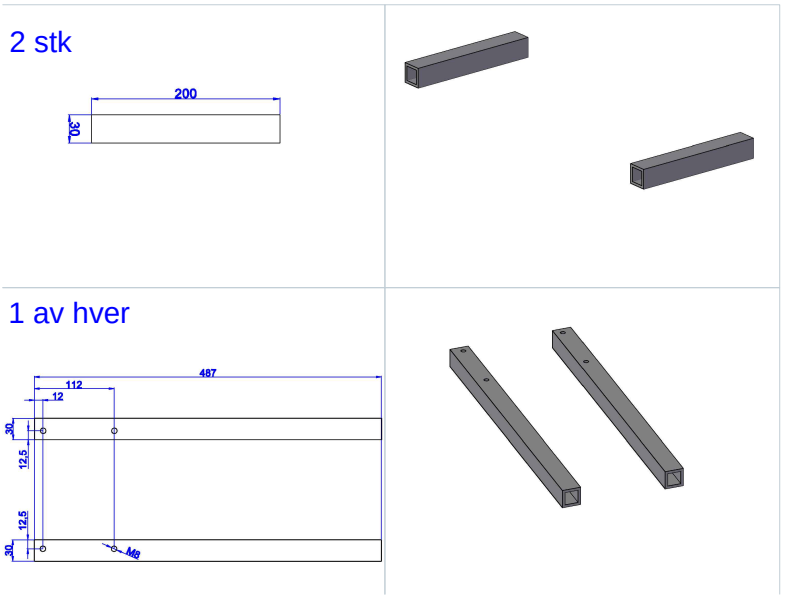

Figure E.12: Frame (Vedvik and Moen)

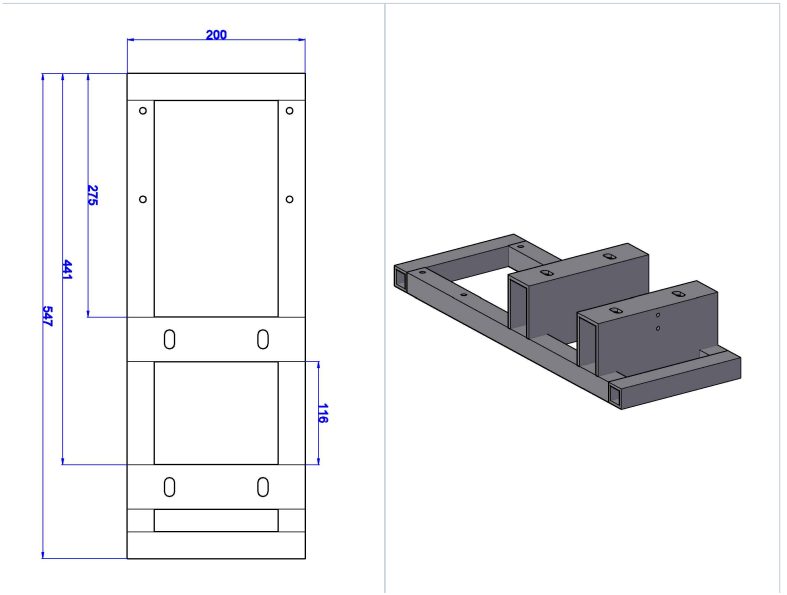

Figure E.13: Full frame (Vedvik and Moen)

Figure E.14: Casing bottom

Figure E.15: Sealing adhesive applied to drillpipe

Figure E.16: Preparing drillpipe for connection

Figure E.17: Drillpipe hoisted for connection

Figure E.18: Bottom drillstring element

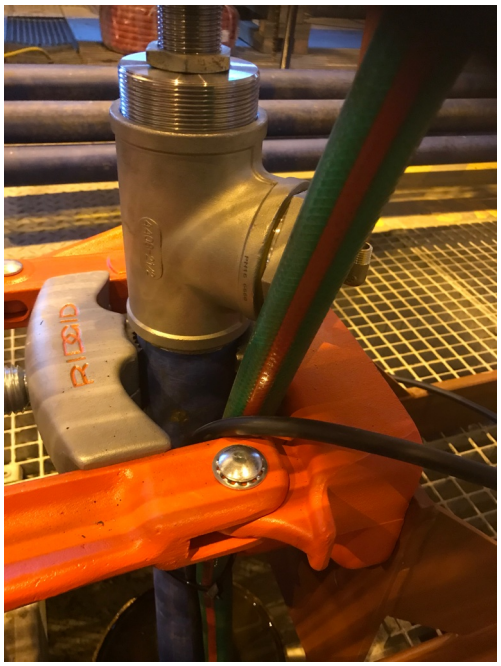

Figure E.19: Cable hose for circulation and T-joint in casing

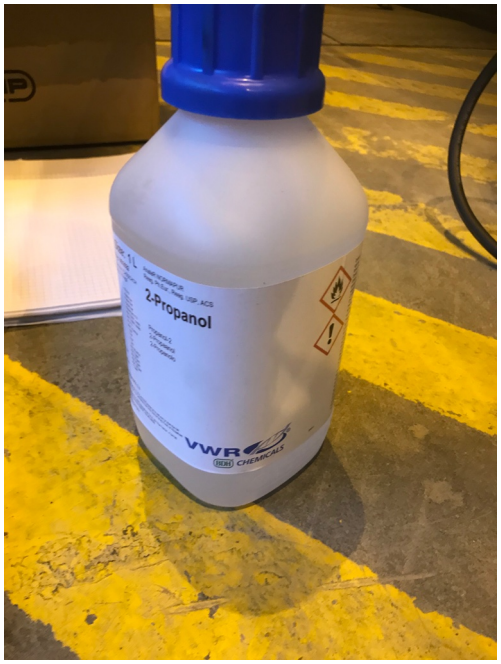

Figure E.20: 2-Propanol for cleaning

Figure E.21: Pressure sensor

Figure E.22: Casing bottom

Figure E.23: Casing

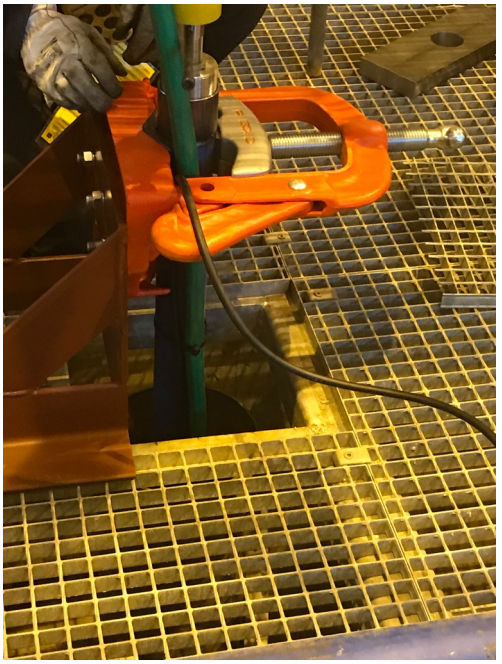

Figure E.24: Running in hole with casing

Figure E.25: Casing

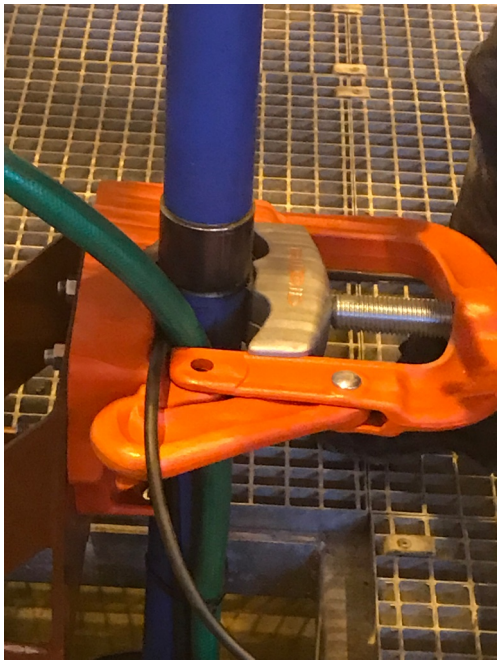

Figure E.26: Slips

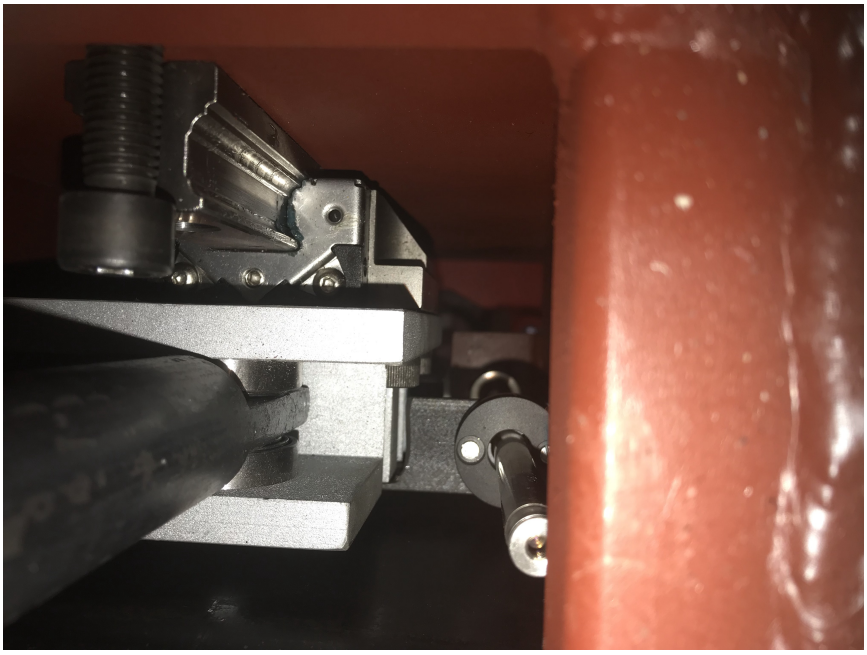

Figure E.27: Connection from motor to pipe and top sensor seen from above

Figure E.28: Connection from motor to pipe and top sensor seen from below

Figure E.29: Slips

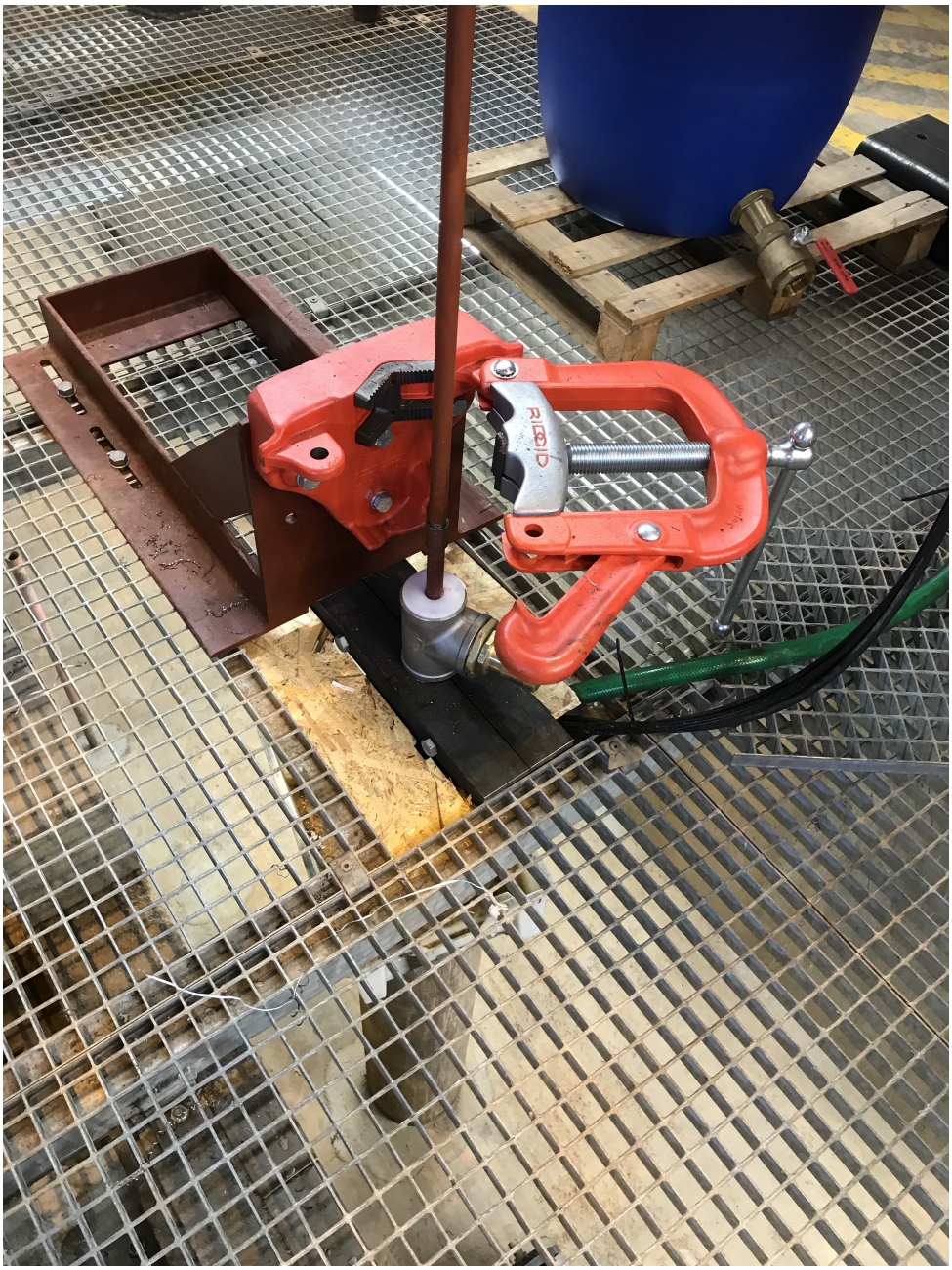

Figure E.30: Topside view of well after completed rig up